Nonlinear Control of the Josephson Plasma in Superconducting Cuprates

Submitted for the Degree of Doctor of Philosophy



Andreas Dienst

Brasenose College, University of Oxford

Trinity 2011

Abstract

Femtosecond optical laser pulses have been comprehensively applied in the past to control the material properties of high critical temperature superconductors. However, since the superconducting gap is of the order of several millielectronvolts, optical photons have the potential to deplete the condensate by breaking Cooper-pairs.

This thesis takes a novel direction as it reports on the non-dissipative control of the Josephson plasma in the layered cuprate superconductor $La_{1.84}Sr_{0.16}CuO_4$ using terahertz electromagnetic waves. To achieve sufficiently intense sub-millimetre radiation, two complementary experimental approaches are taken. First, the table-top tilted pulse front technique is employed as a source of microjoule broadband terahertz pulses. Second, a large-scale free electron laser is operated to achieve multi-cycle pulses of less than two percent relative bandwidth.

Using the tilted pulse front technique, out-of-plane superconducting transport in $La_{1.84}Sr_{0.16}CuO_4$ is gated bi-directionally on ultrafast timescales. The applied electric field modulates the interlayer coupling, leading to picosecond oscillations between superconducting and resistive states. Thereby, the modulation frequency is determined by the electric field strength in spirit of the a. c. Josephson effect. Throughout the oscillations, in-plane properties remain unperturbed, revealing an exotic state in which the dimensionality of the superconductivity is time-dependent.

Using a free electron laser, it is shown that resonant terahertz excitation of nonlinear Josephson plasma waves in $La_{1.84}Sr_{0.16}CuO_4$ creates a metastable state that is transparent over a narrow spectral region. This finding is interpreted as the result of disruptive quantum interference between the linear plasma modes of the cuprate and an optically injected Josephson vortex lattice, which features the periodicity of the driving field, giving rise to three-level quantum interference optical transparency.

Both observations demonstrate the potential of layered superconductors for quantum nonlinear optics and are of relevance for applications in ultrafast nanoelectronics.

Contents

Title Page i

Abstract ii

Table of Contents iii

List of Figures v

Role of the Author vii

Acknowledgement viii

Dedication ix

1 Introduction 1

2 Introduction to Terahertz Science 6

2.1 Optical Probes of Matter 7

2.2 Terahertz Time-Domain Spectroscopy 12

2.3 High-Intensity Terahertz Sources 15

2.4 Time-Resolved Spectroscopy 24

3 Introduction to Superconductivity 27

3.1 Electrostatics of Superconductors 28

3.2 The Ginzburg-Landau Theory 30

3.3 High-Frequency Electrodynamics 33

3.4 The BCS Theory 34
3.5 High-Temperature Superconductivity 37

4 The Josephson Effect 39
4.1 Fundamental Josephson Physics 40
4.2 Electrodynamics of Long Josephson Junctions 45
4.3 Stacks of Josephson Junctions 48

5 The Cuprate $La_{2-x}Sr_xCuO_4$ 52
5.1 *c*-Axis Electrodynamics of $La_{1.84}Sr_{0.16}CuO_4$ 55
5.2 *ab*-Plane Electrodynamics of $La_{1.84}Sr_{0.16}CuO_4$ 58

6 Bi-Directional Electric-Field Gating of Superconductivity 61
6.1 Linear Josephson Plasma Resonance 62
6.2 Experimental Realisation 65
6.3 Ultrafast Electric-Field Gating 67
6.4 Field to Frequency Conversion 69
6.5 Concluding Remarks 73

7 Nonlinear Quantum Plasmonics in a Cuprate Superconductor 74
7.1 Experimental Implementation 75
7.2 Frequency-Selective Nonlinear Plasmonics 78
7.3 Quantum Plasmonics in Cuprates 82
7.4 Transparency Through Quantum Interference 85
7.5 Concluding Paragraphs 88

8 Summary and Outlook 90

Bibliography 93

A Photos and Cover 105

List of Figures

2.1 The electromagnetic spectrum 7

2.2 Refraction of light and terahertz time-domain spectroscopy 13

2.3 Photoconductive terahertz emitter 14

2.4 Tilted pulse front generation in lithium niobate crystals 17

2.5 Time- and frequency-domain high-intensity terahertz pulses 18

2.6 Determination of terahertz pulse energies 19

2.7 Terahertz polarisation and near-infrared spectra 20

2.8 Operational principle of a free electron laser 22

2.9 Characterisation of the free electron laser pulses 23

2.10 Terahertz pump, terahertz probe spectroscopy 25

3.1 Illustration of the Meissner effect 29

3.2 Interface between superconducting and normal domains 32

3.3 The superconducting energy gap 36

4.1 The Josephson effect 40

4.2 Nonlinear modes of long Josephson junctions 46

4.3 Physics of stacks of Josephson junctions 50

5.1 Microscopic properties of the cuprate $La_{2-x}Sr_xCuO_4$ 53

5.2 Out-of-plane equilibrium optical constants of $La_{1.84}Sr_{0.16}CuO_4$ 56

5.3 In-plane equilibrium reflectivity of $La_{1.84}Sr_{0.16}CuO_4$ 59

5.4 Plot of literature values of in-plane equilibrium properties of $La_{1.84}Sr_{0.16}CuO_4$ 60

6.1 Linear optical response of $La_{1.84}Sr_{0.16}CuO_4$ 63
6.2 Characterisation of pump and probe pulses 66
6.3 Experimental realisation of electric-field gating 67
6.4 Time-dependent optical conductivity 68
6.5 Ultrafast electric field gating of superconductivity 70
6.6 Pump-induced modulation of peak probe field 71
6.7 Field dependence of gating frequency 72

7.1 Experimental realisation of light-induced transparency 76
7.2 Linear plasmonics in $La_{1.84}Sr_{0.16}CuO_4$ 77
7.3 Reflectivity change for different excitation wavelengths 79
7.4 Time-dependent loss function 81
7.5 Schematic of a Josephson vortex train in a light field 83
7.6 Dispersion relations and principle of quantum interference optical transparency 84
7.7 Fit of the loss function with the coupled oscillator model 87

A.1 Photograph of the Oxford vacuum chamber exterior 105
A.2 Photograph of the Oxford vacuum chamber interior 106
A.3 Photograph of the Dresden vacuum chamber exterior 107
A.4 Photograph of the Dresden vacuum chamber interior 108
A.5 Cover of the August 2011 issue of *Nature Photonics* 109

Role of the Author

Unless otherwise clearly stated, all data acquisition and analysis presented in this thesis was performed by the author. The terahertz time-domain spectroscopy apparatus as well as the tilted pulse front setup described in chapter 2 were built and characterised by the author in the Oxford laboratory. The $La_{1.84}Sr_{0.16}CuO_4$ samples were grown by S. Pyon, T. Takayama and H. Takagi. The measurement of the linear optical properties of the cuprate discussed in chapter 5 was achieved by the author, who also conducted the data analysis. Bi-directional gating of superconducting transport in $La_{1.84}Sr_{0.16}CuO_4$ was demonstrated by the author in the Oxford laboratory. Assistance with the experimental realisation was given by M. C. Hoffmann, D. Fausti and J. C. Petersen. The author performed the data analysis, while the interpretation was accomplished together with A. Cavalleri. The results were published in *Nature Photonics* (Dienst *et al.*, 2011a). Further documentation can be found in two book contributions (Dienst *et al.*, 2011c; Foerst *et al.*, 2011). The author was involved in related experiments on light control of interlayer coupling in cuprates reported in *Science* (Fausti *et al.*, 2011). The experiments on nonlinear vortex excitation in $La_{1.84}Sr_{0.16}CuO_4$ were designed by the author, while the measurements taken at the free electron laser in Dresden were the result of an international large-scale collaboration under the joint leadership of D. Fausti and the author. The colleagues involved in the implementation of the experiment were M. C. Hoffmann, V. Khanna, M. Gensch, S. Winnerl and W. Seidel. The data analysis was carried out by the author, while the experimental observations were interpreted by A. Cavalleri and the author. A manuscript with the results was submitted for review (Dienst *et al.*, 2011b).

Acknowledgement

In the first place I would like to thank Andrea Cavalleri for supervising me throughout my DPhil and for introducing me to this exciting field of physics. Working together with Andrea has been an inspiring and intense experience, which allowed me to acquire skills applicable far beyond the physical sciences. I am very thankful for his guidance on how to exhibit information in a clear and concise manner, and for giving me the opportunity to present my findings at conferences around the world.

I would also like to express my gratitude to Andrew Boothroyd for providing insight into research at Oxford when I was seeking opportunities as an undergraduate. It has been a great experience to pursue my Doctoral studies here.

Throughout the years, I have very much enjoyed the company of my fellow group members. I would like to thank Matthias C. Hoffmann and Daniele Fausti for teaching me about ultrafast optics and terahertz science. Their, as well as Vikaran Khanna's, companionship at the free electron laser in Dresden is greatly appreciated. Friday night drinks, College dinners, and excessive May Days with Nicky Dean, Jesse C. Petersen, Giovanni Cotugno, and the rest of the group will be sorely missed. I furthermore thank all current and former members of the Simon Room for having made our office an extremely friendly and pleasant working environment.

With great emphasis, I would like to express my gratitude to my girlfriend Yihan for her continuous support and loving personality. I am very lucky to have met you back then in York. Words are not enough to thank my family, and in particular my parents Hiltrud and Willi. Without your advice and support, I would not have made it this far. I will never forget that, thank you.

Für meine Eltern

Chapter 1

Introduction

The electrical conductivity of a specimen describes how fiercely the material properties oppose the flow of an electric current. Charge transport in most conventional metals can be understood by neglecting electron-electron interactions, similar to the treatment of an ideal gas. In strongly correlated electron systems, however, the carriers cannot be described as independent non-interacting entities. Due to the large amount of complex interactions, correlated materials exhibit very rich phase diagrams. Depending on conditions such as temperature, pressure or doping with impurity atoms, the sample properties can change dramatically. Phase transitions describe the changeover between different states of matter (Kittel, 2005).

A prominent example of a phase transition caused by strong electron-electron interactions is observed in superconducting materials (Tinkham, 1996). As a superconductor is cooled below a critical temperature T_c, it changes from being a (bad) conductor to an exotic state characterised by vanishing resistivity and the expulsion of magnetic fields, an observation called the Meissner effect (Kittel, 2005). The technological importance of superconductivity has led to the award of several Nobel Prices for ground-breaking discoveries in the years 1913, 1972, 1973, 1987 and 2003[†]. Many high-technology applications utilise the materials' extraordinary properties to detect

[†] "All Nobel Prizes". Nobelprize.org. 11 July 2011
http://nobelprize.org/nobel_prizes/lists/all/index.html

or generate magnetic fields (Larbalestier *et al.*, 2001). Examples include sensitive magnetometers, magnetic resonance imaging techniques, and high-field applications in maglev trains. The switching properties contemplated in a later part of this thesis allow for the construction of ultrafast digital circuits. The potential for low-loss power cables is obvious, however, applications have been limited due to the requirement of cryogenic cooling.

The phenomenon of vanishing conductivity was observed for the first time in 1911 by H. K. Onnes, but it took almost 50 years until a microscopic description had been derived based on quantum mechanics (Tinkham, 1996). Within this framework, all superconducting electrons form pairs that condense into the same energetic state which can be described by a single many-body wavefunction (Bardeen *et al.*, 1957). Superconductors can be categorised into low- and high-T_c compounds, the latter having transition temperatures in excess of 30 K (Bednorz and Müller, 1986). While the origin of electron pair formation in low-temperature superconductivity is well-understood, a satisfactory description of the physics of high-temperature compounds is still lacking, complicating the objective to further increase the transition temperatures, potentially close to room temperature.

Cuprates are quasi two-dimensional high-T_c materials, in which superconducting carriers are residing in copper oxygen layers that are separated by insulating planes (Lee *et al.*, 2006). Adjacent layers are found to be coupled by the Josephson effect (Josephson, 1962), mediating out-of-plane superconductivity. The interlayer tunnelling amplitude is determined by the sine-Gordon equation for the phase difference of the superconducting order parameter across the planes (Kleiner and Müller, 1994). At equilibrium, the superconducting phase strongly resists perturbations and tends to be uniform throughout the material. As such, a gradient in the order parameter phase is responsible for supercurrents, while the absolute order parameter describes the density of superconducting charge carriers (Tinkham, 1996).

Due to the inductive layer coupling and microscopic geometry of cuprates, a

plasma resonance at terahertz (10^{12} Hz) frequencies develops, corresponding to small-amplitude oscillations of the phase (Kleiner and Müller, 1994). Because external electromagnetic fields couple to these collective charge excitations, terahertz time-domain spectroscopy can be applied to directly observe the linear Josephson resonance in these materials (Tamasaku *et al.*, 1992). In order to explore the nonlinear phase regime in cuprates, interlayer transport can be altered statically by application of magnetic or electric fields (Schafgans *et al.*, 2010). To achieve this effect on the ultrafast timescale, interlayer voltage drops of tens of millivolts are required, corresponding to peak electric fields reaching hundreds of kilovolts per centimetre (Savel'ev *et al.*, 2006).

Using optical pump-probe techniques based on femtosecond lasers, one can gain important information about the out-of-equilibrium physics of superconductivity (Averitt *et al.*, 2001). However, because the superconducting gap is of the order of several millielectronvolts, optical photons have the potential to deplete the condensate by breaking Cooper-pairs. If one wishes to control the superconducting state on these timescales without inducing dissipation, one has to apply photons with energies below the pair-breaking threshold, such as terahertz radiation.

Nonlinear spectroscopy in the terahertz regime has long been impossible due to a lack of sufficiently bright sources. However, recent progress in high-intensity terahertz science has removed this limitation. On the one hand, broadband single-cycle terahertz pulses of picosecond (10^{-12} s) duration can be generated with table-top setups (Hebling *et al.*, 2008a). Pulse energies reach the microjoule regime, providing electric field strengths of hundreds of kilovolts per centimetre. On the other hand, powerful narrowband multi-cycle pulses at less than two percent relative bandwidth have become available at large-scale free electron lasers[†].

The aim of this work is to exploit novel techniques in the field of terahertz science to accomplish nonlinear spectroscopy of $La_{1.94}Sr_{0.16}CuO_4$, a prototype cuprate superconductor. The large-amplitude terahertz pulses allow to explore nonlinear modes in the layered superconductor without inducing dissipation by breaking Cooper-pairs.

[†]See for instance http://www.hzdr.de/FELBE

In a first experiment conducted in the Oxford laboratory, broadband pulses tuned well below the 2-THz plasma resonance are generated by the tilted pulse front technique and used to bi-directionally gate interlayer transport in the cuprate. Because the applied pulses are so short, electric fields in excess of 100 kV/cm can be applied without significant heating or damage of the material, making it possible to study the response in unprecedented fields. Oscillations between the superconducting and normal states are observed, as the conduction through Cooper-pairs is shut on and off by the gate field. This study demonstrates the equivalent of transistor action at ultrafast speeds, and may be of importance as a component in opto-electronic devices. It also demonstrates the existence of a new non-equilibrium phenomenon in high-T_c superconductivity, as the dimensionality of the system is made time-dependent. Indeed, the superconducting properties are modulated only along the c-direction, whilst they remain unperturbed within the ab-planes (Dienst *et al.*, 2011a).

In a second experiment, narrowband terahertz pulses generated at the free electron laser in Dresden are tuned close to the Josephson resonance frequency and used to optically inject large-amplitude nonlinear plasma waves into the cuprate, giving rise to a metastable state that is transparent over a narrow spectral region. The observation is interpreted as the result of disruptive quantum interference between the linear plasma waves of the material and the resonantly excited Josephson vortex train, which exhibits the periodicity of the driving electromagnetic wave. Here, the vortices act as long-lived dark states, and the observed transparency can be simulated with a model of coupled oscillators. The experiment demonstrates the potential of layered superconductors for quantum nonlinear optics and shows how such effects make it possible to track vortex excitations on picosecond timescales (Dienst *et al.*, 2011c).

This thesis is organised as follows. Chapter 2 contemplates the principles of light-matter interaction and explains based on experimental data how nonlinear terahertz spectroscopy can be applied to study the time-resolved optical properties of materials. In chapter 3, an introduction to the field of superconductivity is given, highlighting

anisotropic high-temperature compounds. Chapter 4 outlines the Josephson physics needed to interpret the non-equilibrium phenomena observed in this work. Chapter 5 discusses the layered cuprate $La_{2-x}Sr_xCuO_4$ in more detail and presents the equilibrium properties measured by terahertz time-domain spectroscopy. The observation of bi-directional electric-field gating of superconductive transport in $La_{2-x}Sr_xCuO_4$ is reported in chapter 6. In chapter 7, results on quantum interference optical transparency by resonant excitation of nonlinear plasma modes in $La_{2-x}Sr_xCuO_4$ are presented. The thesis closes with the summary and outlook of chapter 8.

Chapter 2

Introduction to Terahertz Science

The term terahertz (THz) radiation generally refers to electromagnetic waves having frequencies of the order of $\sim 10^{12}$ Hz = 1 THz. More specifically, the terahertz range is often defined to lie in the interval between 0.1 THz to 10 THz. With the corresponding wavelengths ranging from 3 mm to 30 μm, terahertz radiation is situated between the microwave and infrared region of the electromagnetic spectrum as indicated in figure 2.1. Existing methods of radiation generation and detection in these well-established neighbouring regions based on electronic and semiconductor technology have turned out to be not applicable in the terahertz regime. This fact, together with the high degree of atmospheric absorption, has resulted in a historic lack of suitable terahertz sources and detectors (Ferguson and Zhang, 2002).

In the field of condensed matter research, however, terahertz science is of critical importance. Many fundamental excitations in metals, semiconductors, or superconductors are in resonance with terahertz photons. Examples include phonon modes, interband transitions, or the Josephson plasma resonance. Moreover, inelastic processes such as quasiparticle scattering occur with rates within the terahertz region. During the last 30 years, a surging interest in complex materials accompanied by the development of novel detectors and high-intensity sources has led to a renewed interest in the field of terahertz science. These novel high-intensity techniques open new opportunities to achieve nonlinear terahertz spectroscopy in correlated systems.

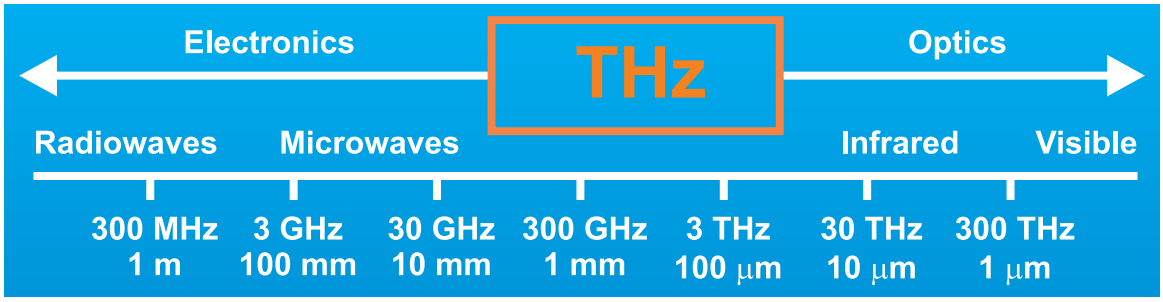


Figure 2.1: The electromagnetic spectrum. The terahertz frequency domain is situated between the microwave and infrared region, marking the transition from electronics to optics.

The first part of this chapter presents principles of light-matter interaction. Second, terahertz time-domain spectroscopy is introduced as a probe of the optical properties. Third, the functionality of two broad- and narrowband high-intensity terahertz sources is discussed. Fourth, time-resolved pump-probe techniques are introduced.

2.1 Optical Probes of Matter

Spectroscopy denotes a family of methods that extract material-specific information from the elastic and inelastic interaction of matter and radiated energy, such as neutrons, electrons or electromagnetic radiation. Using photons as a probe, the optical conductivity of the medium can be introduced through Maxwell's equations reading in the centimetre-gram-second (CGS) system of units[†] (Jackson, 1999; Lee, 2009)

$$\nabla \times \boldsymbol{H} - \frac{1}{c}\frac{\partial \boldsymbol{D}}{\partial t} = \frac{4\pi}{c}\boldsymbol{j} \quad , \tag{2.1}$$

$$\nabla \times \boldsymbol{E} + \frac{1}{c}\frac{\partial \boldsymbol{B}}{\partial t} = 0 \quad , \tag{2.2}$$

$$\nabla \cdot \boldsymbol{D} = 0 \quad , \tag{2.3}$$

$$\nabla \cdot \boldsymbol{B} = 0 \quad , \tag{2.4}$$

where $\boldsymbol{H}$ is the magnetic H-field, $\boldsymbol{D}$ is the displacement field, $\boldsymbol{E}$ is the electric field, $\boldsymbol{B}$ is the magnetic field, $\boldsymbol{j}$ is the electric current density, and c denotes the speed of light. ∇ symbolises the vector differential operator del, acting with respect to the spatial

[†]For a conversion table see http://en.wikipedia.org/wiki/Centimetre_gram_second_system_of_units

coordinate $\boldsymbol{r}$. The constitutive equations describe the material-specific response of bound charge and current to the externally applied fields as (Dresselhaus, 2011)

$$\boldsymbol{D} = \epsilon' \boldsymbol{E} \quad , \tag{2.5}$$

$$\boldsymbol{B} = \mu \boldsymbol{H} \quad , \tag{2.6}$$

$$\boldsymbol{j} = \sigma' \boldsymbol{E} \quad . \tag{2.7}$$

The quantities ϵ' and σ' are used in the following to derive the concept of a complex permittivity and conductivity, respectively. Combining Maxwell's equations with the constitutive equations, one obtains two equivalent wave equations for the field variables $\boldsymbol{E}$ and $\boldsymbol{H}$ reading

$$\nabla^2 \boldsymbol{E} = \frac{\epsilon' \mu}{c^2} \frac{\partial^2 \boldsymbol{E}}{\partial t^2} + \frac{4\pi\sigma' \mu}{c^2} \frac{\partial \boldsymbol{E}}{\partial t} \quad , \tag{2.8}$$

$$\nabla^2 \boldsymbol{H} = \frac{\epsilon' \mu}{c^2} \frac{\partial^2 \boldsymbol{H}}{\partial t^2} + \frac{4\pi\sigma' \mu}{c^2} \frac{\partial \boldsymbol{H}}{\partial t} \quad . \tag{2.9}$$

A solution of (2.8) can be found in the form of $\boldsymbol{E} = \boldsymbol{E}_0 \exp\{i(\boldsymbol{K} \cdot \boldsymbol{r} - \omega t)\}$, with the complex propagation constant $\boldsymbol{K}$ and the light frequency ω. The real part of $\boldsymbol{K}$ has the function of a wave vector, while the imaginary part represents attenuation of the wave in the medium. The plane wave dispersion relation reads

$$K^2 = \frac{\epsilon' \mu \, \omega^2}{c^2} + i \frac{4\pi\sigma' \mu \, \omega}{c^2} \quad , \tag{2.10}$$

giving rise to the well-known relationship $K_0 = \sqrt{\epsilon' \mu} \, \omega / c$ in case of vanishing attenuation. Introducing the material's complex permittivity as

$$\epsilon = \epsilon' + i \frac{4\pi\sigma'}{\omega} = \epsilon_1 + i\epsilon_2 \quad , \tag{2.11}$$

the general dispersion relation (2.10) in case of finite attenuation can be written equivalently in the form $K = \sqrt{\epsilon \mu} \, \omega / c$. In the same manner, a complex material-

specific optical conductivity σ can be introduced by the expression

$$\epsilon = i\frac{4\pi}{\omega}\sigma \quad , \tag{2.12}$$

where the conductivity is defined as

$$\sigma = \sigma' - i\frac{\epsilon'\omega}{4\pi} = \sigma_1 + i\sigma_2 \quad . \tag{2.13}$$

Equivalently to the permittivity and conductivity, the material's optical properties are captured by the complex frequency-dependent refractive index, which is given by

$$n = \frac{c}{\omega}K = \sqrt{\mu\epsilon} = n' + ik \quad . \tag{2.14}$$

Here, the real part n' defines the phase speed of light waves, $c' = c/n'$, in the specimen. The imaginary part k is called extinction coefficient and represents the amount of absorption losses. The meaning of the extinction coefficient becomes immediately clear when considering that an electromagnetic wave propagating along the x-direction through a medium with finite conductivity is represented by

$$\boldsymbol{E}(x,t) = \boldsymbol{E}_0 \exp(-i\omega t) \exp\left(i\frac{\omega n}{c}x\right) \quad . \tag{2.15}$$

Hence, the wave amplitude decays exponentially over a characteristic length d reading

$$d = \frac{c}{\omega k} \quad , \tag{2.16}$$

which is commonly referred to as skin depth. The inverse absorption coefficient defines the distance at which the intensity of the wave $|\boldsymbol{E}(x,t)|^2$ has fallen to $1/\exp(1)$ of its maximum value at the surface and is given by

$$\frac{1}{\alpha_{abs}} = \frac{c}{2\omega k} \quad . \tag{2.17}$$

It has to be emphasised that in general the optical properties introduced above depend on the frequency of the incident electromagnetic radiation. The aim in spectroscopy is then to link the frequency-dependent complex quantities $\sigma(\omega)$, $\epsilon(\omega)$, and $n(\omega)$ to physical observables such as the reflectivity. The microscopic physical processes in the specimen can then be described in terms of the optical properties employing suitable theoretical models that relate experiment and theory.

In conventional optical absorption spectroscopy, probe light is brought into interaction with a specimen. The absorption coefficient (2.17) is then determined as the fraction of incident intensity absorbed by the material for a given frequency interval. The same analysis can be conducted using the reflected or transmitted part, since reflection and transmission are related by a simple mathematical transformation. This type of spectroscopy only allows for the immediate determination of the extinction coefficient k, since it captures only the intensity reflectivity while neglecting all phase-related information (Kittel, 2005).

Through Kramers-Kronig analysis, which relates the real and imaginary part of a complex function, one can extract the real refractive index n' after having measured k (Roessler, 1965). However, this determination of the real part n' requires assumptions about the behaviour of the imaginary part k in the limits $\omega \to 0$ and $\omega \to \infty$. It does not constitute a direct and independent measurement.

In contrast to absorption spectroscopy, terahertz time-domain spectroscopy allows for the simultaneous determination of real and imaginary part of the refractive index n using Fresnel's equations. This becomes possible because the terahertz traces are generated and detected coherently, retaining amplitude and phase related information (see section 2.2 for experimental details).

Fresnel's Equations

The electric field amplitude and phase of a terahertz transient which is reflected off a specimen are directly related to the material's complex refractive index through

Fresnel's equations. If the polarisation of the probing beam is perpendicular to the plane of incidence as depicted in figure 2.2 A, the complex reflection coefficient r for a wave travelling from a medium with refractive index n_1 to a medium with index n_2 is given by (Born and Wolf, 1975; Saleh and Teich, 1991)

$$r = \frac{n_1 \cos\alpha_1 - n_2 \cos\alpha_2}{n_1 \cos\alpha_1 + n_2 \cos\alpha_2} \quad , \tag{2.18}$$

where α_1 and α_2 denote the angles of incidence and refraction. For light incident from vacuum ($n_1 = 1$) onto a conductor, note that the angle of refraction α_2 in the material becomes complex. The reflection coefficient is defined as the ratio of the Fourier transforms of the time-dependent reflected field and the incoming one as $r(\omega) = E_{ref}(\omega)/E_{inc}(\omega)$. Sometimes it is convenient to display r in its polar form

$$r(\omega) = |r(\omega)| \exp\{i\delta(\omega)\} \quad . \tag{2.19}$$

Here, $\delta(\omega) = \delta_{ref}(\omega) - \delta_{inc}(\omega)$ defines the frequency-dependent phase difference of the Fourier transforms of the reflected and incoming electric fields. Together with Snell's law reading

$$\cos\alpha_2 = \sqrt{1 - \left(\frac{n_1}{n_2}\right)^2 \sin^2\alpha_1} \quad , \tag{2.20}$$

the Fresnel relation (2.18) can be inverted to obtain n_2 as a function of α_1, n_1 and r.

Under the experimental condition encountered in this thesis, the probe radiation is incident from vacuum ($n_1 = 1$) at an angle of $\alpha_1 = 45°$. Then, the real and imaginary part of the permittivity can be calculated as

$$\mathrm{Re}(\epsilon) = \frac{\xi^2 - \zeta^2 + 1}{2} \quad , \tag{2.21}$$

$$\mathrm{Im}(\epsilon) = \xi\zeta \quad , \tag{2.22}$$

where ξ and ζ are determined by the amplitude $|r|$ and phase δ as (Jepsen and Fischer,

2005; Roessler, 1965)

$$\xi = \frac{1 - |r|^2}{1 + |r|^2 + 2|r|\cos\delta} \quad , \tag{2.23}$$

$$\zeta = \frac{2|r|\sin\delta}{1 + |r|^2 + 2|r|\cos\delta} \quad . \tag{2.24}$$

Equations (2.21)-(2.24) provide the mathematical foundation to determine the static optical properties in the terahertz time-domain spectroscopy experiments reported in this thesis. How a terahertz spectroscopy apparatus is implemented experimentally is outlined in the remaining part of this chapter.

2.2 Terahertz Time-Domain Spectroscopy

Terahertz time-domain spectroscopy utilises single-cycle electromagnetic transients generated opto-electronically based on femtosecond-duration laser pulses. The sub-picosecond time resolution allows for the coherent detection of the transient electric field, determining both amplitude and phase of the pulse's spectral components.

Figure 2.2 B depicts a typical terahertz time-domain spectroscopy setup used in the experiments described in this thesis. Near-infrared radiation with a central wavelength of $\sim$ 800 nm is delivered by a titanium-doped sapphire laser, providing pulsed radiation at repetition rates in the kHz to MHz regime. The pulse duration accounts for $\sim$ 100 fs, while the relative spectral width is $\sim$ 2 %. A beamsplitter divides the laser output of several Watts average power. The main share of the split beam is used to generate single-cycle terahertz pulses. For the terahertz sources utilised in the experiments presented here, two generation mechanism are distinguished:

(i) When using a 1 kHz amplified laser system providing 3.7 W average output power, terahertz transients are generated by optical rectification of the near-infrared pulses in (110)-cut zinc telluride (ZnTe) crystals. Optical rectification is a second-order nonlinear process based on difference frequency generation in electro-optic crystals (Ma and Zhang, 1993). The principle here is that the ith polarisation component

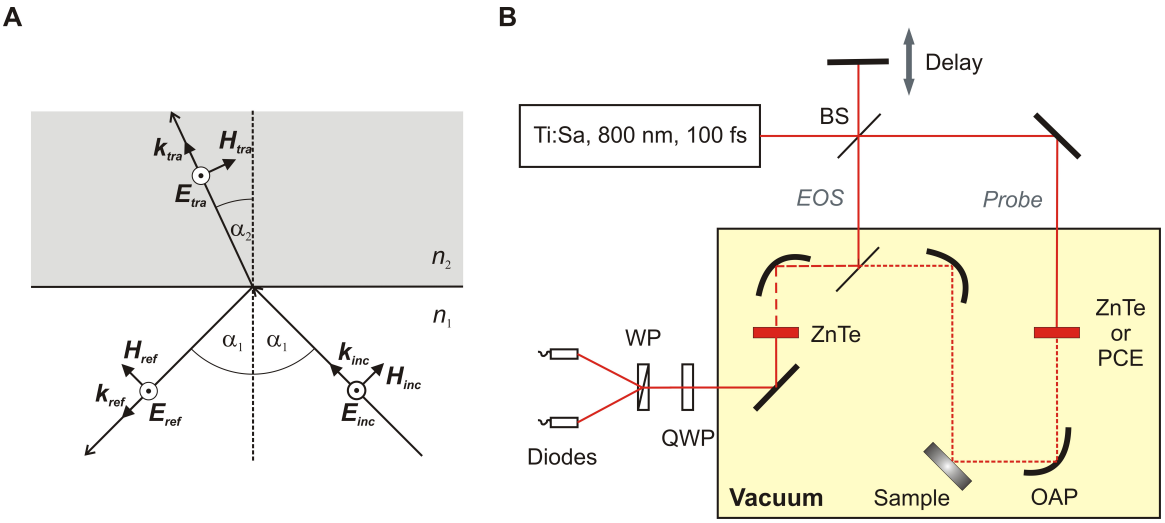


Figure 2.2: Refraction of light and terahertz time-domain spectroscopy. A: Reflection and transmission of incident electromagnetic radiation at the interface between two materials with refractive indices n_1 and n_2. The electric field is polarised perpendicular to the plane of incidence. B: Schematic of a typical terahertz time-domain spectroscopy setup based on a femtosecond titanium-doped sapphire laser. The radiation is generated by optical rectification in zinc telluride (ZnTe) or a photoconductive emitter (PCE), while the detection is achieved by electro-optic sampling in ZnTe.

in the medium essentially follows the intensity envelope of the excitation field as

$$P_i(\Omega) = \int_{\nu_0-\Delta\nu/2}^{\nu_0+\Delta\nu/2} \chi_{ijk}(\Omega,\nu) E_j(\nu+\Omega) E_k^*(\nu) \mathrm{d}\nu \quad , \tag{2.25}$$

where the incident light beam has the central frequency ν_0 and bandwidth $\Delta\nu$, while χ_{ijk} is the nonlinear susceptibility tensor element of the material. $E_j(\nu)$ denotes the Fourier transform of the time-dependent near-infrared electric field component j. By dipole far-field approximation, the emitted electromagnetic amplitude spectrum $E_{THz}(\Omega)$ is directly proportional to the induced polarisation $E_{THz}(\Omega) \propto \Omega^2 P(\Omega)$, and the generated terahertz pulses contain frequency components Ω ranging from d. c. to $\Delta\nu$. For efficient interaction of the femtosecond light field with the polarisation modulation in the crystal, it is necessary that near-infrared group- and terahertz phase-velocity match. This condition is met in zinc telluride for excitation wavelengths of $\sim$ 800 nm in a collinear geometry. Because of the high excitation pulse intensities necessary, optical rectification is often used with amplified kHz laser systems.

(*ii*) When working with 13 MHz oscillators, the higher pulse repetition rates available make the use of a photoconductive emitter (PCE) for terahertz generation more

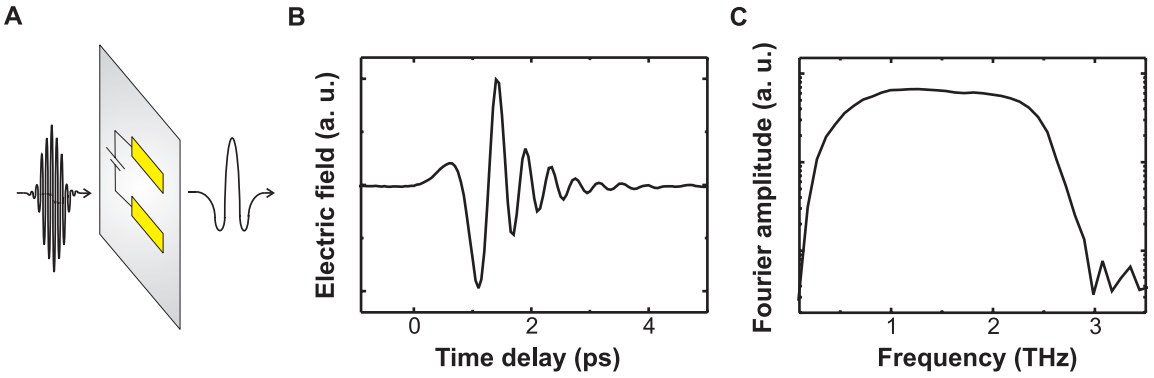


Figure 2.3: Photoconductive terahertz emitter. A: Sketch of a photoconductive emitter. A femtosecond laser pulse is focused in between two electrodes deposited on a semiconductor substrate. The generated photo-carriers are accelerated by a bias voltage, emitting a short terahertz pulse. B: Electric field of terahertz transient generated with an emitter and measured by electro-optic sampling in ZnTe. C: Spectrum obtained by computing the Fourier amplitude of the electric field in panel B.

favourable. In such a photoconductive antenna, two metal electrodes are assembled on a semiconductor substrate, and biased with a constant voltage. Optical near-infrared pulses are focussed onto the gap in between the electrodes, generating photocarriers which are accelerated by the bias field. The temporal evolution of the photocurrent is dictated by the intensity envelope of the femtosecond excitation, giving rise to radiation of single-cycle terahertz pulses. Usually the generated terahertz fields are lower than compared to optical rectification. Figure 2.3 A shows a schematic of a typical antenna. Geometric parameters such as the electrode distance determine together with excitation pulse characteristics, strength of applied voltage, and material properties the emitted spectrum.

The terahertz probe pulses are subsequently focussed onto the sample at an incident angle of 45° (with respect to the surface normal) using an off-axis parabola (OAP). After reflection off the sample, the pulses are collimated, and subsequently focussed onto a 1 mm-thick zinc telluride detection crystal. The small remaining fraction of the 800 nm light which is reflected from the beamsplitter is used to gate the far-infrared radiation in the zinc telluride detection crystal by electro-optic sampling (EOS). This detection technique is based on an induced refractive index change in the zinc telluride crystal caused by the coincident terahertz radiation ($\Delta n \propto E_{THz}$). The transient birefringence results in a polarisation rotation of the EOS beam, which can

be mapped using a combination of quarter wave plate (QWP), Wollaston prism (WP), and balanced photodiode scheme. Since the intensity difference on both photodiodes is linearly proportional to the applied terahertz field strength ($\Delta I \propto E_{THz}$), a direct observation of the probe electric field becomes possible (Parc *et al.*, 2008).

To scan entire terahertz traces, probe and EOS pulses have to be mutually adjusted in time using an optical delay stage. The sub-picosecond time resolution necessary to detect the terahertz transients is limited by the EOS pulse duration and the coherence length of terahertz and optical pulses within the zinc telluride crystal. In a 1 mm long crystal that corresponds to 3 THz (Nahata *et al.*, 1996), resulting in a temporal resolution of about 150 fs. The signal, which is generated by the balanced photodiodes, is amplified by a phase-sensitive detector and acquired by a computer together with the delay line position. A data acquisition program, which had to be developed for this application, allows real time data analysis. An exemplary time-domain terahertz trace and the corresponding Fourier amplitude, generated by an emitter and measured after reflection from a gold sample, are shown in figure 2.3 B and C, respectively.

2.3 High-Intensity Terahertz Sources

Conventional optical rectification of femtosecond near-infrared laser radiation in zinc telluride produces terahertz pulses of nanojoule energy and electric fields reaching few kilovolts per centimetre. These terahertz fields are often suitable to investigate the linear optical properties of matter. If one wishes to study nonlinear phenomena, one has to resort to alternative generation schemes capable of producing terahertz pulses of much higher intensity. In the following, two generation mechanisms are introduced that provide microjoule pulse energies and electric fields reaching hundreds of kilovolts per centimetre. The first method is based on tilted pulse front excitation in lithium niobate crystals and represents a table-top setup producing broad-bandwidth single-cycle radiation. The second technique generates narrow-bandwidth multi-cycle pulses using a large-scale free electron laser.

Tilted Pulse Front Technique

It is crucial for efficient optical rectification that the near-infrared group velocity v_{NIR} matches the terahertz phase velocity v_{THz}. For experimental simplicity, a collinear geometry is often chosen, in which the near-infrared pulses propagate parallel to the terahertz radiation in phonon-polariton form. Since these requirements are fulfilled by gallium phosphide or zinc telluride crystals and near-infrared excitation wavelengths of about 800 nm, these materials are commonly employed for optical rectification. However, the nonlinear susceptibility χ (see equation (2.25) above) of zinc telluride is considerably smaller than that of comparable nonlinear optical materials such as lithium niobate ($LiNbO_3$).

Apart from the higher nonlinear susceptibility, lithium niobate has a further very important advantage over zinc telluride. Zinc telluride is a semiconductor with comparably small bandgap, leading to two-photon absorption of the 800 nm pump pulses. The induced free carriers cause strong terahertz absorption saturating the terahertz conversion efficiency when increasing the near-infrared pump power (Löffler *et al.*, 2005). The bandgap of lithium niobate is much larger, preventing two-photon absorption and allowing for higher excitation powers (Redfield and Burke, 1974).

The utilisation of lithium niobate for optical rectification, however, has been hindered in the past mainly because the near-infrared group velocity is about twice as large as the terahertz phase velocity (Hebling *et al.*, 2002).

Recent technological progress has overcome the problem of phase matching in lithium niobate (Hebling *et al.*, 2002, 2008a). Figure 2.4 A shows a schematic of the generation mechanism. The novel idea is to tilt the intensity front of the near-infrared radiation by an angle γ, such that the modified phase matching condition

$$v_{NIR} \cos\gamma = v_{THz} \quad , \tag{2.26}$$

can be fulfilled. Using literature values for both v_{NIR} and v_{THz} (Hebling *et al.*,

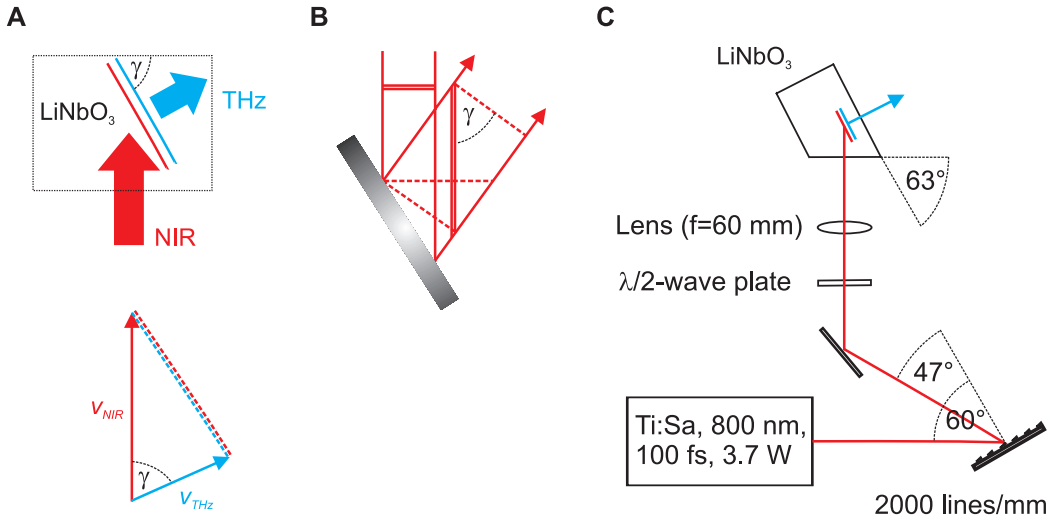


Figure 2.4: Tilted pulse front generation in lithium niobate crystals. A: The pulse front of the near-infrared excitation laser is tilted by an angle γ to fulfil the phase matching condition. B: The optimum pulse front tilt is achieved by diffracting the laser beam off a grating at an appropriate angle. C: Near-infrared pulses of $\sim$ 100 fs duration produced by a titanium-doped sapphire laser are incident on a grating with 2000 lines/mm. After tilting of the pulse front, the polarisation is rotated by 90° using a $\lambda/2$-wave plate. As described in (Hebling *et al.*, 2002), a lens with 60 mm focal length images the laser spot at the grating position onto the appropriately cut lithium niobate crystal, inside of which the high-intensity terahertz radiation is generated by optical rectification.

2008a), the optimum tilt angle inside the crystal accounts for $\gamma = 63°$. Because the pulse front tilt decreases upon entering lithium niobate from vacuum according to $n_{NIR} \tan\gamma = \tan\tilde{\gamma}$, the desired angle outside of the material increases to $\tilde{\gamma} = 78°$.

It is known that such high tilt angles can be achieved by diffracting the near-infrared radiation off a grating (Bor *et al.*, 1993). Figure 2.4 B depicts the formation of the pulse front tilt. Using the grating equations, one can show that the phase front tilt angle $\tilde{\gamma}$ is given by

$$\tan\tilde{\gamma} = \lambda \frac{d\alpha_2}{d\lambda} \quad , \tag{2.27}$$

where λ is the wavelength, and α_2 the diffraction angle. The term $d\alpha_2/d\lambda$ denotes the angular dispersion of the grating, which is determined by diffraction angle, diffraction order, and grating line separation (Bor *et al.*, 1993). Combining equations (2.26) and (2.27) allows to optimise the phase matching condition by adjusting the grating angle.

Figure 2.4 C details the experimental realisation of the tilted pulse front setup built in the laboratory. An amplified titanium-doped sapphire laser generates pulses

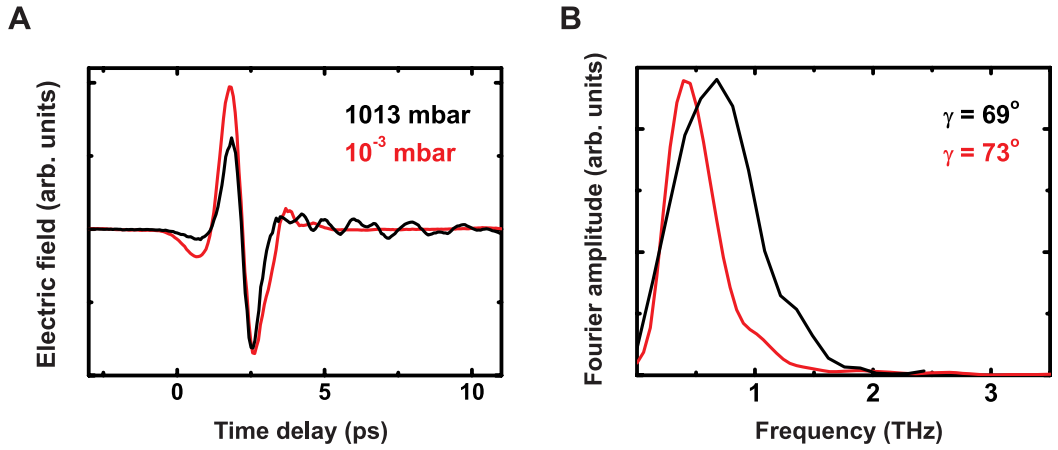


Figure 2.5: Time- and frequency-domain of the high-intensity terahertz pulses. A: Time-dependent electric field measured by electro-optic sampling of the high-intensity pulses for atmospheric and low pressure. The ringing on the trailing edge of the pulse is caused by absorption and coherent re-radiation through water vapour, which is strongly suppressed below 1 mbar. Both curves have the same arbitrary units. B: Normalised Fourier amplitude of pump transients as a function of frequency measured for two different pulse front tilt angles γ. By adjusting γ, the spectrum can be tuned to match the experimental requirements.

of $\sim$ 100 fs duration with a central wavelength of $\sim$ 800 nm. The average laser power is 3.7 W at a repetition rate of 1 kHz. The laser beam is incident on a blazed grating with 2000 lines/cm. To minimise loss at the grating, the polarisation is parallel to the plane of incidence. After diffraction off the grating, a $\lambda/2$-wave plate rotates the polarisation by 90° to be parallel to the optical axis of the lithium niobate crystal. This is important for efficient radiation generation, because the corresponding nonlinear susceptibility tensor element (compare equation (2.25) above) is maximum. A lens with a focal length of 60 mm is used to image the laser spot at the grating onto the lithium niobate crystal, employing a demagnification factor of 2. The demagnification leads to a doubling of the tangent of the tilt angle, effectively reducing the optimum tilt angle after the grating to $\tilde{\gamma} \approx 67°$ in this configuration. The spot sizes at the grating and the lithium niobate crystal are chosen such that the damaging thresholds are not exceeded, accounting for beam diameters of $\sim$ 8 mm and $\sim$ 4 mm, respectively.

Figure 2.5 A shows a typical high-intensity terahertz transient measured by electro-optic sampling in zinc telluride. The graph compares two traces taken at atmospheric pressure and under vacuum conditions. The ringing following the pulse measured at atmospheric pressure is due to absorption and re-radiation by water vapour, which is

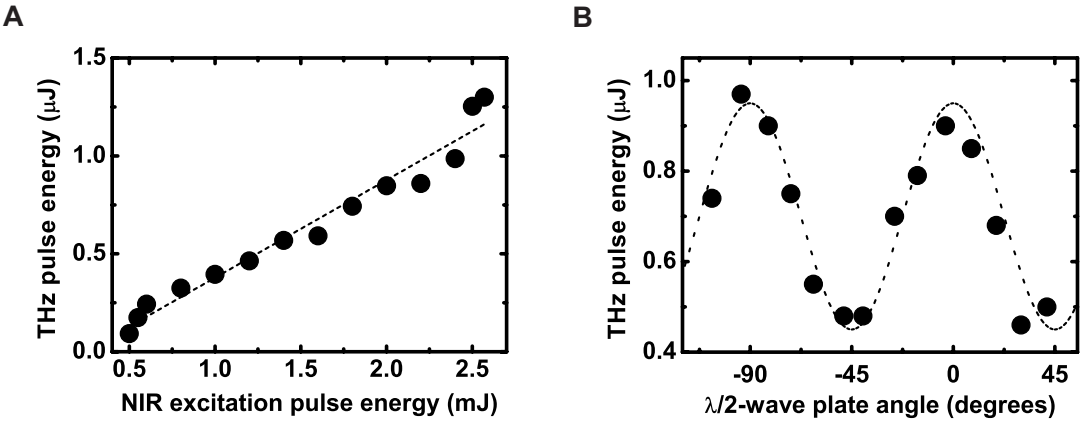


Figure 2.6: Determination of terahertz pulse energies. A: Measurements of the high-intensity terahertz pulse energy in dependence of near-infrared excitation pulse energy, revealing a roughly linear relationship. Here, the maximum achievable pulse energy is ∼1.3 μJ. B: Terahertz pulse energy as a function of the $\lambda/2$-wave plate angle. As the wave plate is rotated and the polarisation altered from its optimum alignment parallel to the optical axis of $LiNbO_3$, the generation efficiency decreases. A second maximum is reached when the wave plate is turned by 90°, corresponding to a rotation of the polarisation by 180°. The experimental data can be fit with a function $\propto \cos^2(2\beta)$, where β is the wave plate rotation angle with respect to the optimum configuration at $\beta = 0$.

suppressed strongly below 1 mbar. Figure 2.5 B shows two typical spectra. Through adjustment of the pulse front tilt angle, the centre frequency can be tuned to match the specific experimental requirements.

The energy of the sub-millimetre radiation can be determined with a calibrated pyroelectric detector. Figure 2.6 A displays the terahertz pulse energy as a function of the near-infrared excitation pulse energy measured after and before the lithium niobate crystal position, respectively. In the energy interval shown, the relationship between excitation and terahertz pulse energy is roughly linear, which is in agreement with previous measurements (Hebling *et al.*, 2008a).

Rotating the $\lambda/2$-wave plate highlights the terahertz generation efficiency in dependence of the near-infrared polarisation orientation. Measurements of the terahertz pulse energy as a function of the wave plate rotation angle are shown in figure 2.6 B. When the near-infrared polarisation is parallel to the optical axis of the nonlinear crystal, the generation efficiency is maximum. When the wave plate is rotated by 45°, corresponding to a polarisation rotation of 90°, the generated terahertz pulse energy takes on a minimum value. The experimental data can be well-fitted by a function $\propto \cos^2(2\beta)$, where β is the angle of rotation.

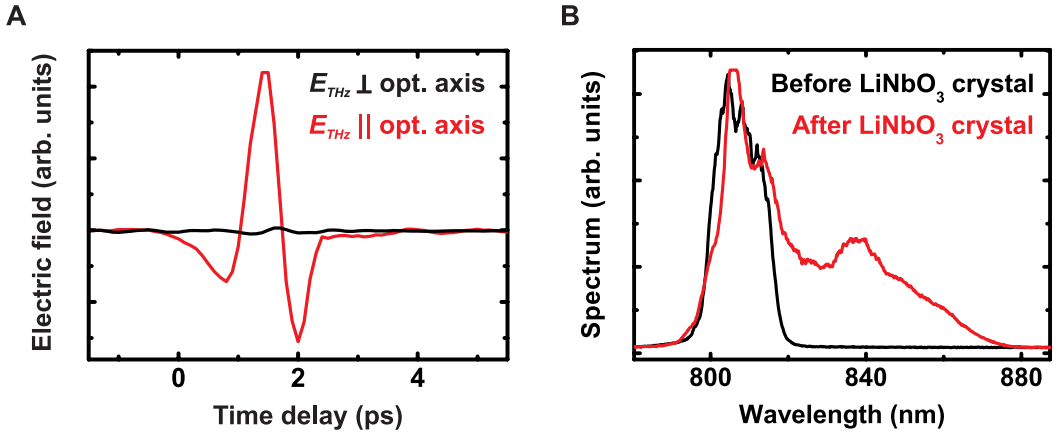


Figure 2.7: Terahertz polarisation and near-infrared spectra. A: Polarisation-sensitive measurements of time-dependent terahertz transients. The near-infrared excitation field is polarised parallel to the $LiNbO_3$ crystal axis. A terahertz polariser is inserted into the beam path, and the transmitted radiation polarised parallel and perpendicular to the optical axis of $LiNbO_3$ is probed. The transients are found to be essentially polarised parallel to the optical axis. B: Scaled spectra of the titanium-sapphire laser recorded before and after interaction with the lithium niobate crystal. As previously observed in (Hebling *et al.*, 2008a), the spectrum develops a broad shoulder on the low-energy side due to the cascade-like difference frequency generation in the nonlinear crystal.

Inserting a terahertz polariser in the beam path allows to probe the polarisation of the terahertz pulses. Figure 2.7 A shows polarisation-dependent measurements of the pump transients. For the near-infrared polarisation oriented parallel to the crystal *c*-axis, the terahertz pulses are essentially linearly polarised in the same direction.

The terahertz generation process also alters the near-infrared excitation spectrum. Figure 2.7 B depicts scaled titanium-sapphire laser spectra measured before and after passing through the lithium niobate crystal. After interaction with the nonlinear material, a pronounced broadening of the red side of the spectrum is observed, indicating that the cascading process of difference-frequency generation is the major cause of the spectral shift (Hebling *et al.*, 2008b).

The tilted pulse front technique can generate broadband high-intensity terahertz pulses using a table-top setup. Indeed, it is possible to significantly narrow the spectra by splitting the optical excitation radiation into several collinear pulses using parallel partial reflectors with adjustable spatial separation ($\sim$ 100 µm), leading to multi-cycle pulse sequences (Hebling *et al.*, 2008b). However, when relative spectral bandwidths of a few percent or less are required, one has to resort to free electron lasers.

Free Electron Laser Sources

Free electron lasers are large-scale facilities capable of providing tunable, spectrally brilliant, and coherent high-power electromagnetic radiation. The produced light has optical properties characteristic of conventional lasers, although the generation mechanism is based on free moving electrons as lasing medium in contrast to molecular or atomic transitions in solids, liquids and gases. The wavelengths that are achievable span from millimetre waves to hard x-rays, and the pulse duration can be as short as several pico- or femtoseconds (Huang and Kim, 2007).

In a free electron laser, relativistic electron bunches move freely through a magnetic structure called undulator. Due to the acceleration by the magnetic fields, the charge carriers emit photons. To illustrate the principle of light emission, figure 2.8 A shows an electron moving along the z-direction in a planar undulator. The magnetic field in the vertical y-direction varies sinusoidal as a function of the z-coordinate according to $B_y = B_0 \sin(k_u z)$. Thereby, B_0 denotes the magnetic pole field and $k_u = 2\pi/\lambda_u$, with λ_u being the undulator period. A relativistic electron with mass m entering a finite magnetic field wiggles in the horizontal x-direction and emits radiation along the undulator z-axis at the resonant wavelength (Huang and Kim, 2007)

$$\lambda_r = \frac{\lambda_u}{2\gamma_0^2}\left(1 + \frac{K_0^2}{2}\right) \quad . \tag{2.28}$$

Here, γ_0 represents the electron energy in terms of the rest energy mc^2, where c denotes the speed of light. The undulator strength parameter K_0 is defined by

$$K_0 = \frac{eB_0}{mck_u} = 9340 B_0[\text{Gauss}]\lambda_u[\text{cm}] \quad . \tag{2.29}$$

As can be seen from equations (2.28) and (2.29), the resonantly emitted wavelength can be tuned by adjusting the electron energy or undulator specifications. After entering the magnetic structure, spontaneous emission at the resonant wavelength constitutes the starting process of amplification. The emitted electromagnetic radia-

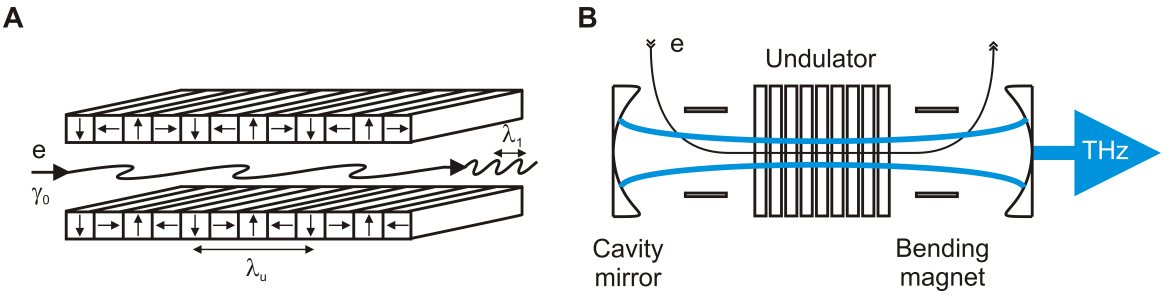


Figure 2.8: Operational principle of a free electron laser. A: Schematic of an electron with energy γ_0 entering an undulator with spatial periodicity λ_u. The electron's oscillatory motion leads to the emission of electromagnetic radiation with wavelength λ_1 (graph according to (Huang and Kim, 2007)). B: A bending magnet directs an accelerated electron into an undulator. In many free electron lasers, the magnetic structure is enclosed in an optical cavity to enhance the electron-photon interaction. A second bending magnet directs the electrons into a beam dump. A small hole in one cavity mirror couples part of the terahertz radiation out for delivery into the optical laboratories.

tion co-propagates in the forward direction together with the electron beam. In many free electron lasers operating in the terahertz regime, the undulator is confined in an optical cavity to enhance the interaction of photons and electrons (see figure 2.8 B).

The measurements presented in chapter 7 of this thesis were performed at the free electron laser ELBE in Dresden, Germany. The three main components of ELBE are the electron accelerator, the undulator and the optical resonator. As shown in the schematic in figure 2.8 B, a dipole bending magnet deflects the electron beam incident from the accelerator into the undulator. The wiggling electrons emit light into a narrow cone around the undulator axis, which is confined in an optical resonator consisting of two opposite focussing mirrors. A second bending magnet subsequently directs the electrons into a beam dump. The length of the cavity is tuned such that a cycling light pulse is coincident with the next electron bunch for optimum interaction during propagation. Stable operation of the free electron laser is achieved if all radiation losses are compensated for by the stimulated emission process. A hole in one of the cavity mirrors couples the 13-MHz pulse train out for delivery into the various scientific laboratories.

Figure 2.9 A shows a typical spectrum measured at ELBE. The relative spectral width for a centre frequency of $\omega/2\pi \approx 2$ THz is $\Delta\lambda/\lambda = 2.2$ %. Using a near-infrared laser oscillator whose repetition rate can be synchronised to the high-intensity pulse

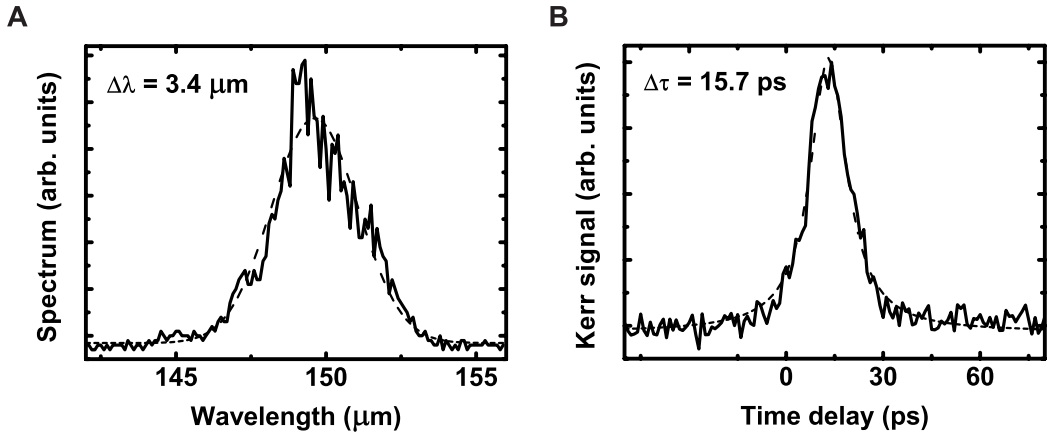


Figure 2.9: Characterisation of the free electron laser pulses. A: Spectrum of the free electron laser exhibiting a central wavelength of 150 μm, corresponding to 2 THz. The spectral width is measured to be $\Delta\lambda = 3.4$ μm assuming a Gaussian pulse shape (dashed line). B: Kerr signal as a function of time delay. The measurement is carried out according to the technique of (Hoffmann *et al.*, 2009) by electro-optic sampling of the free electron laser pulses in a zinc telluride crystal using a synchronised near-infrared laser oscillator. Under assumption of a Gaussian pulse shape (dashed line), the full width at half maximum of the Kerr signal amounts to $\Delta\tau = 15.7$ ps.

train, one can measure the pulse duration of the free electron laser by electro-optic sampling in zinc telluride. This is possible because the high-power terahertz pulses induce a refractive index change in the nonlinear material that follows the envelope of the square of the electric field ($\Delta n \propto E_{THz}^2$), a phenomenon called terahertz Kerr effect (Hoffmann *et al.*, 2009). Figure 2.9 B reports the Kerr signal as a function of time delay, giving rise to a full width at half maximum of $\Delta\tau = 15.7$ ps assuming a Gaussian pulse shape. The calculated time-bandwidth product is $\Delta\tau\Delta\omega/2\pi \approx 0.7$, which is close to Fourier-transform limited operation. The terahertz pulse duration can be tuned by adjusting the cavity mirror separation with respect to the nominal length which is determined by the electron bunch repetition rate. The power output is highest at minimum detuning (achieving ~ 5 W in the laboratories), when the pulse duration reaches its minimum. The spectral width can be decreased by detuning the resonator, resulting in an increase in pulse length[†].

By combining the high-intensity sources discussed in the present section with conventional low-fluence probe techniques, time-resolved nonlinear terahertz spectroscopy becomes possible as outlined in the following section.

[†]For further technical specifications of ELBE see http://www.hzdr.de/FELBE

2.4 Time-Resolved Spectroscopy

Terahertz time-domain spectroscopy as discussed in section 2.2 can be combined with the high-intensity sources described in section 2.3 in a terahertz pump, terahertz probe geometry. In such an experiment, the high-intensity excitation pulses induce a non-equilibrium state in a specimen. As a result, the optical properties of the material become time-dependent in a surface layer of thickness comparable to the penetration depth of the pump radiation. Low-field pulses are then used to probe the excited state by recording changes in the reflection coefficient. The relative time delay between probe and pump pulses is adjusted in a well-defined manner, giving access to the non-equilibrium dynamics with sub-picosecond temporal resolution.

Figure 2.10 A shows a schematic of a typical terahertz pump, terahertz probe setup. A titanium-sapphire laser provides near-infrared pulses with $\sim$ 100 fs duration at a centre wavelength of $\sim$ 800 nm. A terahertz time-domain spectroscopy setup identical to the one introduced in section 2.2 is used to probe the sample properties. The probe pulses are synchronised to a high-intensity terahertz source, and both beams are spatially and temporally overlapped at the sample position. The relative temporal delay between the pump and probe pulses can be controlled by offsetting the mutual phase-locked loop, or by controlling the optical delay line position. In all experiments discussed in this thesis, the terahertz generation, propagation, and detection takes place in vacuum to avoid absorption effects in air.

The pump-induced change in the sample's optical properties leads to a change $\Delta E(\omega)$ of the Fourier transform of the reflected terahertz probe transients $E(\omega)$. The main objective here is to deduce the non-equilibrium optical properties by measuring the modulation $\Delta E(\omega)$ as a function of pump-probe time delay. Subsequently, the out-of-equilibrium conductivity can be determined by inverting Fresnel's equations.

One common approach is to model the system response by considering a photo-excited surface layer of thickness d and unknown properties (n, ϵ, σ), over an unperturbed semi-infinite superconductor with the equilibrium optical constants $(\tilde{n}, \tilde{\epsilon}, \tilde{\sigma})$.

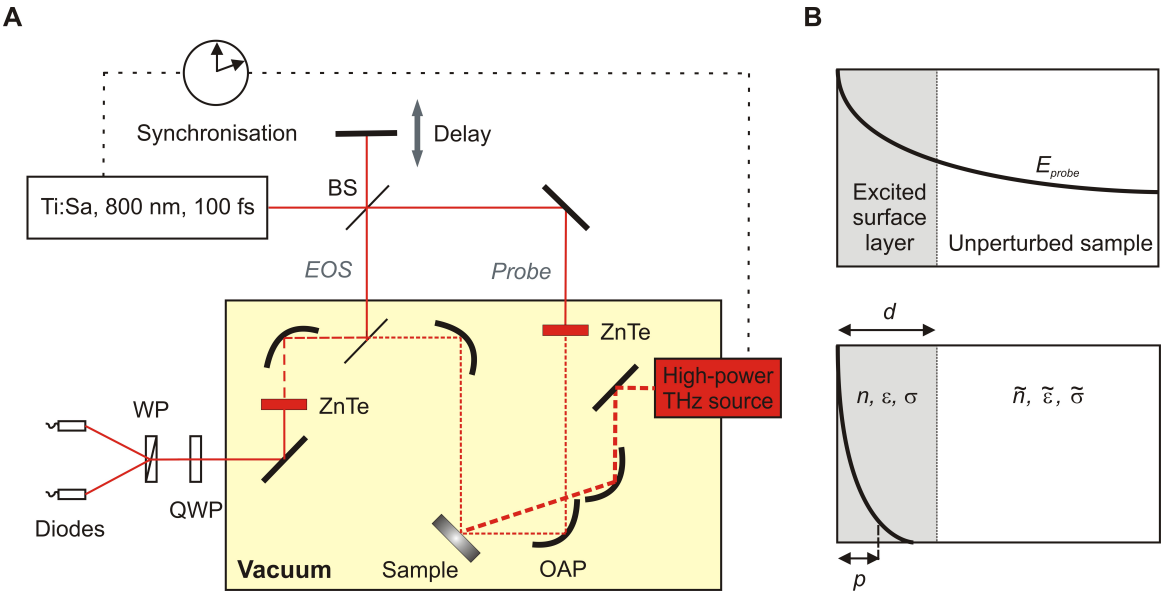


Figure 2.10: Terahertz pump, terahertz probe spectroscopy. A: A conventional terahertz time-domain spectroscopy apparatus is combined with a high-intensity terahertz source. Both, low-fluence probe and high-intensity pump radiation are spatially and temporally overlapped at the sample position. The relative time delay between pump and probe transients is controlled by off-setting the phase-locked loop that synchronises the titanium-sapphire laser with the high-intensity terahertz source. B: As contemplated in (Born and Wolf, 1975), it is assumed that the pump pulses produce a homogeneously excited surface layer of thickness d in the sample, in which the transient complex optical properties (n, ϵ, σ) deviate from their equilibrium values $(\tilde{n}, \tilde{\epsilon}, \tilde{\sigma})$ by an unknown amount. The upper panel depicts the situation when the probe penetration depth p is much larger than the surface thickness d. In the lower panel, the probe penetration depth is similar to the layer thickness.

A scheme of the excited surface layer is depicted in figure 2.10 B. The total reflected wave is represented by the complex reflection coefficient r as (Born and Wolf, 1975)

$$r = \frac{r_1 + r_2 \exp(i\delta)}{1 + r_1 r_2 \exp(i\delta)} \quad , \tag{2.30}$$

where $\delta = 4\pi dn\cos(\theta)/\lambda$. Hereby, n is the refractive index of the film, θ denotes the angle of diffraction, and λ is the probe wavelength. The variables r_1 and r_2 represent the reflection coefficients at the layer front and back surface, respectively.

Depending on the penetration depth d of the high-fluence pump pulses, different analysis techniques have to be employed for a given penetration depth p of the probe radiation. In the limit of long wavelengths and thin films when $p \gg d$, δ is sufficiently small so that the exponential in equation (2.30) can be approximated as $\exp(i\delta) \approx 1 + i\delta$. Then, it can be shown that for an incident angle of 45°, the change in the

complex out-of-equilibrium conductivity $\Delta\sigma = \sigma - \tilde{\sigma}$ is given by (Thoman *et al.*, 2008)

$$\Delta\sigma = \frac{1}{Z_0 d} \frac{\Delta E/E \left(\tilde{n}^2 \sqrt{1 - 1/(2\tilde{n}^2)} - 1/2 \right)}{\Delta E/E \left(1/\sqrt{2} - \tilde{n}\sqrt{1 - 1/(2\tilde{n}^2)} \right) + \sqrt{2}} \quad , \tag{2.31}$$

where Z_0 is the impedance of free space, $\tilde{n}$ the equilibrium refractive index, and $\Delta E(\omega)$ represents the pump-induced change of the Fourier transform of the reflected electric probe field $E(\omega)$. Equation (2.31) is commonly known as the thin-film approximation.

In another limiting case when the penetration depth of the pump radiation is very similar to the one of the probe, one is essentially examining a bulk sample with the out-of-equilibrium optical properties. In a situation where $|\exp(i\delta)| \ll 1$, the total Fresnel coefficient (2.30) simplifies to $r \approx r_1$, since one can neglect multiple reflections inside of the specimen. This latter approximation is commonly applied for optically-thick samples (Born and Wolf, 1975). Fresnel's equations for the equilibrium and out-of-equilibrium condition can then be combined and solved for the unknown film properties. For an incident angle of 45°, the perturbed complex permittivity ϵ can be determined from the expression

$$\epsilon = \frac{1}{2} \left(\frac{1 - (1 + \Delta E/E) \left(1 - \sqrt{2\tilde{n}^2 - 1} \right) / \left(1 + \sqrt{2\tilde{n}^2 - 1} \right)}{1 + (1 + \Delta E/E) \left(1 - \sqrt{2\tilde{n}^2 - 1} \right) / \left(1 + \sqrt{2\tilde{n}^2 - 1} \right)} \right)^2 + \frac{1}{2} \quad . \tag{2.32}$$

Under the assumption that the equilibrium optical properties are known, equations (2.31) or (2.32) can be employed (depending on the relative penetration depths of pump and probe) to calculate the time-dependent optical properties by recording the pump-induced changes in the reflection coefficient. In the context of pump-probe measurements, it is important to discuss the minimum temporal resolution of the results obtained. However, since this quantity depends on the exact experimental realisation, it is addressed in the chapters 6 and 7 of this thesis individually.

The following chapter introduces some basic concepts of superconductivity, in an effort to motivate time-resolved studies of these extraordinary materials. Attention is devoted to the anisotropic properties of layered cuprate superconductors.

Chapter 3

Introduction to Superconductivity

Electrical resistance is a measure for how strongly an electrical current through a medium is opposed by the material properties. In metals, resistance arises as a result of collisions of the charge carriers with lattice imperfections, impurities, or lattice vibrations. At room temperature, electron-phonon scattering dominates dissipation, whereby the other two processes prevail at low temperatures (Kittel, 2005).

The superconducting state is in part characterised by the disappearance of all electrical resistivity of a material, a phenomenon which was discovered in 1911 by H. K. Onnes. In his studies, Onnes monitored the conductivity of mercury at cryogenic temperatures, after having liquified helium for the first time in 1908 for use as a refrigerant. He showed that at a critical temperature (T_c) of 4.2 K, the resistivity dropped several orders of magnitude, marking the transition from conventional metallic conduction to a novel state of perfect conductivity, which later became known as superconductivity. In the subsequent decades, several other materials such as lead and niobium nitride were found to undergo the same transition at equally low temperatures that are close to the boiling point of liquid helium (4.2 K) (Tinkham, 1996).

The second fundamental property of the superconducting state was discovered in 1933 by W. Meissner and R. Ochsenfeld. In their observation, which became widely known as the Meissner effect, it was shown that a magnetic field within an originally normal specimen would be expelled as the sample is cooled below the critical

temperature (see figure 3.1 A). However, a perfect metallic conductor would tend to trap magnetic flux rather than give rise to perfect diamagnetism. Indeed, the Meissner effect could not be explained by invoking perfect conductivity alone and confirmed the notion that superconductivity is a fundamentally different state compared to conventional metallic conduction (Meissner and Ochsenfeld, 1933). In the years after the discovery of vanishing resistivity and the Meissner effect, several theoretical models of superconductivity were developed. Some concepts are outlined in the following.

3.1 Electrostatics of Superconductors

In 1935, the two brothers F. and H. London devised a phenomenological approach encapsulating the two fundamental characteristics of superconductivity within a mathematical framework. The two London equations describe the microscopic electrostatics of superconductors and reproduce perfect conductivity as well as perfect diamagnetism (London and London, 1935).

Although a rigorous derivation of the London equations from fundamental principles is not possible, one can gain an intuitive understanding of the basic properties of superconductivity from them. The theory's primary postulate asserts that the supercurrent density $\boldsymbol{J}_s$ is directly proportional to the vector potential $\boldsymbol{A}$, defining a weak microscopic magnetic field $\boldsymbol{B} = \nabla \times \boldsymbol{A}$. The two London equations then relate the supercurrent to the electric and magnetic field $\boldsymbol{E}$ and $\boldsymbol{B}$ as[†] (Tinkham, 1996)

$$\boldsymbol{E} = \frac{\partial}{\partial t}(\Lambda \boldsymbol{J}_s) \quad , \tag{3.1}$$

$$\boldsymbol{B} = -c\nabla \times (\Lambda \boldsymbol{J}_s) \quad . \tag{3.2}$$

The phenomenological parameter $\Lambda = 4\pi\lambda_L^2/c^2$ depends on the characteristic length λ_L, which is defined by $\lambda_L = \sqrt{mc^2/(4\pi n_s e^2)}$. Here, c is the speed of light, n_s the

[†]Note that the vector potential $\boldsymbol{A}$ is, unlike the observables $\boldsymbol{E}$, $\boldsymbol{B}$ and $\boldsymbol{J}_s$, not a uniquely-defined physical quantity, but depends on the gauge. In the following, the London gauge $\nabla \cdot \boldsymbol{A} = 0$ is used.

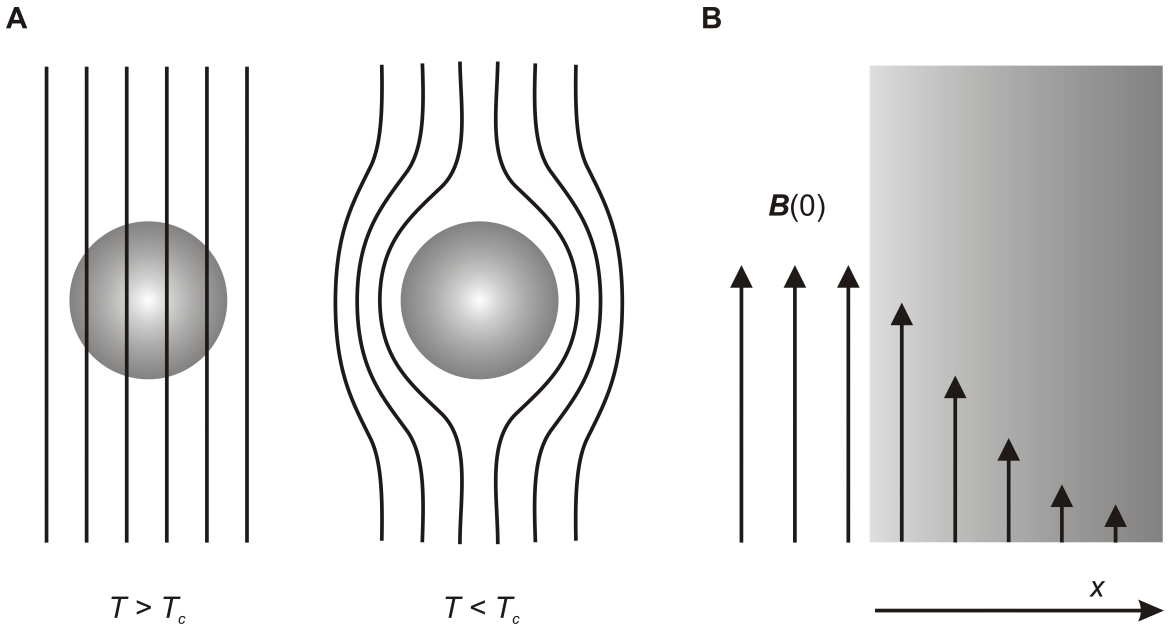


Figure 3.1: Illustration of the Meissner effect. A: A weak external magnetic field is applied to a superconductor. For temperatures above the transition temperature, the flux lines penetrate into the material. As the superconductor is cooled below the critical temperature, the magnetic field is expelled from the bulk sample. B: A magnetic field is applied perpendicular to the surface normal of a superconductor that occupies the half-space with $x > 0$. Inside the material, the magnetic field decays exponentially as $\boldsymbol{B}(x) = \boldsymbol{B}(0)\exp(-x/\lambda_L)$, whereby $\boldsymbol{B}(0)$ defines the magnetic field at the surface. The London penetration depth λ_L determines the distance over which the magnetic field amplitude is attenuated to 1/exp(1) of its maximum value at the surface (Kittel, 2005).

density of superconducting electrons, m their mass and e the electron charge.

The phenomenon of perfect conductivity is captured by the first London equation (3.1), stating that any electric field would accelerate the superconducting carriers rather than just sustaining their velocity against dissipative effects, as it is the case in a conventional metal described by Ohm's law ($\boldsymbol{J} = \sigma \boldsymbol{E}$).

Combining the second London equation with the Maxwell equation $\nabla \times \boldsymbol{B} = \frac{4\pi}{c}\boldsymbol{J}_s$, one finds for a superconductor a differential equation of the form

$$\nabla^2 \boldsymbol{B} = \frac{1}{\lambda_L^2}\boldsymbol{B} \quad . \tag{3.3}$$

This expression is encapsulating the Meissner effect, since it allows for the trivial case $\boldsymbol{B} = 0$, or a damped solution of the form $\boldsymbol{B}(x) = \boldsymbol{B}(0)\exp(-x/\lambda_L)$. Here, the magnetic field decays exponentially inside the sample, with the x-direction assumed to be perpendicular to the magnetic field and parallel to the surface normal as depicted

in figure 3.1 B. As a result of persistent superconducting currents, external magnetic fields are screened out in a distance λ_L from the surface. Using Maxwell's equations, it can be shown that electric fields are attenuated in the same characteristic distance λ_L, which is referred to as London penetration depth.

It is important to note that the London theory of superconductivity is a local theory. It assumes that the current density $\boldsymbol{J}_s(\boldsymbol{r})$ in a point $\boldsymbol{r}$ is determined entirely by the vector potential $\boldsymbol{A}(\boldsymbol{r})$ at the same position. Under the condition of long electronic mean free paths (in "clean superconductors") it is actually found that the experimental London penetration depth is larger than the one predicted above. This is because the assumptions of locality (that remain valid for "dirty superconductors") cease to hold. In this case, one has to average the potential $\boldsymbol{A}$ over a characteristic range ξ to obtain $\boldsymbol{J}_s$. The coherence length ξ is independent of λ_L, and was introduced in the Ginzburg-Landau theory of superconductivity (Tinkham, 1996; Kittel, 2005).

3.2 The Ginzburg-Landau Theory

A further milestone in the phenomenological description of macroscopic superconductivity was achieved with the development of the Ginzburg-Landau theory in 1950. Through the introduction of a complex pseudo-wavefunction as the order parameter in L. D. Landau's general theory of second order phase transitions, it became possible to treat the case when a magnetic field exceeds a critical value and depletes part of the superconductivity, causing a spacial dependence of the condensate density (Tinkham, 1996; Kittel, 2005). The most relevant aspect with respect to this thesis is the concept that the free energy of a superconductor depends not only on the order parameter, but also on its gradient. As such, the gradient of the pseudo-wavefunction is responsible for supercurrents in the material, and motivates the notion of a "phase stiffness". This concept highlights that the superconducting phase tends to be uniform throughout the specimen, strongly resisting perturbations (similar to the rigidity of a solid).

The Ginzburg-Landau description of superconductivity introduces a complex

wavefunction ψ, defining the local density of superconducting electrons as

$$n_s(\boldsymbol{r}) = |\psi(\boldsymbol{r})|^2 \quad . \tag{3.4}$$

The wavefunction ψ serves as an order parameter in the description, since it is zero in the normal state, and finite in the superconducting. In Landau's general description of second order phase transitions, one basic assumption is that the free energy can be described as a Taylor expansion in the order parameter ψ and its gradient $\nabla\psi$. The free energy represents the amount of work that a thermodynamic system is capable of performing. As such, the phenomenological expansion parameters α and β in the Taylor series are chosen to minimise the energy. Applied to superconductors, one arrives at the Ginzburg-Landau equations (Tinkham, 1996)

$$\frac{1}{2m}\left(\frac{\hbar}{2i}\nabla - \frac{e}{c}\boldsymbol{A}\right)^2 \psi + \beta(T)|\psi|^2\psi + \alpha(T)\psi = 0 \quad , \tag{3.5}$$

$$\frac{e\hbar}{2im}\left(\psi^*\nabla\psi - \psi\nabla\psi^*\right) - \frac{2e^2}{mc}|\psi|^2\boldsymbol{A} = \boldsymbol{J}_s \quad . \tag{3.6}$$

Equation (3.5) describes the order parameter in dependence of the magnetic vector potential $\boldsymbol{A}$ (note the similarity to the nonlinear Schrödinger equation for a free particle). The second Ginzburg-Landau equation (3.6) determines the superconducting current density $\boldsymbol{J}_s$ (compare to the probability current of a wave function). In combination, these equations allow for the description of a spatially varying superfluid density $|\psi(\boldsymbol{r})|^2$, and account for nonlinear effects should the vector potential exceed a critical value, leading to the coexistence of superconducting and normal domains. The corresponding critical magnetic field strength is in the following denoted H_c.

Besides encapsulating the effective penetration depth λ, which is given by

$$\lambda = \sqrt{\frac{mc^2}{4\pi|\psi|^2e^2}} \quad , \tag{3.7}$$

the Ginzburg-Landau description predicts the existence of a second characteristic

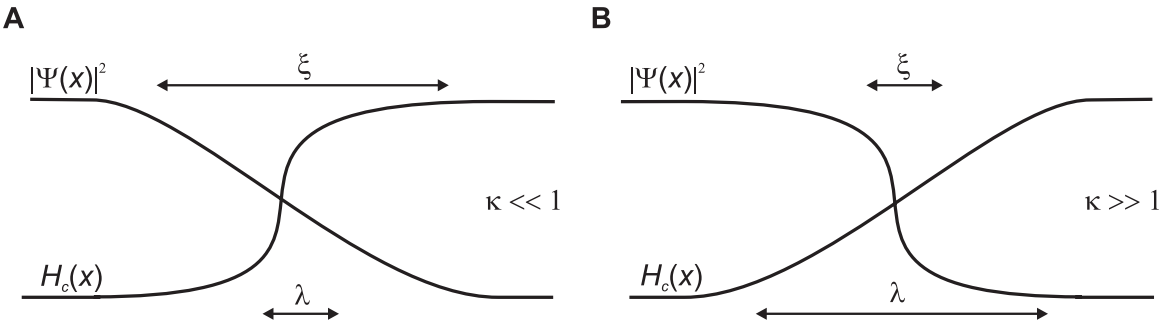


Figure 3.2: Interface between superconducting and normal domains. A: In a type 1 superconductor, the superfluid density changes over a much longer distance than the magnetic field, which is attenuated strongly in the superconducting domain. B: A type 2 superconductor does not show perfect diamagnetism because magnetic flux is allowed to penetrate much deeper into the bulk sample. Cuprates represent a prominent example of type 2 superconductors (Tinkham, 1996).

length scale, the coherence length, which is defined as

$$\xi = \frac{\hbar}{\sqrt{|2m\alpha|}} = \frac{\Phi_0}{2\sqrt{2}\pi H_c \lambda} \quad , \tag{3.8}$$

where $\Phi_0 = hc/(2e)$ is the flux quantum. Since there is an energy cost associated with a spatial variation of the density $n_s = |\psi|^2$, the coherence length ξ defines the distance within which the condensate density cannot change drastically without destroying the superconducting state.

The Ginzburg-Landau parameter κ is defined as the ratio of the two characteristic length scales $\kappa = \lambda/\xi$. In most conventional pure low-temperature superconductors called type 1 materials, the penetration depth is much smaller than the coherence length, and $\kappa \ll 1$. In this case, one is speaking of superconductivity in the clean limit, and the superconductive state is characterised by almost perfect diamagnetism.

For type 2 materials exhibiting $\kappa > 1/\sqrt{2}$ as found in many metal-based alloys and high-temperature superconductors, the superconductivity is local and in the dirty limit. An external magnetic field is not screened as efficiently as in type 1 superconductors and can penetrate into the sample. In the context of chapters 4 and 7 of this thesis, it is important to note that this property favours the injection of vortices into type 2 materials. The interface between a normal and superconducting domain is sketched in figure 3.2 comparing type 1 and 2 systems.

3.3 High-Frequency Electrodynamics

The London and Ginzburg-Landau theories describe the Meissner effect and perfect conductivity in the case of static external electromagnetic fields. If one considers the response of a superconductor to time-dependent fields, dissipation effects have to be taken into account. This is because time-dependent electromagnetic fields act not only on the superconducting, but also on the normal state electrons, which are not perfectly shorted. Scattering of the accelerated normal electrons from lattice imperfections gives rise to finite resistance, which can be captured by Ohm's law.

A fluid of free electrons subject to damping and a time-dependent electric field $E(t)$ while moving along the x-direction is described by the Newton equation

$$m\ddot{x} = -eE(t) - \frac{m}{\tau}\dot{x} \quad , \tag{3.9}$$

where m and e are electron mass and charge, and τ represents the relaxation time. The two fluid model asserts that the total electrons density n can be divided into a superfluid and a normal electron density n_s and n_n, respectively. Obviously, the restriction $n = n_n + n_s$ is imposed to conserve the total number of electrons. The behaviour of the superconducting and normal electrons is characterised by their relaxation times τ_s and τ_n, which are expected to differ as $\tau_s \gg \tau_n$. Assuming an external field of the form $E(t) = E_0 \exp(i\omega t)$, the a. c. response of the normal fraction of the electron density is captured by the complex conductivity (Tinkham, 1996)

$$\sigma_n(\omega) = \frac{n_n e^2 \tau_n / m}{1 + i\omega\tau_n} \quad . \tag{3.10}$$

Thus, the conductivity of the normal electrons follows the well-known Drude response of free electrons. The conductivity of the superfluid fraction is described by an equivalent expression and can be evaluated in the limit $\tau_s \to \infty$, giving rise to

$$\sigma_s(\omega) = \frac{n_s \pi e^2}{2m}\delta(\omega) + i\frac{n_s e^2}{m\omega} \quad . \tag{3.11}$$

The real part of the superfluid conductivity reduces to a delta function at zero frequency, reflecting vanishing d. c. resistivity. The imaginary part shows a $1/\omega$ frequency dependence, characteristic of the superconducting state and equivalent to the first London equation. In the *two fluid approximation*, the conductivity of a superconductor is then described by $\sigma(\omega) = \sigma_n(\omega) + \sigma_s(\omega)$.

It has to be noted that the two fluid model only applies to frequencies below the superconducting gap. Often, the normal electron relaxation times are short enough that $\omega\tau_n \ll 1$, in which case the total complex conductivity can be written as

$$\sigma(\omega) = \frac{n_s \pi e^2}{2m}\delta(\omega) + \frac{n_n e^2 \tau_n}{m} + i\frac{n_s e^2}{m\omega} \quad . \tag{3.12}$$

This limiting case illustrates that when probing a superconductor at finite frequencies, the real part of the conductivity reflects dissipation by normal state electrons. The imaginary part in contrast shows a $1/\omega$ frequency dependence, with a pre-factor that is determined by the superfluid density n_s. This characteristic is of great importance to the following chapters of this thesis, as the two fluid model is applied to interpret the experimental results.

3.4 The BCS Theory

The conjectures of Ginzburg and Landau were years later shown to be a limiting case of the first complete microscopic theory of superconductivity, which was developed in 1957 by J. Bardeen, L. N. Cooper and J. R. Schrieffer (BCS). One of the main findings of the BCS theory is the prediction that electrons close to the Fermi surface tend to form bound pairs in presence of any weak attractive interaction. These bound electrons with equal and opposite momentum and spin are called Cooper-pairs, and represent the superconducting charge carriers that were postulated by the phenomenological models introduced above (Bardeen *et al.*, 1957).

The BCS theory is founded on a quantum mechanical description of the inter-

action between the superconducting electrons. While single electrons are fermions, which have to obey the Pauli exclusion principle, Cooper-pairs behave like bosons that can condense into the same energetic state. Breaking a single Cooper-pair into its constituents therefore means that the state of all other unpaired electrons has to change. Hence, there is an energy gap associated with the excitation of a pair of single electrons (quasi-particles) out of the superconducting condensate (Kittel, 2005).

Figure 3.3 A shows the development of the gap for temperatures below the critical value. The width of the gap $E_g(T)$ is predicted to depend on the temperature and increases from zero at the transition temperature T_c to

$$E_g(0) \approx 3.5\, k_B T_c \quad , \tag{3.13}$$

as $T \rightarrow 0$. Here, k_B denotes the Boltzmann constant. Figure 3.3 B depicts how the gap energy changes as a function of temperature on a normalised scale. The emergence of the energy gap inhibits scattering processes that would lead to finite resistivity in the normal state. For low enough temperatures, such that the thermal energy is smaller than the superconducting gap, the condensed electrons can carry a current without resistivity, optimally shortening the normal state electrons.

Different mechanisms leading to the pairing of electrons are possible. In conventional low-temperature superconductors, the coupling of electrons to discrete lattice vibrations (phonons) produces a weak attractive force between the charge carriers, leading to the formation of Cooper-bound electrons. These boson-like particles are unaffected by the scattering processes impeding the motion of single electrons in metals, and give rise to vanishing resistivity. In an attempt to visualise the interaction, one can think of an electron pair moving through a crystal lattice of positively charged ions. Via the Coulomb interaction, the leading electron will attract the ions, leading to a local increase in positive charge, which in turn attracts the second electron. In combination, both electrons enter a bound state, and are capable of moving through the crystal structure without undergoing dissipative scattering processes.

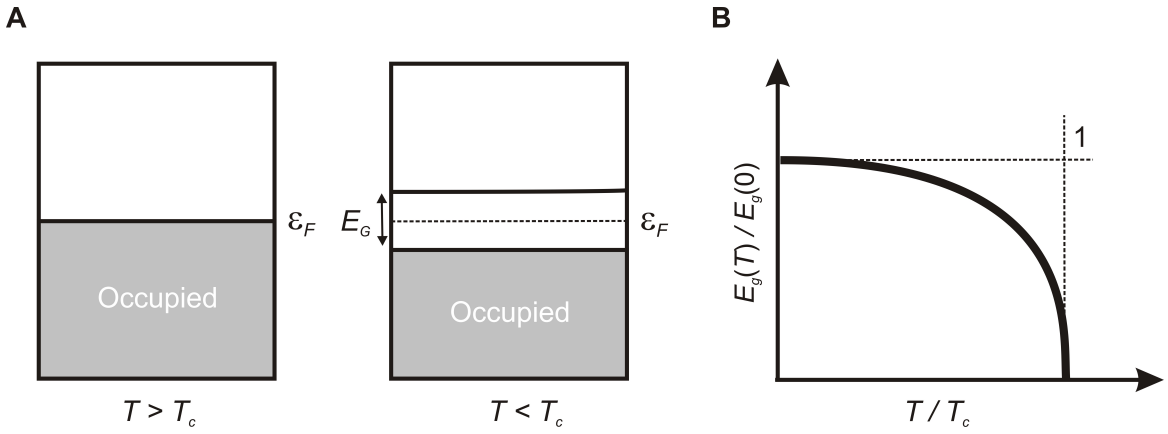


Figure 3.3: The superconducting energy gap. A: The left panel depicts the electronic state for temperatures above the transition temperature. The conduction band is occupied up to the Fermi level ϵ_F. The right panel shows the emergence of an energy gap at the Fermi level in the superconducting state. The energy gap has a size of E_g, which is exaggerated in the figure and usually much smaller than the Fermi energy. Breaking of a Cooper-pair amounts to an excitation of two electrons from the condensate above the gap. B: The relative size of the superconducting gap is shown schematically as a function of the reduced temperature. For $T \ll T_c$, the relative gap energy $E_g(T)/E_g(0)$ approaches unity. As the temperature increases to the critical temperature T_c, the gap decreases continuously to zero. The graphs are according to (Tinkham, 1996; Kittel, 2005).

According to the BCS theory, the spatial extension of a Cooper-pair is determined by the coherence length ξ. Because the coherence length in most conventional materials is much larger than the average distance between electrons, the wavefunctions of many pairs overlap, motivating the representation of the superconducting state by a single macroscopic many-body wavefunction that underpins the resulting Bose-Einstein statistics. The BCS theory predicted many of the fundamental properties of superconductors such as the isotope effect. This effect describes the experimental observation that if the mass of the lattice ions is increased, the transition temperature decreases. This is qualitatively understood by considering that an increase in mass will make the lattice less capable of meditating the interaction between two electrons.

In the context of this thesis, the microscopic BCS theory plays a minor part. Nevertheless, the concept of an energy gap due to pair binding is crucial, as the main objective of this work is to study below-gap excitations in superconductors. Despite its significance to low-temperature superconductivity, the BCS theory sets an upper limit for allowed transition temperatures of about 30 K. However, as discussed in the following section, materials exhibiting significantly higher critical temperatures exist.

3.5 High-Temperature Superconductivity

While the electron-phonon interaction is at the heart of the pair binding process in conventional superconductors such as mercury, it fails to account for high critical temperature (high-T_c) superconductivity, which was discovered in 1986 by G. Bednorz and K. A. Müller (Bednorz and Müller, 1986). High-T_c superconductors are commonly defined as materials whose transition temperature lies above 30 K, which is the highest allowed temperature that can be explained within the BCS framework. The first unconventional compounds were found to be quasi two-dimensional, with superconducting transport occurring within layers of weakly coupled copper oxygen planes. These ceramic oxides are referred to as cuprates.

In the decades after the discovery of the first high-T_c materials, further cuprates with increasingly higher critical temperatures of up to ~ 140 K were produced[†] (Dai *et al.*, 1995). The higher transition temperatures create an interest with respect to technical applications, since the superconducting state can be reached with liquid nitrogen as a coolant (boiling point 77 K), rather than with liquid helium. Liquid nitrogen is cheaper and considerably easier to produce than liquid helium.

In high-T_c cuprates, superconductive transport is carried by paired electrons as well (Gough *et al.*, 1987), but the origin of pair binding is still the subject of controversial debate (Lee *et al.*, 2006). The out-of-plane electrodynamics can be well-described by the Lawrence-Doniach model, which assumes that the copper oxygen layers are weakly coupled by the Josephson effect (Lawrence and Doniach, 1971). One of the key results is that the superconducting order parameter ψ can be described by

$$\frac{1}{2}\left(\frac{\hbar}{2i}\nabla - \frac{e}{c}\boldsymbol{A}\right)\left(\frac{1}{m}\right)\left(\frac{\hbar}{2i}\nabla - \frac{e}{c}\boldsymbol{A}\right)\psi + \beta|\psi|^2\psi + \psi = 0 \quad , \tag{3.14}$$

which corresponds to a Ginzburg-Landau equation with ellipsoidal anisotropy. The

[†]In 2008, a second class of high-T_c compounds was identified which consist of layers of iron and pnictogen (Takahashi *et al.*, 2008). These materials are called iron-pnictides. However, to keep the scope of this thesis, the following discussion focuses on cuprates.

reciprocal mass tensor $1/m$ has the principal values $1/m_{ab}$, $1/m_{ab}$, and $1/m_c$. The different masses represent the different strength of charge transport within the copper oxygen (*ab*-)planes, and in the perpendicular (*c*-)direction (see chapter 5 for further information). When the interlayer coupling is weak one has $m_c \gg m_{ab}$.

Using the definition of the isotropic coherence length in equation (3.8) above, it becomes clear that the coherence length ξ_j, and in turn the penetration depth λ_j, are anisotropic and given by

$$\xi_j(T) = \frac{\hbar}{\sqrt{|2m_j\alpha(T)|}} = \frac{\Phi_0}{2\sqrt{2}\pi H_c(T)\lambda_j(T)} \quad , \tag{3.15}$$

where j denotes the *ab*- or *c*-direction. Anisotropic cuprate superconductors usually have $\lambda_c \gg \lambda_{ab}$ and $\xi_c \ll \xi_{ab}$. The anisotropy of a layered superconductor is encapsulated in the ratio $\gamma = \lambda_c/\lambda_{ab} = \xi_{ab}/\xi_c$.

Apart from the higher transition temperature and the structural anisotropy, high-temperature compounds differ from conventional materials in that the superconducting state is more affected by resistance-causing fluctuations. This is because higher temperatures inevitably lead to stronger thermal fluctuations and because the materials are type 2 superconductors with comparably short coherence lengths. External magnetic fields penetrate into the materials and give rise to the formation of vortices. In a vortex, a supercurrent flows around a normal or superconducting core, carrying one unit of magnetic flux (Moler *et al.*, 1998; Tinkham, 1996). Vortex excitations in cuprates are discussed in greater detail in chapter 7 of this thesis.

In most cuprates, the Josephson coupling energy as well as the gap are of the order of several millielectronvolts, corresponding to terahertz frequencies. Thus, terahertz spectroscopy provides a convenient tool to investigate and control the superconducting state. The approach taken in this thesis is to focus on the Josephson-aspect of cuprate superconductors, and to exploit this property for nonlinear spectroscopy. The fundamental Josephson physics of layered superconductors are introduced in the next chapter, which is followed by a discussion of the cuprate $La_{x-2}Sr_xCuO_4$.

Chapter 4

The Josephson Effect

One of the defining features of quantum mechanics is the assertion that quantum objects can tunnel through a potential barrier that represents an unsurmountable obstacle for classical particles. Single free electrons possess this quality and can tunnel from one conductor to another via a thin insulating barrier. In an external potential, the tunnelling current depends exponentially on the work function of the material and the gap spacing, enabling the exploitation of the effect for imaging techniques in scanning tunnelling microscopy (Binning *et al.*, 1982).

The phenomenon of electric tunnelling between two superconductors that are separated by a thin insulating barrier is named after its discoverer B. D. Josephson. In 1962, Josephson predicted that a zero voltage d. c. supercurrent would flow across the barrier between two unbiased electrodes, with an amplitude determined by the superconducting order parameter phase difference across the link. He derived an expression for the temporal evolution of the relative phase in case a voltage difference were established across the junction. Maintaining a constant voltage leads to an alternating current with a frequency proportional to the electric potential difference.

These fascinating predictions, known as the d. c. and a. c. Josephson effect, have hitherto been confirmed in a plethora of experiments. However, Josephson physics has given rise to many more phenomena. Analogous to coupling between classical mechanical oscillators, stacks of interacting Josephson junctions give rise to complex

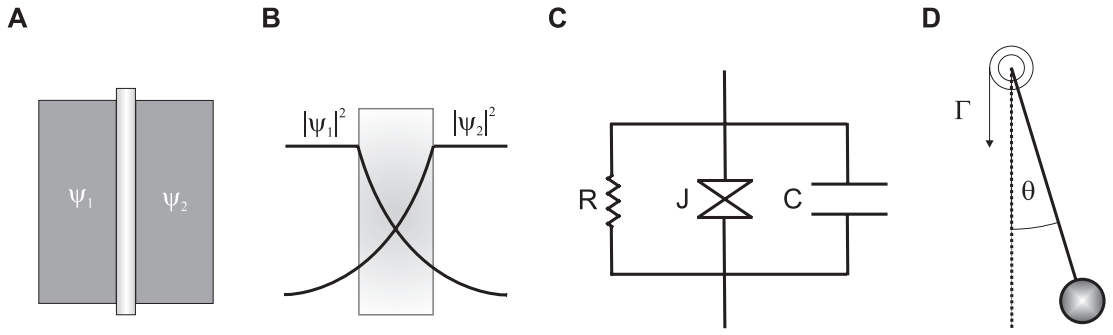


Figure 4.1: The Josephson effect. A: Two superconductors are separated by an insulating barrier. The condensate in both electrodes is described in terms of the complex wavefunction ψ_1 and ψ_2, respectively. B: If the insulating layer is thin enough, there is a finite probability for electrons from either side to tunnel through the barrier. C: The RCSJ model describes a real Josephson link as an ideal junction J, that is shunted by a resistance R representing quasiparticle transport. The junction geometry is encapsulated by the capacitance C. D: Mechanical analogue of the Josephson effect. The angle of deviation θ corresponds to the phase difference, the angular velocity $\dot{\theta}$ to the voltage, and the torque Γ to the current. The pendulum tips over if a critical torque is applied, leading to a finite angular velocity. Small amplitude oscillations correspond to the Josephson resonance.

dynamical behaviour. Stacked junctions can be realised based on niobium technology (Ustinov *et al.*, 1993), however, it has turned out that anisotropic layered superconductors such as cuprates provide stacks of great homogeneity and density. In these materials, the superconducting layers are formed by single CuO_2 sheets, with inductive coupling between layers giving rise to plasmonic behaviour (Machida *et al.*, 1999).

The present chapter is organised as follows. First, the fundamental physics of Josephson coupling is introduced. Second, the electrodynamics of long Josephson junctions are outlined. Finally, stacks of junctions are discussed.

4.1 Fundamental Josephson Physics

The consequences of Cooper-pair tunnelling between two superconductors were first noticed by Josephson (Josephson, 1962). In his microscopic analysis, Josephson considered two superconductors connected by a thin insulating layer as depicted in figure 4.1 A. This basic structure is now called a Josephson junction. If the insulating barrier is too thick, electron pairs are not able to tunnel from one electrode to the other. However, if the layer is thin enough, there is a finite quantum mechanical tunnelling amplitude across the barrier as depicted in figure 4.1 B.

The main phenomena that result from the Josephson tunnelling mechanism can be understood by considering two coupled Schrödinger equations for the wavefunctions on both sides of the barrier (Feynman *et al.*, 1966). One essential characteristic of the superconducting state is the existence of a many-particle condensate wave function ψ maintaining phase coherence over a macroscopic distance. In the following, the amplitude to find an electron on the left side of the barrier is called ψ_1, the amplitude to find it on the other side ψ_2. Assuming the same superconducting material on both sides of the junctions, the two amplitudes are related by

$$\begin{aligned} i\hbar\dot{\psi}_1 &= U_1\psi_1 + K\psi_2 \quad , \\ i\hbar\dot{\psi}_2 &= U_2\psi_2 + K\psi_1 \quad , \end{aligned} \tag{4.1}$$

where K is a characteristic coupling constant. Without coupling ($K = 0$), the two equations simply describe the lowest energetic states with energies U_1 and U_2, respectively. Finite coupling ($K > 0$) describes leaking of the wavefunctions across the barrier into the other electrode. This set of equations can be analysed by choosing a solution of the form

$$\begin{aligned} \psi_1 &= \sqrt{\rho_1}e^{i\phi_1} \quad , \\ \psi_2 &= \sqrt{\rho_2}e^{i\phi_2} \quad , \end{aligned} \tag{4.2}$$

where ϕ_1 and ϕ_2 are the phases of the condensate wavefunctions on both sides of the junction, and ρ_1 and ρ_2 are the corresponding Cooper-pair densities. Substituting this expression into equations (4.1) and comparing real and imaginary parts gives rise to

$$\begin{aligned} \hbar\dot{\rho}_1 = -\hbar\dot{\rho}_2 &= 2K\sqrt{\rho_1\rho_2}\sin(\phi_2 - \phi_1) \quad , \\ \hbar(\dot{\phi}_2 - \dot{\phi}_1) &= U_1 - U_2 \quad . \end{aligned} \tag{4.3}$$

The time derivative of the Cooper-pair density effectively describes a current $I = \dot{\rho}_1$. If the two superconducting regions are connected to a battery so that a potential difference V is applied across the junction, $U_1 - U_2 = 2eV$, with $2e$ being the charge

of an electron pair. Defining the zero energy appropriately and introducing the phase difference $\phi \equiv \phi_1 - \phi_2$, equations (4.3) can thus be written as[†]

$$I = I_c \sin\phi \quad , \tag{4.4}$$

$$\dot{\phi} = 2eV/\hbar \quad . \tag{4.5}$$

Here, $I_c = 2K\sqrt{\rho_1\rho_2}/\hbar$ is the critical current. Equations (4.4)-(4.5) are commonly referred to as the first and second Josephson equation, and represent the general theory of a weak link between two superconductors. If there is no voltage drop across the junction, the d. c. supercurrent can take any value between $-I_c$ and I_c. The critical current therefore denotes the maximum supercurrent that the junction can support. In contrast, if a constant voltage is maintained across the junction, the phase difference advances linearly in time ($\phi \propto t$). This in turn leads to a sinusoidally oscillating supercurrent at a frequency of $f_{ac} = 2eV/h$, whereby the net current remains zero. These two phenomena are known as the d. c. and a. c. Josephson effect, respectively.

One way of interpreting the zero voltage d. c. Josephson effect is given in terms of a nonlinear inductance (Josephson, 1964). If one considers a small deviation of the phase difference δ (small enough to preserve the zero voltage state) from its equilibrium position ϕ_0, the first Josephson equation (4.4) implies a current change

$$\Delta I = (I_c \cos\phi_0)\delta \quad . \tag{4.6}$$

Through the second Josephson equation, the phase variation induces a voltage as

$$\Delta V = \hbar/(2eI_c \cos\phi_0)(\dot{\Delta I}) = L(\dot{\Delta I}) \quad . \tag{4.7}$$

This expression is the defining equation for an inductor with a nonlinear inductance

[†]Assuming that the barrier thickness in negligible. In general, the phase difference ϕ is, unlike the supercurrent I, not a well-defined gauge-invariant physical quantity. This is corrected by introducing the gauge-invariant phase difference $\phi = \phi_1 - \phi_2 - \frac{2e}{\hbar c}\int_2^1 \boldsymbol{A}\cdot\boldsymbol{ds}$, $\boldsymbol{A}$ being the magnetic vector potential.

$L = \hbar/(2eI_c \cos\phi_0)$. The Josephson inductance therefore depends on the equilibrium phase difference ϕ_0, which can be adjusted by an external electric current or field. Without external stimulus, the inductance takes the minimum value $L_0 = \hbar/(2eI_c)$. It should be noted that the Josephson inductance is a kinetic inductance, since it arises from the kinetic energy of the Cooper-pairs rather than the magnetic field energy.

Josephson's equations are often sufficient to describe the zero voltage characteristics, however, they do not model dissipation effects in the finite voltage regime. One approach to combine the a. c. Josephson physics with quasiparticle dissipation is the Resistively and Capacitively Shunted Junction (RCSJ) model. As depicted in figure 4.1 C, a real Josephson junction is modelled by an ideal weak link J shunted in parallel by a voltage independent resistance R and a capacitance C. An external current source provides a bias current I. The resistance accounts for dissipation in case the total current I exceeds the critical current I_c, and quasiparticles flow across the junction. Due to the junction geometry, a parallel capacitor is added to model charging effects. The total current through the link equals the sum of the contributions from each parallel element according to the differential equation

$$I = I_c \sin\phi + V/R + C\dot{V} \quad . \tag{4.8}$$

Using Josephson's equations and introducing a dimensionless time variable $t \rightarrow \omega_J t$, this expression can be rewritten to form a second-order differential equation in the phase difference reading

$$\ddot{\phi} + \beta_c \dot{\phi} + \sin\phi = I/I_c \quad , \tag{4.9}$$

with the parameter $\beta_c = \omega_J RC$ determining the damping (McCumber, 1968). The characteristic frequency is defined as $\omega_J = \sqrt{2eI_c/(\hbar C)} = 1/\sqrt{L_0 C}$, and corresponds to the resonance frequency of the undamped oscillator circuit in the limiting case of small amplitudes when $\sin\phi \approx \phi$. These plane wave solutions are a type of plasma

oscillations, whereas the electric current and field are oriented normal to the barrier. The oscillatory behaviour can be understood in terms of an exchange between the inductive and capacitive energy terms.

It is interesting to note that equation (4.9) has a mechanical analogue, which describes a physical pendulum attached to a pulley as illustrated in figure 4.1 D. The superconducting phase difference is thereby replaced by the angle θ of the pendulum with respect to the vertical direction, while the applied torque Γ replaces the external current. The average angular velocity of the mechanical pendulum corresponds to the voltage across a weak link. By introducing the dimensionless time coordinate $t \rightarrow \omega_R t$, the equation of motion for the pendulum reads (Altshuler and García, 2002)

$$\ddot{\theta} + \nu\,\dot{\theta} + \sin\theta = \Gamma/\Gamma_c \quad , \tag{4.10}$$

where ω_R is the resonance frequency of the linearised problem, and ν determines the damping. The parameter Γ_c denotes the critical value of the torque, that lets the pendulum tip over its pivot.

With the help of the pendulum analogue, one can obtain qualitative insight into the different types of Josephson junction dynamics. As the external torque Γ increases from zero, the deflection angle of the pendulum increases, achieving an equilibrium position θ_0 for a given torque. The angular velocity of the pendulum is zero in this case. Hence, the behaviour is analogous to the d. c. Josephson effect when the interlayer phase difference is finite and a constant supercurrent flows ($I < I_c$, $\phi = \phi_0$, $V = 0$). If the torque is increased above it's critical value Γ_c when the pendulum is aligned horizontally ($\theta = \pi/2$), the system starts to swing and the angle θ increases in time with an average angular velocity determined by the torque. This is analogous to the oscillating supercurrents of the a. c. Josephson effect ($I > I_c$, $\phi \propto t$, $V \neq 0$). The resonance frequency ω_R of the pendulum in the approximation $\sin\theta \approx \theta$ corresponds to small amplitude oscillations around the equilibrium position $\theta_0 = 0$. This mechanical resonance is the analogue of Josephson plasma waves.

4.2 Electrodynamics of Long Josephson Junctions

The electrodynamics of long two-dimensional Josephson junctions can be understood by considering Maxwell's equations, relating the magnetic field $\boldsymbol{B}$ to the electric current $\boldsymbol{J}$ and electric field $\boldsymbol{E}$ as

$$\nabla \times \boldsymbol{B} = \frac{4\pi}{c}\boldsymbol{J} + \frac{\epsilon_r}{c}\frac{\partial \boldsymbol{E}}{\partial t} \quad , \tag{4.11}$$

where c is the speed of light, and ϵ_r the relative dielectric constant of the barrier material. The junction is supposed to lie in the plane $z = 0$, having a separation s (see figure 4.2 A). The magnetic field is assumed to have nonzero x- and y-components, while the electric field is parallel to the z-axis (with $\hat{\boldsymbol{z}}$ being the unit vector along the same direction). Then, the phase difference across the junction obeys

$$\nabla\phi = \frac{2\pi(2\lambda + s)}{\Phi_0}\boldsymbol{B} \times \hat{\boldsymbol{z}} \quad , \tag{4.12}$$

where $\Phi_0 = hc/2e$ is the flux quantum, and λ the London penetration depth. The z-component of the total current J_z is composed of two contributions stemming from superconducting and quasiparticle tunnelling as

$$J_z = J_c \sin\phi + \sigma V/s \quad . \tag{4.13}$$

Here, σ is the quasiparticle conductivity. Combining the expressions (4.11)-(4.13) and introducing the Josephson penetration depth as $\lambda_J = \sqrt{c\,\Phi_0/[8\pi^2 J_c(s + 2\lambda)]}$ gives rise to the sine-Gordon equation for the relative phase (Josephson, 1965; Hu and Lin, 2010)

$$\frac{\partial^2\phi}{\partial x^2} + \frac{\partial^2\phi}{\partial y^2} - \frac{1}{c'^2}\frac{\partial^2\phi}{\partial t^2} - \frac{\beta'}{c'^2}\frac{\partial\phi}{\partial t} = \frac{1}{\lambda_J^2}\sin\phi \quad , \tag{4.14}$$

with the Swihart velocity $c' = c/\sqrt{\epsilon_r(1 + 2\lambda/s)}$, and the damping coefficient reading $\beta' = 4\pi\sigma/\epsilon_r$. In the stationary limit of small phases ϕ and if dissipation is neglected,

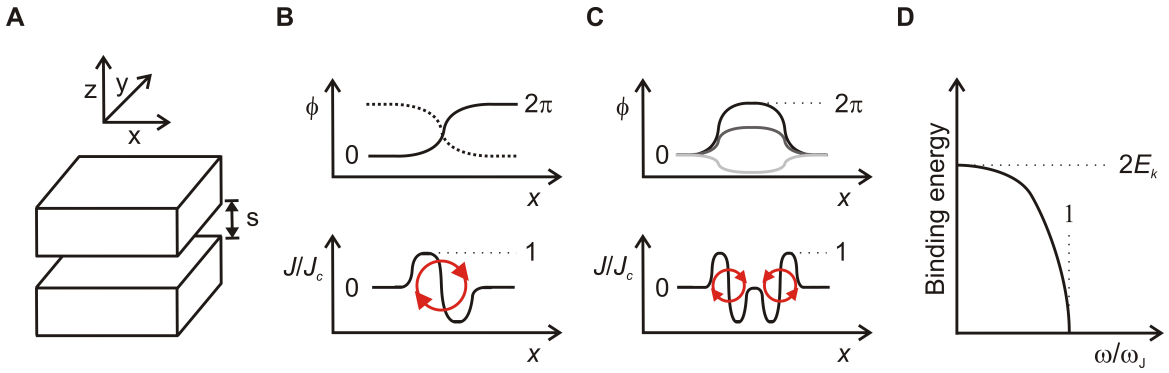


Figure 4.2: Nonlinear modes of long Josephson junctions. A: Schematic of a long Josephson junction with spatial separation s. B: The upper panel depicts a kink (solid line) and antikink (dotted line), corresponding to a 2π phase twist of the interlayer phase difference ϕ along the x-direction (the phase is assumed to be uniform along the y-axis). The lower panel shows $\sin\phi$ of the kink, which is equal to the normalised supercurrent distribution J/J_c. As can be seen from the resulting loop of circulating current (red curve), a kink corresponds to a Josephson vortex oriented perpendicular to the junction, with a vortex core confined in-between the electrodes. C: The upper panel shows a breather for three different points in time. A breather is a bound-state kink-antikink pair, which oscillates around a common centre of mass position. Large amplitude breathers correspond to vortex-antivortex pairs (the red curves indicate the resulting currents). D: Binding energy of breathers versus relative frequency. The binding energy converges to twice the rest energy of a single vortex E_k at low frequencies, while approaching zero close to the Josephson plasma frequency (Eilbeck *et al.*, 1981).

equation (4.14) has the character of a London-type penetration equation $\nabla^2\phi = \lambda_J^{-2}\phi$. This means that the Josephson current is confined in a distance of λ_J from the edges of the electrodes due to screening by the self-generated magnetic field.

Equation (4.14) describes the full electrodynamics of the long Josephson junction. It represents a nonlinear partial differential equation and a general solution has not been found yet. However, some special cases can be treated analytically.

In the limit of small amplitudes ($\sin\phi \approx \phi$) and negligible damping, the system can show collective oscillations of Cooper-pairs between the two electrodes at the Josephson plasma frequency $\omega_J = c'/\lambda_J$. The electric field is oriented along the z-direction and the mode corresponds to a longitudinal plasma wave. Contrary, solutions of the form $\phi(x,y,t) = \phi_0\exp\{i(\boldsymbol{k}\cdot\boldsymbol{r} - \omega t)\}$ give rise to transverse plasma wave solutions with the dispersion relation $\omega^2 = \omega_J^2 + c'^2k^2$. Thus, c' defines the minimum phase and maximum group velocity of linear electromagnetic waves in long Josephson junctions.

In the extremely nonlinear regime, equation (4.14) gives rise to soliton solutions (Martinov and Vitanov, 1992). For the sake of presentability, it is convenient to consider solutions depending on the spatial coordinate x only, while the phase is

assumed to be uniform along the y-axis. For the full two-dimensional solution, giving rise to well-defined vortices that are localised in the xy-plane, please consult (Martinov and Vitanov, 1992). The one-dimensional form, however, captures the basic physics of the Josephson vortex as discussed in chapter 7 of this thesis, owing to the system's isotropy within the xy-plane. Introducing the coordinates $x \to x/\lambda_J$, and $t \to \omega_J t$, the fundamental nonlinear modes can be categorised in two classes, (i) kink or antikink, and (ii) breather solutions (Eilbeck *et al.*, 1981)

$$(i) \quad \phi(x,t) = 4\tan^{-1}\left[\exp\{\pm\gamma(x - x_0 - ut)\}\right] \quad , \tag{4.15}$$

$$(ii) \quad \phi(x,t) = 4\tan^{-1}\left[\sqrt{1/\omega_b^2 - 1}\sin\theta_I \operatorname{sech}\theta_R\right] \quad . \tag{4.16}$$

Here, $\theta_I = \gamma\omega_b\left[t - u(x - x_0)\right]$, $\theta_R = \gamma\sqrt{1-\omega_b}(x - x_0 - ut)$, and $\gamma = 1/\sqrt{1-u^2}$. The (dimensionless) velocity u can take the values $0 < u < 1$, corresponding to $0 < u < c'$ in real units. The Swihart velocity thus defines the maximum speed of propagation.

The first solution (i) is called kink or antikink, depending on the sign of the argument in the exponent. As shown in figure 4.2 B, the kink or antikink represents a twist of the phase between the zero energy constant solutions $\phi = 0$ and $\phi = 2\pi$, or vice versa. The resulting current distribution of the kink (antikink) illustrates that these solutions correspond to vortex (antivortex) states in the junction, with supercurrents circulating around the superconducting vortex core. Because $\int_{-\infty}^{\infty} \frac{\partial\phi}{\partial x} dx = 2\pi$, solitons carry one quantum of magnetic flux, which is why they are also called *fluxons*. The energy carried by a fluxon is $E_k = 8\gamma$, determined by the velocity.

The breather solution (ii), displayed in figure 4.2 C, can be viewed as a bound state kink-antikink pair oscillating with the (dimensionless) frequency ω_b. Thereby, the oscillation frequency ω_b represents a parameter which can be freely chosen within the interval $0 < \omega_b \leq 1$. In real units this means for the frequency $0 < \omega_b \leq \omega_J$. Hence, a small amplitude breather is oscillating with the Josephson plasma frequency ω_J. Figure 4.2 D depicts the binding energy, which is given by $E_b = 2E_k\sqrt{1-\omega_b^2}$. The binding energy goes to zero as $\omega_b \to 1$, and the breather can be considered as a

coherent spatially confined excitation of linear plasmons. Transforming back into real time units, this means that the binding energy vanishes as the frequency gets close to the Josephson plasma frequency ω_J. For $\omega_b \to 0$, the breather energy $E_b = 2E_k$ approaches twice the energy of a single kink (antikink). Contrary to vortex solutions, there is no threshold energy required for the creation of breathers, and a relatively small inhomogeneous driving force is expected to excite a low energy breather mode (Eilbeck *et al.*, 1981).

4.3 Stacks of Josephson Junctions

When stacks of Josephson junctions are formed by connecting a number of long laterally extended weak links (of dimension larger than the Josephson penetration depth λ_J) in series, inter-junction coupling leads to intriguing collective phenomena. As described in chapter 5 of this thesis, layered cuprate superconductors represent stacks of intrinsic Josephson junctions. The linear Josephson properties of cuprates have been examined in a variety of experiments, including current-voltage (Kleiner *et al.*, 2000) and terahertz spectroscopy measurements (Tamasaku *et al.*, 1992; Thorsmølle *et al.*, 2001). The latter becomes possible since external terahertz fields couple resonantly to the Josephson plasma waves in cuprates. In the present thesis, the nonlinear regime of plasma excitations is exploited using high-field terahertz radiation.

In the following, a stack of Josephson junctions is theoretically investigated according to figure 4.3 A, with the superconducting electrodes parallel to the xy-plane, being separated by the distance s. A weak electric field is assumed to be parallel to the z-axis, whereas the magnetic field is parallel to the xy-plane. The Josephson coupling between planes can be analysed on the basis of the Lawrence-Doniach model (see section 3.5), which relates the superconducting phase difference in the lth layer to the current $\boldsymbol{J}_l$ and the magnetic field $\boldsymbol{B}_l$ as (Lawrence and Doniach, 1971)

$$\nabla_{xy}\phi_l = \frac{8\pi^2\lambda_{ab}^2}{c\Phi_0}(\boldsymbol{J}_{l+1} - \boldsymbol{J}_l) + \frac{2\pi s}{\Phi_0}\boldsymbol{B}_l \times \hat{\boldsymbol{z}} \quad . \tag{4.17}$$

Here, the del operator $\nabla_{xy} = (\frac{\partial}{\partial x}, \frac{\partial}{\partial y}, 0)$ is acting in the lateral xy-direction. Neglecting charging effects of the layers, the current conservation dictates (Hu and Lin, 2010)

$$\nabla_{xy} \cdot (\boldsymbol{J}_{l+1} - \boldsymbol{J}_l) = -\frac{1}{s}\Delta_d J_l^z \quad , \tag{4.18}$$

with J_l^z being the current across the lth junction. Δ_d represents a difference operator acting along the z-direction and is defined as $\Delta_d J_l^z = J_{l+1}^z + J_{l-1}^z - 2J_l^z$. Using the Maxwell relations $\nabla \cdot \boldsymbol{E} = 4\pi\rho/\epsilon_r$ and equation (4.11), expression (4.17) can be written in the form

$$\nabla_{xy}^2 \phi_l = \left(1 - \frac{\lambda_{ab}^2}{s^2}\Delta_d\right)\left(\frac{8\pi^2 s}{\Phi_0 c}\frac{\partial J_l^z}{\partial t} + \frac{2\pi s \epsilon_r}{\Phi_0 c}\frac{\partial E_l^z}{\partial t}\right) \quad . \tag{4.19}$$

Substituting J_l^z by the Josephson current relation (4.13) with $J_c = c\Phi_0/(8\pi^2\lambda_c^2 s)$, and using the a. c. Josephson equation (4.5), the phase evolution is governed by

$$\lambda_c^2 \nabla_{xy}^2 \phi_l = \left(1 - \frac{\lambda_{ab}^2}{s^2}\Delta_d\right)\left(\sin\phi_l + \frac{4\pi\sigma\lambda_c^2}{c^2}\frac{\partial \phi_l}{\partial t} + \frac{\lambda_c^2 \epsilon_r}{c^2}\frac{\partial \phi_l^2}{\partial t^2}\right) \quad . \tag{4.20}$$

By introducing the dimensionless variables $x \to x/\lambda_c$, $y \to y/\lambda_c$, and $t \to \omega_J t$, this expression can be equivalently written as

$$\nabla_{xy}^2 \phi_l = \left(1 - \varkappa\Delta_d\right)\left(\sin\phi_l + \beta\frac{\partial \phi_l}{\partial t} + \frac{\partial \phi_l^2}{\partial t^2}\right) \quad , \tag{4.21}$$

where $\varkappa = (\lambda_{ab}/s)^2$ is the constant of inductive coupling, the dimensionless damping parameter is given by $\beta = 4\pi\sigma/(\omega_J \epsilon_r)$, and the Josephson plasma frequency reads $\omega_J = c/(\lambda_c\sqrt{\epsilon_r})$. For phase differences uniform along the z-axis, this expression is equivalent to equation (4.14) for a single junction.

In analogy to a single weak link, small amplitude Josephson plasma wave solutions exist. The dispersion relation for a purely transverse plasma wave travelling along the x-direction reads $\omega^2 = \omega_J^2 + c'^2 k_x^2$, where $c' = c/\sqrt{\epsilon_r}$ is the light velocity in the material. Thus, the dispersion is qualitatively identical to the relation for the transverse mode

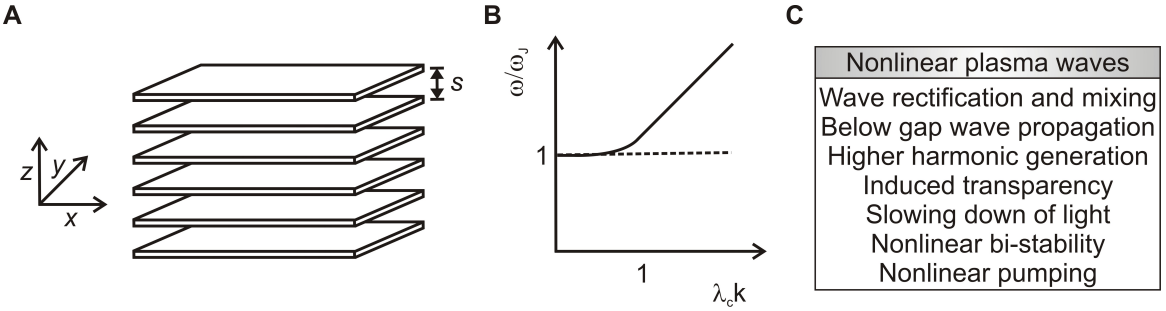


Figure 4.3: Physics of stacks of Josephson junctions. A: Schematic of a stack of Josephson junctions separated by the distance s. B: Dispersion relation of small amplitude transverse (solid line) and longitudinal (dashed line) Josephson plasma waves propagating in a stack of junctions. C: Summary of novel effects predicted in reference (Savel'ev *et al.*, 2006) for nonlinear Josephson plasma waves in layered superconductors under the approximation $\sin\phi \approx \phi - \phi^3/6$ in equation (4.22).

in a single junction, differing only in the temporal and spatial constants involved.

For nonuniform phase differences along the z-direction, the dispersion of the longitudinal plasma waves can be determined by incorporating charging effects of the superconducting electrodes (Hu and Lin, 2010). With the Debye length μ, defining the distance over which mobile charge carriers screen out an electric field, the longitudinal plasma dispersion reads $\omega^2 = \omega_J^2 + c^2\mu^2 k_z^2/\lambda_c^2$. In the limit of small charging effects when $\mu \to 0$, this expression reduces to the constant relation obtained for the single junction. Since $\mu \ll \lambda_c$ for the intrinsic stacks of junctions under investigation in this thesis, the dispersion is much smaller than for the transverse wave as depicted in figure 4.3 B.

In the limit of long wavelengths compared to the interlayer spacing, the difference operator in equation (4.21) can be treated in the continuum approximation, yielding the sine-Gordon equation (Savel'ev *et al.*, 2006)

$$\nabla_{xy}^2\phi = \left(1 - \frac{\partial^2}{\partial z^2}\right)\left(\sin\phi + \beta\frac{\partial\phi}{\partial t} + \frac{\partial\phi^2}{\partial t^2}\right) \quad . \tag{4.22}$$

Linear small amplitude longitudinal and transverse plasma waves which can be described with this equation have been observed experimentally in a number of Josephson junctions (Tamasaku *et al.*, 1992; Kadowaki *et al.*, 1997; Thorsmølle *et al.*, 2001). Furthermore, the nonlinear regime has been explored in experiments and theory. The

evolution equation (4.21) has been applied for instance to understand vortex dynamics in Josephson systems (Kleiner *et al.*, 2000; Hu and Lin, 2010).

Some recent theoretical investigations have predicted a range of intriguing nonlinear phenomena in the intermediate weakly nonlinear regime when $\sin\phi \approx \phi - \phi^3/6$ (Savel'ev *et al.*, 2006). Analogous to conventional nonlinear optics, nonlinear Josephson plasma waves are predicted to give rise to effects such as higher harmonic generation at terahertz frequencies, slowing down of electromagnetic radiation, nonlinear pumping of weak waves, and electromagnetically induced transparency below the plasma frequency (see the summary in figure 4.3 C). Cuprate superconductors, which represent stacks of intrinsic Josephson junctions as outlined in the next chapter, are expected to give rise to these nonlinear phenomena when subject to sufficiently strong terahertz fields.

Chapter 5

The Cuprate $La_{2-x}Sr_xCuO_4$

High critical temperature (T_c) cuprate superconductors are generally considered to be quasi two-dimensional systems in which mobile charge carriers primarily reside within weakly coupled copper oxygen (CuO_2) planes. The superconducting layers are separated by neighbouring dielectric planes that contain atoms such as lanthanum, strontium or barium. These atoms act as charge reservoirs that control the doping of the CuO_2 planes with free carriers and represent spacers delivering stability and determining the level of anisotropy. The un-doped parent compounds of cuprate superconductors have insulating character, accompanied by antiferromagnetic ordering at low temperatures. The phase diagram in figure 5.1 A highlights qualitatively the emergence of superconductivity in dependence of temperature for hole-doped cuprates.

Cuprates can be categorised according to the constituent elements and the number of CuO_2 layers building the superconducting blocks. Substitution of divalent Sr for trivalent La in the antiferromagnetic insulator La_2CuO_4 introduces mobile holes into the copper-oxygen layers and leads to superconductivity in $La_{2-x}Sr_xCuO_4$. Here, the doping level is expressed in terms of the fractional number x. $La_{2-x}Sr_xCuO_4$ represents a prototype high critical temperature superconductor, adopting the perovskite-like crystal structure depicted in figure 5.1 B with one CuO_2 plane per unit cell. The copper oxygen planes resemble checkerboards with a Cu^{2+} ions at the centres of squares whose corners are taken by O^{2-} ions. Oxygen ions surround the copper ions

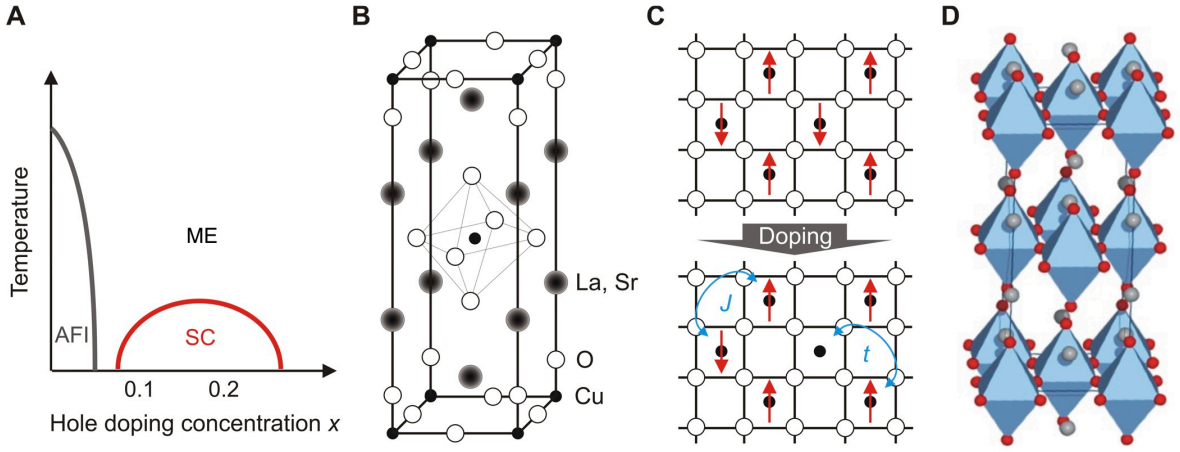


Figure 5.1: Microscopic properties of the cuprate $La_{2-x}Sr_xCuO_4$. A: Simplified phase diagram of hole-doped cuprate superconductors. The parent compound represents an antiferromagnetic insulator (AFI). Doping of holes leads to the emergence of metallic transport (ME). At low temperatures, a superconducting (SC) dome develops. B: The unit cell of $La_{2-x}Sr_xCuO_4$, highlighting the perovskite crystal structure. Copper atoms are at the corners of the unit cell, which contains a single superconducting copper oxygen layer (Lee, 2008). C: The superconducting planes resemble a checkerboard pattern with copper atoms located at the centre of squares defined by four oxygen atoms. The parent compound is an insulator due to the repulsive Coulomb interaction of the electrons. The ferromagnetic exchange interaction J permits a finite hopping amplitude t. As holes are introduced into the planes by doping, the charge carriers become mobile and metallic conductivity develops (Lee *et al.*, 2006). D: The copper oxygen octahedra form stacks of CuO_2 layers lying in the *ab*-plane. The CuO_2 planes have a separation of ~ 6.6 Å (Kubo *et al.*, 2009). Charge dynamics along the perpendicular *c*-axis can be understood by invoking Josephson coupling between the planes.

to form octahedral cages, separated from each other by sheets containing lanthanum and strontium ions. The unit cell is rotated by 45° from the checkerboard pattern, where the centre and corners are taken by the copper ions (Lee *et al.*, 2006; Lee, 2008).

The electronic properties of the copper oxygen layers are determined by the doping level, and the parent compounds of cuprate superconductors are typically Mott insulators. In a copper oxygen layer of La_2CuO_4, which is schematically depicted in the upper panel of figure 5.1 C, each copper atom has one loosely bound electron that in principle has the potential to move from one copper atom to another carrying an electrical current. However, because of the repelling Coulomb interaction of electrons at adjacent lattice sites, the system has an insulating character. In addition, the undoped material gives rise to antiferromagnetism, a state of spin order without bulk magnetisation. The forces between the electrons' magnetic moments lead to neighbouring spins pointing in opposite directions, such that an alternating spin-orientation pattern develops across the material. The spin-ordered state, which arises due to the

antiferromagnetic exchange interaction J, diminishes the virtual hopping amplitude t between the lattice sites (Lee, 2008).

When lanthanum atoms are replaced by strontium and the doping level rises from zero ($x > 0$) as depicted in the lower panel of figure 5.1 C, the material turns from an insulator to a conductor. This is because the electron affine strontium atoms attract the loosely bound electrons from the copper atoms. The introduction of electron vacancies leads to greater charge mobility as the Coulomb repulsion declines locally (see figure 5.1 A). At even larger doping values, the material becomes superconducting when the temperature is reduced below the critical value T_c. Optimal doping is defined as the level at which T_c reaches its maximum value, accounting for $x \approx 0.2$ in many copper oxides. In the superconducting phase, carriers move freely within the copper oxygen planes (ab-axis), while the out-of-plane (c-axis) electrodynamics are dominated by quantum tunnelling between the CuO_2 layers (Lee, 2009).

More than 25 years after their discovery, possible mechanisms for pair-binding in high-temperature superconductors are still the subject of considerable debate (Lee, 2008). However, tunnelling between planes makes possible three-dimensional coherent transport in cuprates, and the c-axis electrodynamics can be understood by considering stacks of intrinsic Josephson junctions (see figure 5.1 D).

The Josephson coupling, however, also depends on the doping level. For optimal doping with $x = 0.16$, the Josephson plasma resonance frequency in $La_{2-x}Sr_xCuO_4$ reaches a maximum value, and the superconducting state is characterised by a homogeneous superfluid density in the planes. As a result, a description of c-axis transport in terms of the two fluid model (see chapter 3.3) is possible (Dordevic *et al.*, 2003).

In the normal state, the resistivity ratio was measured to be $\rho_c/\rho_{ab} \approx 450$ at $T = 40$ K in the sample used in the experiments described in this thesis. In the superconducting state, the anisotropy ratio of the penetration depth is $\gamma = \lambda_c/\lambda_{ab} \approx 15$. The directional anisotropy of $La_{2-x}Sr_xCuO_4$ leads to inherently different charge dynamics depending on the direction of carrier transport. In the following sections,

terahertz time-domain spectroscopy measurements probing the in- and out-of-plane response of optimally doped $La_{2-x}Sr_xCuO_4$ are being presented.

5.1 *c*-Axis Electrodynamics of $La_{1.84}Sr_{0.16}CuO_4$

Apart from vanishing d.c. resistivity and the manifestation of the Meissner effect through the development of a $-1/\omega^2$ frequency dependence of the real permittivity, the *c*-axis electrodynamics in the superconducting state are characterised by a third key feature. The combination of the layers' capacitive coupling and tunnelling between the planes, which has an equivalent inductive impedance, gives rise to collective plasma oscillations of Cooper-paired electrons, or Josephson plasma waves (Orenstein and Mills, 2000). The insulating planes in layered cuprates have thicknesses of the order of interatomic distances, resulting in plasma frequencies in the terahertz regime. The Josephson plasma resonance in cuprates, typically investigated using frequency domain techniques (Tamasaku *et al.*, 1992), can be observed directly by time-domain terahertz spectroscopy (Thorsmølle *et al.*, 2001).

Figure 5.2 A shows single-cycle terahertz time-domain spectroscopy transient recorded by electro-optic sampling after reflection from the optimally doped cuprate $La_{1.84}Sr_{0.16}CuO_4$. The terahertz electric field is polarised parallel to the *c*-axis, probing the out-of-plane electromagnetic response. Measurements are carried out above and below the critical temperature $T_c = 36$ K. At low temperatures, the onset of the 2-THz Josephson plasma resonance is apparent in the long-lived oscillations on the trailing edge of the reflected pulse (red line). In the frequency domain, the plasma edge emerges in the amplitude of the Fourier transform of the two transients as shown in figure 5.2 B. While the reflected field gains spectral weight at low frequencies, a sharp dip develops close to ~ 2 THz.

In order to deduce the absolute sample reflectivity, the incident pulse has to be recorded for comparison. Here, the incident field is determined after reflection from a gold-coated portion of the sample surface. The frequency-dependent complex re-

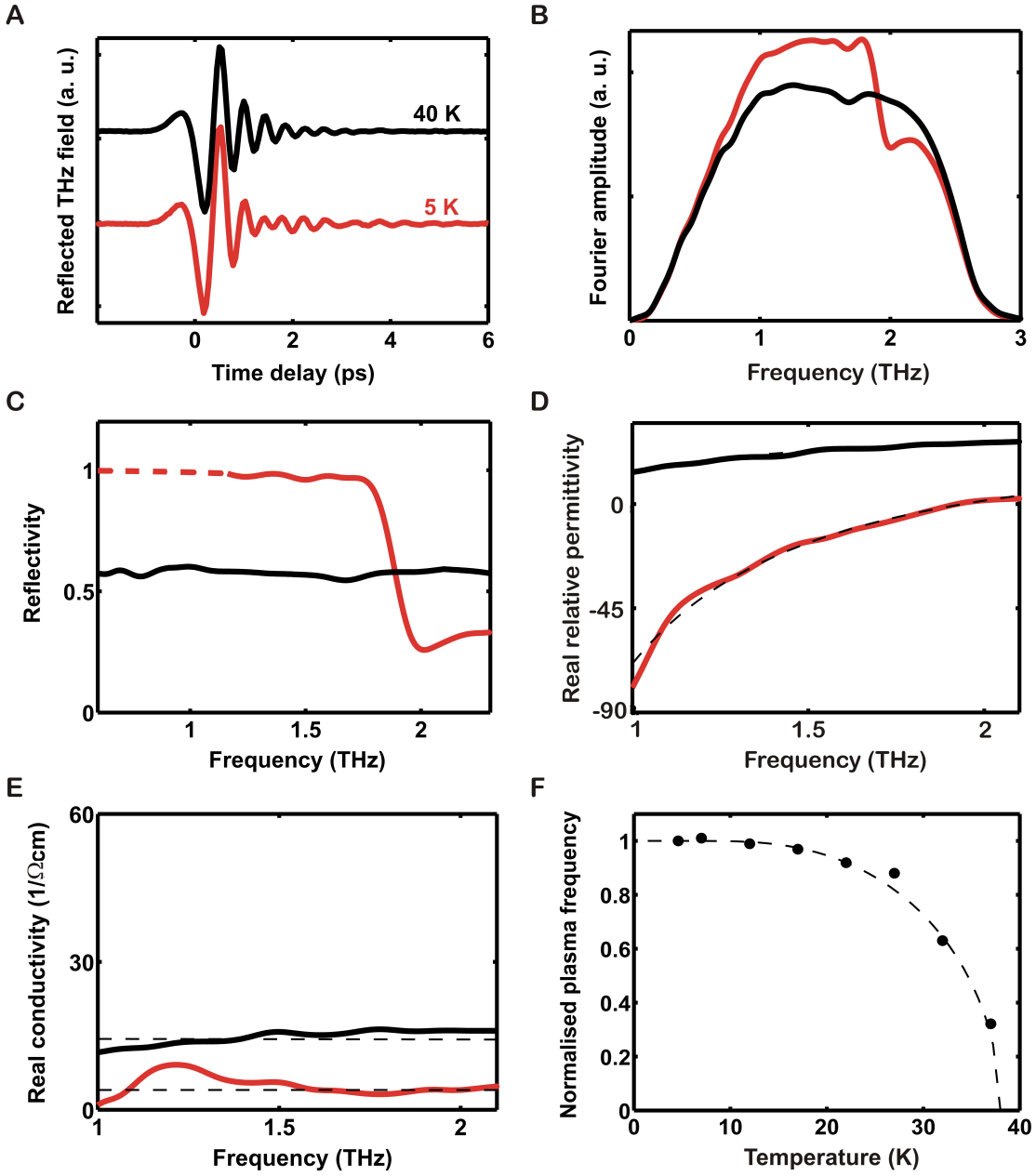


Figure 5.2: Out-of-plane equilibrium constants of $La_{1.84}Sr_{0.16}CuO_4$. A: Time-dependent terahertz transients detected after reflection from $La_{1.84}Sr_{0.16}CuO_4$ above and below T_c. For $T < T_c$, long lived oscillations on the trailing edge of the pulse signal the onset of interlayer Josephson coupling. B: Fourier amplitude of the probe traces versus frequency. Spectral weight increases at low frequencies for $T < T_c$, and a well-defined edge appears at ~ 2 THz. C: Intensity reflectivity in dependence of frequency. For $T > T_c$, the reflectivity is featureless and almost constant. A well-defined reflectivity edge develops at ~ 2 THz for $T < T_c$. D: Real part of the relative permittivity as a function of frequency. For $T > T_c$, the real permittivity is almost constant and positive. When $T < T_c$, a $-1/\omega^2$ frequency dependence arises, reflecting the superfluid response. The real permittivity crosses zero at the Josephson plasma frequency $\omega_J/2\pi$. A fit of the reflectivity edge with the two fluid model reproduces the data (dashed line). E: Real part of the conductivity in dependence of frequency. The real part is featureless over the whole frequency range for $T > T_c$. For $T < T_c$, the conductivity decreases, reflecting diminishing quasiparticle absorption. A fit of the reflection edge with the two fluid model reproduces the measurement (dashed line). F: Normalised Josephson plasma frequency $\omega_J(T)/\omega_J(0)$ in dependence of the temperature. With increasing temperature, the plasma resonance shifts to lower frequencies and disappears as $T \to T_c$. The data can be fitted (dashed line) based on the weak-coupling BCS theory in (Mühlschlegel, 1959; Homes *et al.*, 2004).

flection coefficient $r(\omega) = E_{refl}(\omega)/E_{inc}(\omega)$ is then derived as the ratio of the Fourier transforms of the reflected and incident fields. The intensity reflectivity $|r(\omega)|^2$ is displayed in figure 5.2 C. Above the superconducting transition temperate ($T > T_c$), the c-axis response is insulator-like and the reflectivity essentially featureless at a level of about 55% (black line). However, as the sample undergoes the superconducting transition ($T < T_c$), the reflectivity characteristics change dramatically (red line). The reflectivity approaches unity at low frequency, but drops sharply at about 2 THz. At higher frequencies, the reflectivity approaches that of the normal state. These measurements, which are reminiscent of the plasma edge observed in conventional metals (Kittel, 2005), reproduce the well-characterised Josephson plasma resonance in this compound (Tamasaku *et al.*, 1992; Dordevic *et al.*, 2003; Gerrits *et al.*, 1994).

Having determined the reflection coefficient $r(\omega)$, the equilibrium optical properties can be deduced using Fresnel's equations as described in section 2.1 above. Since measuring the incoming field after reflection from the thin gold layer on the sample introduces a small uncertainty in the phase of the transients, the reflectivity edge in figure 5.2 C was simultaneously fitted with the two fluid model. Figure 5.2 D displays the real part of the complex frequency-dependent relative permittivity $\mathrm{Re}\{\epsilon(\omega)\}$. Above the transition temperature, the real permittivity is almost frequency-independent and determined by the high-energy phonon contribution ϵ_∞. The plasmon is overdamped and can not be observed in the normal state (black line). For $T < T_c$, the damping vanishes, and the superfluid response gives rise to the characteristic $-1/\omega^2$ frequency dependence (red line). The reason for this is that the real part of the permittivity is directly related to the superfluid density ρ as $\mathrm{Re}\{\epsilon(\omega)\} = -\rho/\omega^2$, which represents a measure for the condensate stiffness at equilibrium (see section 3.3 above). The interplay of phonon background and superfluid contribution leads to the zero crossing of the real permittivity at the Josephson plasma frequency $\omega_J/2\pi \approx 2$ THz. A fit of the two fluid model to the reflectivity edge reproduces the measurements of the real permittivity at both temperatures (thin dashed lines).

The real part of the optical conductivity, reflecting the amount of dissipation of electromagnetic energy in the medium, is displayed in figure 5.2 E. The real conductivity is indicative of an insulating state for $T > T_c$ (black line), since charge transport along the c-axis is incoherent and dominated by interlayer hopping. Upon cooling through the transition temperature, the material shows a depression of the real conductivity at terahertz frequencies, because electron pairs form and enter the condensate. However, a residual conductivity remains even at low temperatures ($T \ll T_c$), and no evidence can be found for the emergence of the superconducting gap. The real part of the conductivity is reproduced by a fit of the two fluid model to the reflectivity edge (thin dashed lines).

Figure 5.2 F summarises the temperature dependence of the Josephson resonance in $La_{1.84}Sr_{0.16}CuO_4$, reporting the plasma frequency ω_J as a function of temperature T on a normalised scale. For low temperatures, the plasma frequency increases and saturates, corresponding to a strengthening and eventual saturation of the superfluid density. As the temperature approaches T_c from below, the plasma frequency continuously tends to zero, reflecting the disintegration of the condensate. The measured characteristics of the plasma frequency in $La_{1.84}Sr_{0.16}CuO_4$ are well-fitted by utilising the temperature-dependence of the superconducting gap energy, which is predicted by the BCS theory assuming a transition temperature of $T_c = 38$ K (Mühlschlegel, 1959; Homes *et al.*, 2004).

5.2 *ab*-Plane Electrodynamics of $La_{1.84}Sr_{0.16}CuO_4$

Vanishing d. c. resistivity and the expulsion of magnetic fields for $\omega \to 0$ through the Meissner effect are the two defining properties of the in-plane superconducting transition. Terahertz time-domain spectroscopy can be applied to examine the transition experimentally.

Figure 5.3 A shows the Fourier amplitudes of time-domain spectroscopy measurements in which the terahertz electric field polarisation is parallel to the supercon-

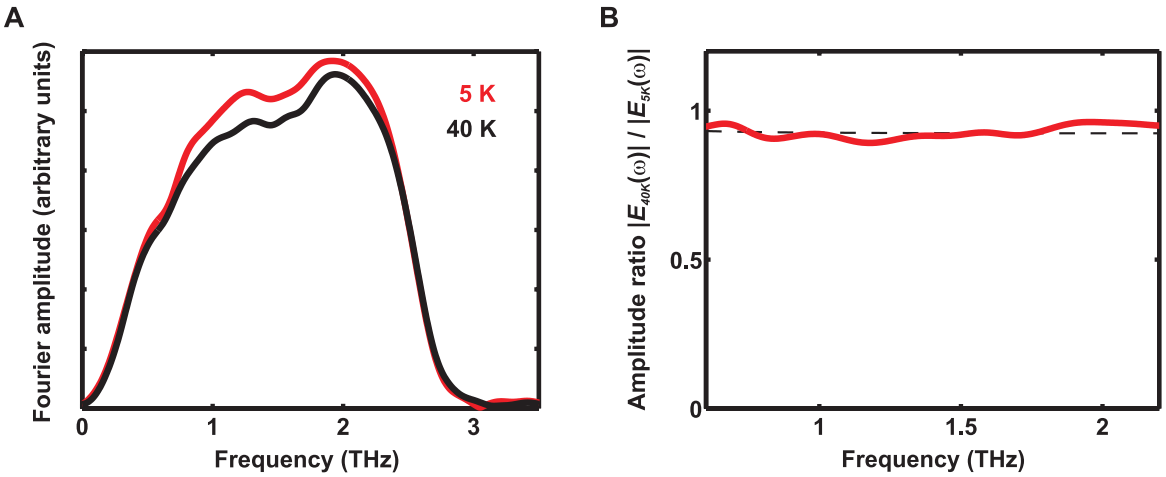


Figure 5.3: In-plane equilibrium reflectivity of $La_{1.84}Sr_{0.16}CuO_4$. A: Fourier amplitude of terahertz transients detected by electro-optic sampling after reflection from $La_{1.84}Sr_{0.16}CuO_4$ in dependence of frequency. The electric field is polarised parallel to the *ab*-layers, probing the in-plane response. In the superconducting state, spectral weight increases almost independent of frequency with respect to the normal state. B: Amplitude ratio $|E_{40K}(\omega)|/|E_{5K}(\omega)|$ as a function of frequency. The relative reflectivity is fitted with the two fluid model (dashed line).

ducting layers, probing the in-plane response. As highlighted in figure 5.3 B, the relative reflectivity increases almost frequency independent by several percent when the sample is cooled below the transition temperature.

The complex *ab*-plane optical properties are determined by using literature values for the two-fluid model description of $La_{1.84}Sr_{0.16}CuO_4$, which reproduce the relative reflectivity $|E_{40K}|/|E_{5K}|$ measured in our experiment (dashed line in figure 5.3 B) (Gorshunov *et al.*, 1998; Fudamoto *et al.*, 2003; Tajima *et al.*, 2005; Basov and Timusk, 2005). Figure 5.4 A depicts the real part of the complex relative permittivity at both temperatures below and above T_c. Above the critical temperature $T > T_c$, the in-plane response is that of a bad metal, manifested in a featureless almost constant intensity reflectivity at low frequencies, dropping sharply at the in-plane plasma edge located at $\sim$ 120 THz. Accordingly, the real part of the normal state relative permittivity is almost constant at low frequencies, taking a value close to zero. When entering the superconducting state, the real permittivity develops the characteristic $-1/\omega^2$ frequency dependence, reflecting the stiffening of the condensate and the Meissner effect as $\omega \to 0$.

Figure 5.4 B shows the real part of the conductivity. In the metallic state, the real

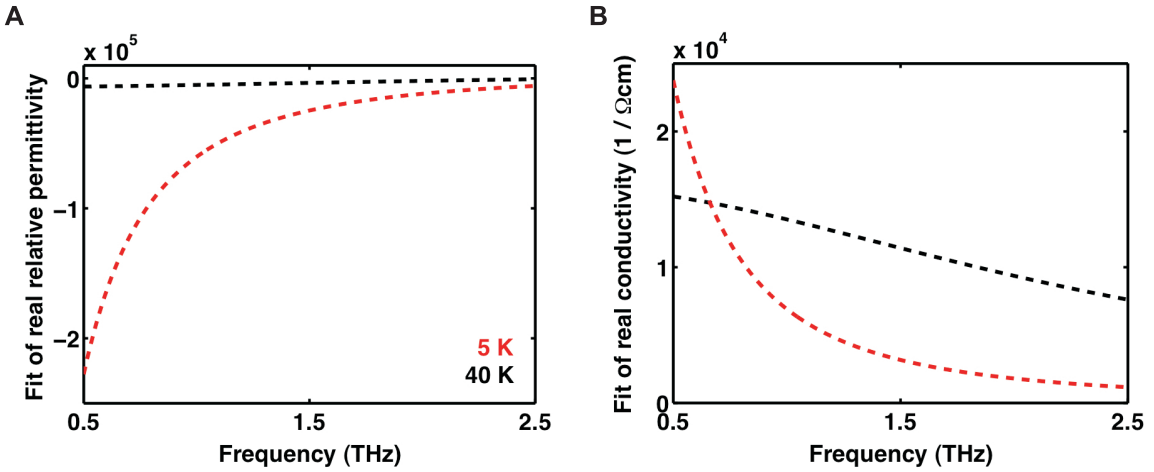


Figure 5.4: Plot of literature values of the in-plane equilibrium properties of $La_{1.84}Sr_{0.16}CuO_4$. A: Plot of the real relative permittivity as a function of frequency. The conductivity data is obtained using literature values of the well-characterised in-plane properties of the material (Gorshunov *et al.*, 1998; Fudamoto *et al.*, 2003; Tajima *et al.*, 2005; Basov and Timusk, 2005), which reproduce the relative reflectivity of figure 5.3 B (dashed line). For $T > T_c$, the real permittivity is almost frequency-independent. Due to the superfluid response, the real part of the permittivity develops a $-1/\omega^2$ dependence when $T < T_c$. B: Plot of the real conductivity as a function of frequency. When cooled below the transition temperature, the real conductivity increases below ~ 1 THz, and is strongly suppressed at higher frequencies when compared to the normal state. The missing spectral weight is accumulated in the superconducting delta function at zero frequency.

part of the conductivity shows an almost frequency-independent behaviour over a wide range up to several terahertz. Below the critical temperature, the real conductivity decreases for frequencies above $\sim$ 1 THz, while it increases for smaller frequencies. During the superconducting transition, the missing spectral weight in the real conductivity is accumulated in the superconducting δ function at zero frequency. However, unlike conventional low-T_c materials, $La_{1.84}Sr_{0.16}CuO_4$ does not show a well-defined conductivity gap in the in-plane superconducting response. Instead, a residual absorption is inherent to these materials, meaning that the density of states is finite at all energies. This is a scenario expected for d-wave superconducting transport, however, the measured magnitude of the residual conductivity cannot be accounted for within this framework for physically reasonable choices of the scattering rate and measured transition temperatures (Quinlan *et al.*, 1996).

The equilibrium optical properties of the optimally doped cuprate $La_{1.84}Sr_{0.16}CuO_4$ presented in this chapter provide the foundation for determining the out-of-equilibrium dynamics presented in the remaining part of this thesis.

Chapter 6

Bi-Directional Electric-Field Gating of Superconductivity

In the superconducting state, tunnelling between planes underpins three-dimensional coherent charge transport in cuprates. However, the interlayer tunnelling amplitude is reduced when an order parameter phase gradient is established in the direction perpendicular to the planes. As such, interlayer superconductivity along the *c*-axis can be weakened if a strong electric field is applied in the same direction. Here, high-field single-cycle terahertz pulses generated by tilted pulse front excitation in lithium niobate are used to gate interlayer coupling in $La_{1.84}Sr_{0.16}CuO_4$. Ultrafast oscillations between superconducting and resistive states are induced, and the plasmon response is switched on and off, without reducing the density of Cooper-pairs in the copper oxygen layers. Indeed, in-plane superconductivity remains unperturbed, revealing a non-equilibrium state in which the dimensionality of the superconducting transport is time-dependent. The gating frequency is determined by the electric field strength in the spirit of the a. c. Josephson effect. Non-dissipative, bi-directional gating of superconductivity is of interest for device applications in ultrafast nanoelectronics and represents an example of nonlinear terahertz physics, applicable to nanoplasmonics and active metamaterials.

6.1 Linear Josephson Plasma Resonance

Superconducting transport in layered cuprates can be understood by considering a stack of intrinsic Josephson junctions, made of superconducting planes which are separated by insulating layers. Three key features characterise the *c*-axis electrodynamics in the superconducting state. First, the d. c. resistivity vanishes, as superconductive tunnelling shorts resistive transport through incoherent quasi-particles. Second, the imaginary part of the conductivity displays $1/\omega$ frequency dependence, reflecting diamagnetism and the Meissner effect as $\omega \rightarrow 0$. Third, the combination of tunnelling, which has an equivalent inductive impedance, and capacitive coupling between the planes, leads to collective plasma oscillations of superconducting electrons at terahertz frequencies, or Josephson plasma waves (Orenstein and Mills, 2000).

These properties, which are typically measured in the frequency-domain (Tamasaku *et al.*, 1992), can be observed directly with time-domain terahertz spectroscopy (Thorsmølle *et al.*, 2001). Figure 6.1 a shows one such electro-optic sampling measurement of a single-cycle terahertz field, after reflection from the optimally-doped cuprate $La_{1.84}Sr_{0.16}CuO_4$ (Takagi *et al.*, 1989; Shibauchi *et al.*, 1994). In the superconducting phase (red curve), long-lived oscillations at 2-THz frequency appear on the trailing edge of the pulse. The incident field is measured after reflection from a gold-coated fraction of the sample surface. The frequency-dependent complex reflection coefficient $r(\omega) = E_{refl}(\omega)/E_{inc}(\omega)$ is derived by dividing the Fourier transforms of the time-dependent reflected field of figure 6.1 a by the incident one. The intensity reflectivity $|r(\omega)|^2$ is displayed in Figure 6.1 b, and reproduces well the Josephson plasma edge in this compound.

In figure 6.1 c, the complex frequency-dependent dielectric function $\epsilon(\omega)$ of the equilibrium low-temperature state is displayed, extracted by the procedure explained in section 5.1 above. As for any plasmonic response, the real part $\mathrm{Re}\{\epsilon(\omega)\}$ is negative for $\omega < \omega_J$, where $\omega_J/2\pi \approx 2$ THz is the frequency of the Josephson plasma resonance in $La_{1.84}Sr_{0.16}CuO_4$. The imaginary part $\mathrm{Im}\{\epsilon(\omega)\}$ is nearly zero over the

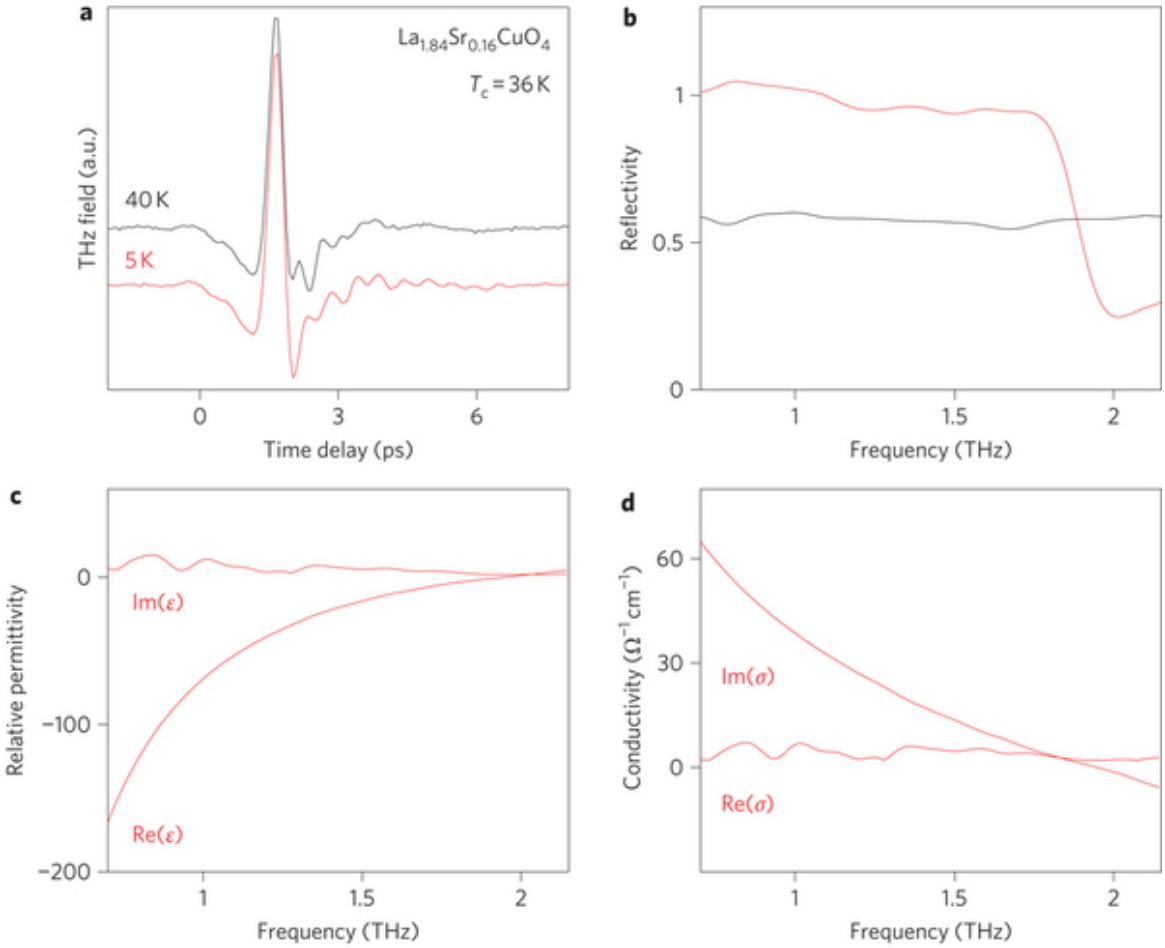


Figure 6.1: Linear optical response of $La_{1.84}Sr_{0.16}CuO_4$. In $La_{2-x}Sr_xCuO_4$, x = 0.16 corresponds to the optimal doping level (Takagi *et al.*, 1989). The anisotropy is a decreasing function of doping, both in the normal and superconducting states. In the normal state, the resistivity ratio decreases for $x > 0.08$, and is measured to be $\rho_c/\rho_{ab} \approx 450$ at $T = 40$ K in the sample used here. In the superconducting state, the anisotropy ratio of the penetration depth is $\lambda_c/\lambda_{ab} \approx 15$. a: Reflected terahertz electric fields from $La_{1.84}Sr_{0.16}CuO_4$, above (black curve, 40 K) and below (red curve, 5 K) $T_c = 36$ K. The probe electric field is polarised along the *c*-axis, probing interlayer transport. b: Electric field intensity reflectivity spectrum above (black curve, 40 K) and below (red curve, 5 K) $T_c = 36$ K. c: Real and imaginary part of the frequency-dependent equilibrium permittivity $\epsilon(\omega)$ at 5 K. While $\mathrm{Im}\{\epsilon(\omega)\}$ is small indicating negligible dissipation, $\mathrm{Re}\{\epsilon(\omega)\}$ highlights the plasmonic response crossing zero at the plasma frequency $\omega_J/2\pi \approx 2$ THz. d: Real and imaginary part of the equilibrium conductivity $\sigma(\omega)$ in the superconducting state at 5 K. $\mathrm{Re}\{\sigma(\omega)\}$ is small and almost frequency-independent since the spectral weight is accumulated in the superconducting delta function at zero frequency. $\mathrm{Im}\{\sigma(\omega)\}$ exhibits a $1/\omega$ dependence representing the Meissner effect and diamagnetic response as $\omega \to 0$. The figure was first published in (Dienst *et al.*, 2011a).

whole frequency range, indicating negligible dissipation by non-superconducting quasiparticles. In figure 6.1 d, the low temperature conductivity $\sigma(\omega)$ is displayed, which is characterised by a vanishing real part for finite frequencies, and a $1/\omega$ frequency dependence in its imaginary component, $\mathrm{Im}\{\sigma(\omega)\} = \rho/4\pi\omega$. Here, ρ represents the superfluid density, a measure for the stiffness of the condensate at equilibrium (Basov

et al., 1999). These equilibrium transport properties have been discussed extensively in the past, especially with regard to the controversial role of interlayer tunnelling in high-T_c superconductivity (Anderson, 1998; Moler *et al.*, 1998; Tsvetkov *et al.*, 1998).

The present work aims at perturbing interlayer Josephson coupling without injecting incoherent excitations, in order to gate *c*-axis transport at high frequencies. It is known that interlayer transport can be altered statically by application of magnetic (Schafgans *et al.*, 2010) or electric fields (Kleiner and Müller, 1994). This is possible because tunnelling across a weak link depends on the order parameter phase difference ϕ between the two superconductors, which is affected by application of external electromagnetic fields (Josephson, 1962, 1964).

To obtain a simple estimate of the required terahertz field strengths, it is instructive to consider the voltage drop V, that corresponds to an induced phase difference of $\pi/2$ according to the time integral of equation (4.5) above, yielding

$$\phi(t) = \int^{t} \frac{2e}{\hbar} V(t')\mathrm{d}t' \equiv \frac{\pi}{2} \quad . \tag{6.1}$$

If the voltage V is assumed to be constant over the time duration of 1 ps this implies

$$V = \frac{\pi}{4e} \frac{\hbar}{1\,\mathrm{ps}} \sim \mathrm{mV} \quad . \tag{6.2}$$

Thus, to achieve the gating effect on ultrafast timescales, interlayer voltage drops of few to tens of mV are needed. This implies that for interlayer distances of the order of 10 Å (Kubo *et al.*, 2009), peak electric fields of tens of kV/cm are required since

$$E_{pump} \sim \frac{1\ \mathrm{mV}}{1\ \mathrm{nm}} = 10\ \frac{\mathrm{kV}}{\mathrm{cm}} \quad . \tag{6.3}$$

Hence, application of the tilted pulse front technique introduced in section 2.3 above allows to exceed the required fields by at least one order of magnitude assuming modest focussing constraints.

6.2 Experimental Realisation

High-field terahertz transients are achieved in the experiment using the tilted-pulse front technique, which is applied to generate μJ single-cycle pulses by optical rectification in $LiNbO_3$ (Hebling *et al.*, 2008a). The pulses are tuned to a centre frequency of 450 GHz, well below the 2-THz Josephson plasma edge as displayed in figure 6.2. The gate field wavelength is $\sim$ 0.65 mm, and can be focused down to spot sizes of approximately 1 mm^2, reaching field strengths up to 100 kV/cm. The gate field is polarised perpendicular to the planes and is completely reflected, penetrating over a distance of 5 μm as an evanescent wave.

The time-dependent reflectivity of $La_{1.84}Sr_{0.16}CuO_4$ is probed both perpendicular and parallel to the planes with a delayed terahertz probe pulse. The probe bandwidth extends up to 2.5 THz and, for *c*-axis polarisation, it covers the Josephson plasma edge (see figure 6.2). To extract the time-dependent conductivity, the amplitude- and phase-resolved transients are fitted by the model described in section 2.4, considering a 5-μm-thick surface layer of unknown conductivity, over an unperturbed semi-infinite superconductor with the optical properties of figure 6.1 d.

The experimental realisation of the pump-probe apparatus is schematically shown in figure 6.3. Near-infrared radiation of $\sim$ 800 nm central wavelength is delivered by a titanium-doped sapphire laser at a repetition rate of 1 kHz. The pulse duration accounts for $\sim$ 100 fs, while the average pulse energy is measured to be 3.7 mJ. The initial laser output is split by a (98 % transmission, 2 % reflection) beamsplitter (BS_1), whereas the small reflected component is denoted EOS since it is used for electro-optic sampling of the terahertz probe pulses.

The transmitted component is again divided by a (92 % transmission, 8 % reflection) beamsplitter (BS_2). The smaller reflected part of the 800 nm light is used to generate the broadband single-cycle probe pulses via optical rectification in a (110)-cut zinc telluride (ZnTe) crystal of 500 μm thickness. The terahertz probe pulses are subsequently focussed onto the sample using an off-axis parabola (OAP), and

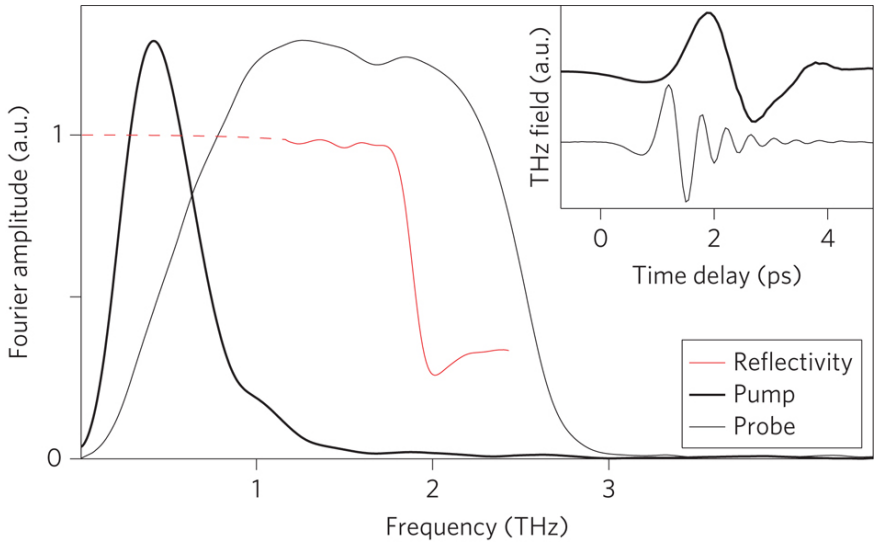


Figure 6.2: Characterisation of pump and probe pulses. Scaled spectra of terahertz pump (thick black curve) and probe (thin black curve) pulses, overlaid to the $La_{1.84}Sr_{0.16}CuO_4$ reflectivity edge at 5 K (red curve). The inset shows typical time-domain transients of THz pump and probe pulses measured by electro-optic sampling. The figure was first published in (Dienst *et al.*, 2011a).

reflected at 45° (with respect to the surface normal) for coherent detection. To this end, the probe is collimated and subsequently focussed onto the second zinc telluride detection crystal of 1 mm thickness, spatially and temporally overlapping with the near-infrared EOS beam. The main share of the split beam (at BS_2) is used to generate the high-intensity terahertz radiation pump pulses by tilted pulse front excitation in lithium niobate. The pump is focused onto the sample using an off-axis parabolic mirror, spatio-temporally overlapping with the probe pulses.

It is important to discuss the minimum temporal resolution achievable in this experimental setup. A measurement scheme with two translation stages is employed in which the temporal delay between electro-optic sampling gate field at the zinc telluride detection crystal and pump field is kept constant. This guarantees that the measured terahertz probe transients experience as a whole the same pump-probe time delay, avoiding artefacts that arise when the material response is faster than the terahertz probe duration (Kindt and Schuttenmaer, 1999; Averitt *et al.*, 2000). The temporal resolution in this scheme is not limited by the terahertz pump pulse envelope duration, but rather by the response time of the electro-optic detection system which is on the order of 150 fs. The response is determined by the electro-optic sampling

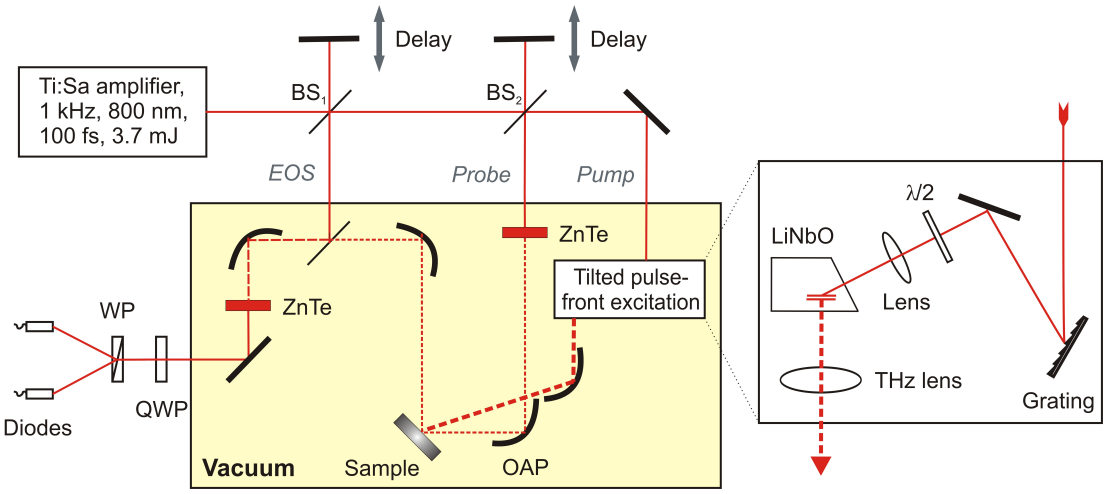


Figure 6.3: Experimental realisation of electric-field gating. An amplified titanium-sapphire laser provides femtosecond pulses in the near-infrared. Single-cycle high-field terahertz pump pulses are generated with the tilted pulse front technique and focussed onto the sample. The excited sample is probed by terahertz time-domain spectroscopy. Optical delay lines regulate the relative time delay between pump and probe pulses as proposed in references (Kindt and Schuttenmaer, 1999; Averitt *et al.*, 2000). Terahertz generation, propagation and detection takes place in vacuum to avoid absorption effects in air.

gate pulse duration, and by the coherence length of terahertz and optical pulse within the zinc telluride crystal. In a 1 mm thick crystal the latter corresponds to 3 THz (Nahata *et al.*, 1996). A temporal resolution of 150 fs full width at half maximum therefore is a safe assumption.

6.3 Ultrafast Electric-Field Gating

The key observation of this work is reported in the two-dimensional plots of figure 6.4 a, which display the frequency-dependent conductivities (real and imaginary part) for different time delays τ between a 80 kV/cm single-cycle gate field and the probe pulse. In the two upper panels, c-axis measurements are displayed. As the gate electric field evolves in time, superconductive coupling vanishes for $\tau = 1.25$ ps, as qualitatively shown by the loss of spectral weight in the imaginary conductivity, and in the corresponding gain of the real part. Remarkably, superconductive transport is re-established within a few hundred femtoseconds ($\tau = 1.5$ ps), when the conductivity of the unperturbed superconductor is recovered. Oscillations between the states follow.

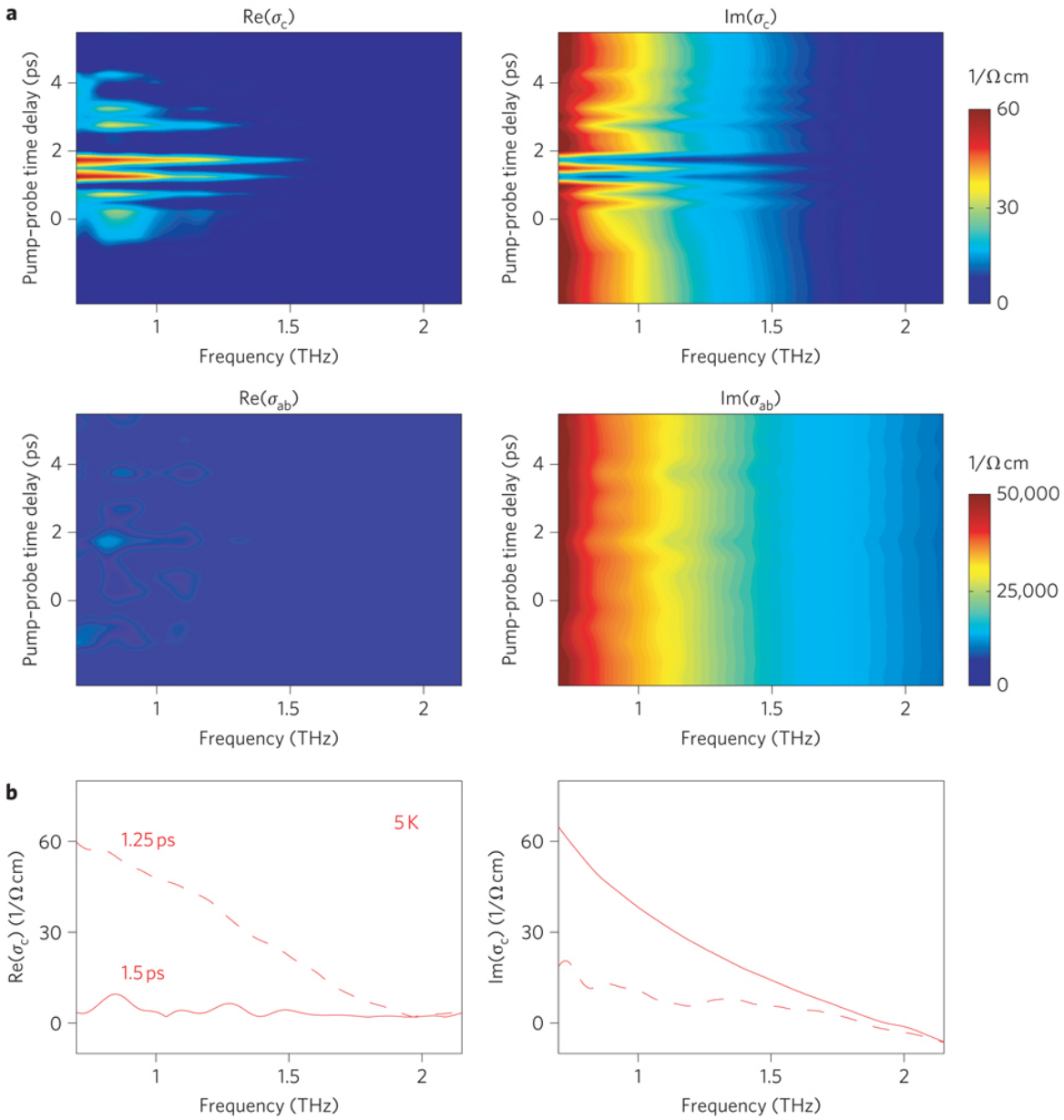


Figure 6.4: Time-dependent optical conductivity. a: The upper panels show two-dimensional plots of real and imaginary part of the c-axis conductivity $\sigma_c(\omega, \tau)$ for different pump probe time delays, measured at 5 K. Pump and probe polarisation are parallel to the c-axis. The pump field strength is 80 kV/cm. For $\tau < 0$, the lineouts reflect the unperturbed optical conductivity. As the gate field progresses, the conductivity oscillates rapidly between resistive and superconductive states. Oscillations persist for a couple of picoseconds, comparable to the Josephson coherence time. The lower two panels display the low-temperature in-plane conductivity $\sigma_{ab}(\omega, \tau)$, measured by rotating the probe polarisation by 90 degree to be parallel to the ab-plane, whilst the pump polarisation is kept parallel to the c-axis. b: Lineouts of the real and imaginary part of the c-axis conductivity $\sigma_c(\omega, \tau)$ at the peaks and the troughs of the oscillations depicted in panel a, exhibiting resistive ($\tau = 1.25$ ps) and superconductive ($\tau = 1.5$ ps) interlayer coupling. The figure was first published in (Dienst *et al.*, 2011a).

Figure 6.4 b shows lineouts of the complex conductivity at the peaks and the troughs of these oscillations. At negative time delays and in the recurring superconducting states, $\mathrm{Re}\{\sigma(\omega,\tau)\}$ nearly vanishes at all frequencies, whilst $\mathrm{Im}\{\sigma(\omega,\tau)\}$ follows a $1/\omega$ frequency dependence, as in figure 6.1 d. At time delays were resistive states are established (dashed curve), the real conductivity is the dominant contribution and tends to a finite value σ_0 for $\omega \to 0$, as expected for a Drude gas of incoherent quasi-particles. Here, it is interesting to note the long scattering time ($\sim$ 1 ps) for the quasiparticle c-axis transport, which could be attributed to the decreased density of unpaired electrons compared to $T > T_c$. In the resistive state, the imaginary conductivity still exhibits its $1/\omega$ dependence, but with a strongly depleted pre-factor.

A second important observation results from the ab-plane conductivity, which remains essentially unperturbed throughout these dynamics as displayed in the lower panels of figure 6.4 a. Effectively, the dimensionality of the superconductivity oscillates in time as the planes are decoupled, an exotic phenomenon never observed to date. The fact that the in-plane optical properties do not show significant change reinforces the notion that the strong terahertz field perturbs the phase but does not ionise the Cooper-pairs, maintaining the modulus of the order parameter unperturbed.

6.4 Field to Frequency Conversion

The physics observed here can be quantitatively discussed as follows. As can be seen from equation (4.7) introduced in chapter 4 above, the interlayer coupling strength is described by an equivalent tunnelling inductance L, which is proportional to $1/\cos\phi$ (Josephson, 1962). At equilibrium when $\phi \approx 0$, the inductance L is minimum and transport by non-condensed, incoherent quasi-particles is optimally shorted. For weak electric fields, a supercurrent J_s is driven through the layers, and a gradient in ϕ develops across the junction, as, according to the first Josephson equation, $J_s \propto \sin\phi$.

For large fields, as L increases, ohmic conduction by quasi-particles becomes relevant and a voltage drop V develops across the junction. At this point the order

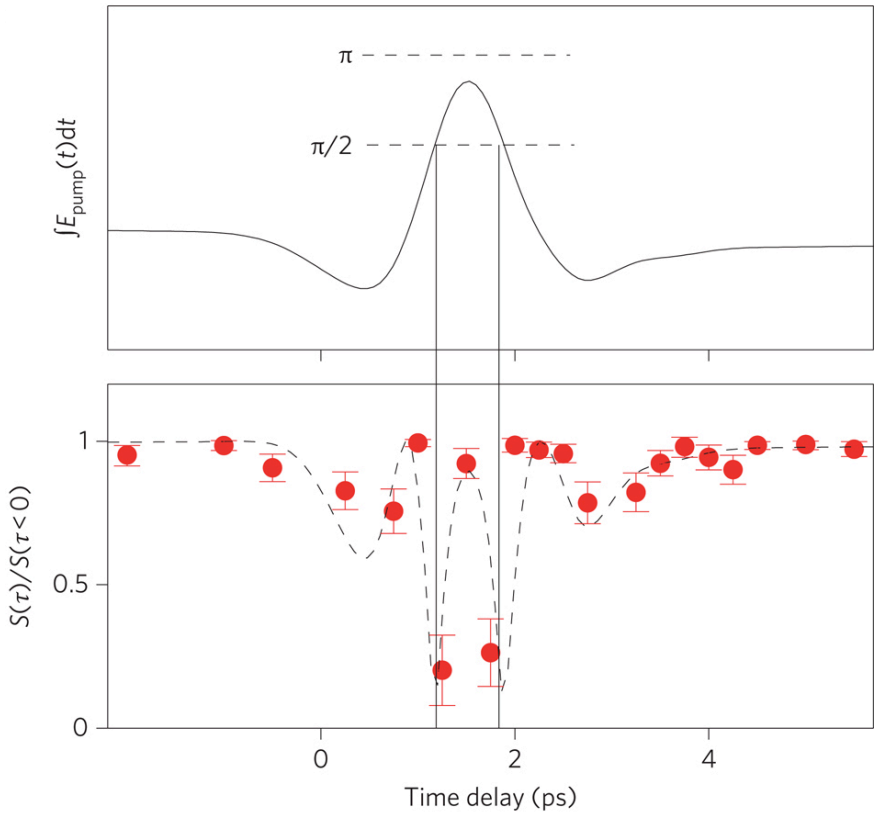


Figure 6.5: Ultrafast electric field gating of superconductivity. The upper panel shows the normalised integral of the measured terahertz pump transient as a function of time delay, being proportional to the advancement of the interlayer phase difference $\phi(t) \propto \int^t E_{pump}(t')\mathrm{d}t'$. The lower panel shows $S(\tau) = \lim_{\omega\to 0} \omega \mathrm{Im}\{\sigma(\omega,\tau)\}$ as a measure of interlayer coupling strength extracted from our experimental data (red dots), together with error bars obtained from the low-frequency extrapolation. The coupling strength is fit by the function $|\cos(c\int^t E_{pump}(t')\mathrm{d}t')|$ (black dashed line), where c is left as free parameter. The figure was first published in (Dienst *et al.*, 2011a).

parameter phase difference starts advancing in time according to the second Josephson equation, that is, as $\dot{\phi} = 2eV(t)/\hbar$, where e is the electron charge and $\hbar$ Planck's constant. The tunnelling evolves then as $L \propto 1/\cos\phi$, diverging when ϕ crosses $\pm\pi/2$, and changing sign in between.

The upper panel of figure 6.5 reports the normalised time integral of the gate electric field $\int^t E_{pump}(t')\mathrm{d}t'$, derived from the measured terahertz pump transients $E_{pump}(t)$. The field integral is compared to the quantity $S(\tau) = \lim_{\omega\to 0} \omega \mathrm{Im}\{\sigma(\omega,\tau)\}$ displayed in the lower panel, which represents the measured time-dependent strength of c-axis superconducting transport (Basov *et al.*, 1999). Under equilibrium conditions, this quantity is proportional to the superfluid density ρ (see section 3.3 above). Here, $S(\tau)$ is used as a measure of the non-equilibrium interlayer coupling strength,

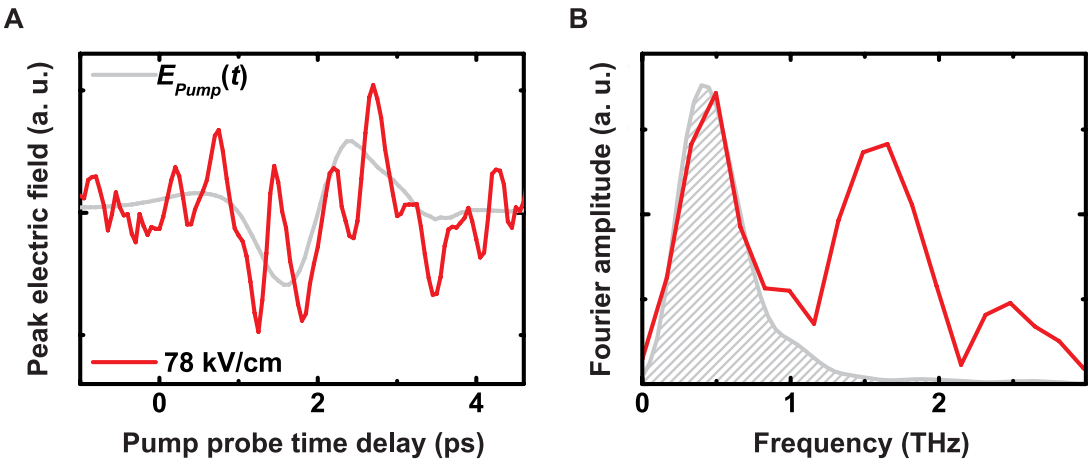


Figure 6.6: Pump-induced modulation of peak probe field. A: For an excitation fluence below a certain threshold, the peak electric field of the probe pulse is modulated in time in conformity with the measured time-dependent pump transient (grey line). When the excitation field strength exceeds a critical value, a more rapid oscillation is superimposed onto the slow modulation (red line, 78 kV/cm). B: Fourier amplitude as a function of frequency for the two curves displayed in panel A. For excitation above the threshold (red line, 78 kV/cm), the electric field is modulated at the pump frequency (grey line), however, a distinct second spectral peak emerges at higher frequencies.

and is well-fitted by the function $|\cos(c\int^t E_{pump}(t')\mathrm{d}t')|$ with only the constant c left as free parameter. As the integral of the driving voltage evolves, and as ϕ crosses $\pi/2$, the coupling $S(\tau)$ vanishes, recovering as ϕ is driven towards π. The model does not fit well at low field strengths, as, according to the discussion above, the transport is still superconducting and no voltage drop develops. At high fields, the model faithfully reproduces the measured non-equilibrium interlayer coupling strength $S(\tau)$ over a large dynamic range.

The pump-induced oscillations of interlayer coupling can be investigated as shown in figure 6.6 A by sampling the peak of the terahertz probe field as a function of time delay (with respect to the pump pulse). Utilising a double-polariser configuration, it is possible to tune the terahertz electric field strength with high accuracy. For electric field strengths below a certain threshold, the peak probe field modulation resembles the electro-optic sampling signal of the pump transients (grey line). As a critical field strength is exceeded, an additional considerably faster oscillation is superimposed onto the slow modulation (red line).

Taking the Fourier transform of the time-dependent traces and comparing the

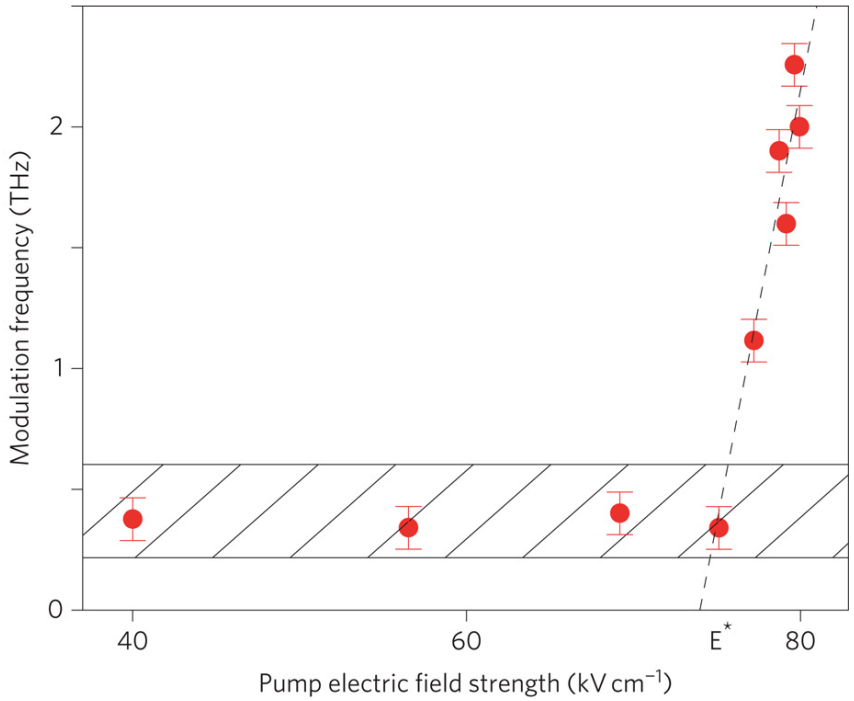


Figure 6.7: Field dependence of gating frequency. Modulation frequency as a function of terahertz gate electric field amplitude with estimated systematic error. Two regions can be distinguished: For low amplitudes $E_{pump} < E^{\star}$, the modulation occurs at the pump frequency (the shaded area represents the full width at half maximum of the pump amplitude spectra). Above the critical threshold $E^{\star}$, the modulation frequency increases linearly with field strength, reminiscent of the a. c. Josephson effect. The figure was first published in (Dienst *et al.*, 2011a).

amplitude to the pump spectrum as shown in figure 6.6 B reveals that the slow modulation occurs at the pump frequency. As the critical pump amplitude is exceeded, a second distinct amplitude component appears at higher frequencies. The higher component of the superconductive-resistive oscillation frequency is shown in figure 6.7 in dependence of the pump field strength. Two distinct regions are identified. Below $E^{\star} \approx 75$ kV/cm, the transport is modulated at the frequency of the pump. In this regime the interlayer phase difference is perturbed but it does not reach $\pi/2$ and the coupling is never completely shut off. For field strengths above $E^{\star}$, the modulation frequency increases linearly with the field in spirit of the a. c. Josephson effect.

To connect the threshold value $E^{\star}$ under these non-equilibrium conditions quantitatively to the material properties of $La_{1.84}Sr_{0.16}CuO_4$, it is most intuitive to make an argument based on energy scales. If one considers the energy gained by a pair of electrons ($2e$) tunnelling from one CuO_2 layer to the next across a gap of approximately

0.7 nm (the CuO_2 interlayer distance) being subject to electric fields of 75 kV/cm, one finds that this energy is of about $\sim$ 10 meV, a number close to the superconducting gap energy of optimally doped $La_{1.84}Sr_{0.16}CuO_4$ (Ino *et al.*, 1999).

6.5 Concluding Remarks

This voltage to frequency conversion is a new demonstration of nonlinear terahertz physics[†] that could be extended to photonic devices and modulators, but also to nanoplasmonic devices. In these applications, the rapid non-dissipative switching properties of the electric-field gating effect could be utilised (Chen *et al.*, 2006, 2007). Secondly, the effect allows for potential applications to nanoelectronics, since it is known that high-temperature superconductivity can be sustained in a single copper oxygen plane (Logvenov *et al.*, 2009). Because interlayer transport is determined by short range tunnelling between neighbouring layers, this phenomenon could be applied to single nanoscale junctions. Inspired by the present work, it would be interesting to explore terahertz pulse sequences with voltage integrals that drive the phase by multiples of $\pi/2$, in order to switch the dimensionality at will. These experiments would be relevant below and above the Berezinskii-Kosterlitz-Thouless temperature, corresponding to different regimes of stability for two-dimensional superconductivity. Finally, strong field perturbations of interlayer couplings (Fausti *et al.*, 2011) may be used to test new ideas of the physics of cuprates, including the case of striped states for which Josephson de-coupling might be important (Berg *et al.*, 2007).

[†]It is important to emphasise that the experiment described here is sensitive to the carrier envelope phase of the pump pulses. The signal observed represents a coherent response and is only present during the temporal overlap of terahertz pump and probe transients. However, the signal is not due to a mere "coherent artefact". In degenerate pump-probe spectroscopy, this notation applies when interference between the pump and probe pulses takes place, leading to a transient refractive index grating in the sample, which results in a modulation of the probe traces. Importantly, this type of wave-mixing is referred to as an artefact only when the time resolution is not high enough to extract the underlying coherent physics (Lebedev *et al.*, 2005). In this experiment, such an effect would occur at the frequency of the pump, which is not the case. The clear indicator that the response is not an artefact is the observation that the probed response changes and develops more oscillations when the terahertz field strength is increased, while all other parameters, especially the time-dependent terahertz electric field pulse form, are kept constant.

Chapter 7

Nonlinear Quantum Plasmonics in a Cuprate Superconductor

An opaque medium can become transparent if absorption through two simultaneous quantum paths is activated, leading to disruptive interference over a narrow spectral window. This is a general mechanism that is for example realised in electromagnetically induced transparency (EIT), as a strong laser field couples different atomic levels and drives absorption to zero (Fleischhauer *et al.*, 2005). Motivated by potential applications in quantum technology, recent realisations of related effects have been developed, making use of plasma excitations in gases and metamaterials (Harris, 1996; Liu *et al.*, 2009), quantum opto-mechanics (Weis *et al.*, 2010), and circuit quantum electrodynamics (Joo *et al.*, 2010). Here, strong-field narrowband terahertz pulses from a free electron laser are used to resonantly excite nonlinear Josephson plasma waves in the cuprate $La_{1.84}Sr_{0.16}CuO_4$, creating a metastable state that is transparent over a narrow spectral window. This is interpreted as the result of disruptive quantum interference between the linear plasma waves propagating in the cuprate and optically injected Josephson vortices, predicted by the sine-Gordon equation for the time- and space-dependent order parameter phase. The observations demonstrate the potential of layered superconductors for quantum nonlinear optics and show how such effects can make it possible to track vortex excitations on the ultrafast timescale.

7.1 Experimental Implementation

In the experiment reported in the present chapter, narrowband terahertz pump, broadband terahertz probe measurements are performed to selectively study multiple nonlinear optical phenomena, which are expected to occur above, at, or below the plasma resonance. To this end, an infrared free electron laser, which generates 50 ps pulses over a spectral bandwidth of $\sim 1\,\%$, is combined with a terahertz time-domain spectroscopy apparatus, and tuned to the 2-THz Josephson plasma resonance of $La_{1.84}Sr_{0.16}CuO_4$. A schematic of the experimental configuration is depicted in figure 7.1. Single-cycle probe pulses are generated using a photoconductive emitter excited by a femtosecond titanium-sapphire laser oscillator. The terahertz probe spectrum covers an extended bandwidth monitoring the frequency-dependent response around the 2-THz Josephson plasma resonance.

The narrow-bandwidth pump pulses are focused at the sample position reaching field strengths of ~ 2.5 kV/cm, a level that significantly perturbs the optical response near resonance[†] (Savel'ev *et al.*, 2006). The free electron laser pulses are characterised using a Czerny-Turner type spectrometer, which is integrated part of the optical beam diagnostics. The temporal duration of the pump pulses is determined by exploiting the terahertz Kerr effect in zinc telluride (Hoffmann *et al.*, 2009). Pump-probe time delays are fine-tuned with an optical delay line, while the coarse timing is achieved by offsetting the phase-locked loop that synchronises the laser oscillator and the free electron laser. Both pump and probe are polarised along the c-axis of $La_{1.84}Sr_{0.16}CuO_4$, perpendicular to the superconducting planes of the cuprate. The multi-cycle free electron laser pulses are tuned close to the plasma frequency, and the pump-induced change in the reflection coefficient is probed as a function of relative time delay.

Terahertz time-domain spectroscopy can be applied to observe the linear plasma resonance in the time- and frequency-domain (Thorsmølle *et al.*, 2001; Tamasaku

[†]Consider the energy gained by a pair of electrons tunnelling between the CuO_2 layers across a gap of ~ 1 nm being subject to electric fields of 2.5 kV/cm, one finds that this energy is ~ 0.5 meV, which is a sizeable fraction of the ~ 7 meV phase stiffness energy of optimally doped $La_{1.84}Sr_{0.16}CuO_4$.

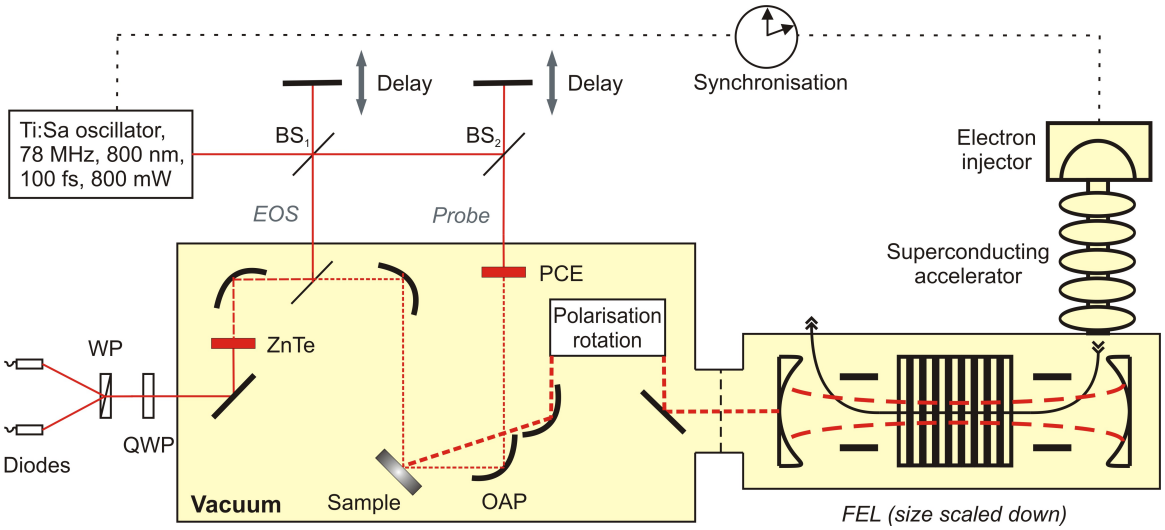


Figure 7.1: Experimental realisation of light-induced transparency. A free electron laser (right) is combined with a terahertz time-domain spectroscopy apparatus (left), allowing for narrow-band pump, broadband probe experiments at terahertz frequencies. The pump and probe pulses, which are both polarised perpendicular to the copper oxygen layers of $La_{1.84}Sr_{0.16}CuO_4$, are overlapped at the sample position. The relative time delay is fine-tuned using optical delay lines. The experiment takes place in a vacuum chamber, which is directly connected to the free electron laser.

et al., 1992). Figure 7.2 reports a measurement of the linear c-axis optical properties in the unexcited optimally doped cuprate $La_{1.84}Sr_{0.16}CuO_4$, probed with broadband terahertz pulses. Single-cycle terahertz transients are generated by a photoconductive antenna illuminated by a femtosecond laser-oscillator, and measured after reflection from the specimen by electro-optic sampling in a zinc telluride crystal. In the superconducting state ($T \ll T_c = 36$ K), long-lived 2-THz oscillations appear on the trailing edge of the pulse (see figure 7.2 A). By calibrating the incoming electric field after reflection from a gold-coated portion of the sample, the frequency-dependent complex reflection coefficient is derived via Fourier transformation as $r(\omega) = E_{refl}(\omega)/E_{inc}(\omega)$. The frequency spectrum of the probe pulse, covering the Josephson plasma edge, is plotted in figure 7.2 B, together with the intensity reflectivity $|r(\omega)|^2$ at 5 K.

Figure 7.2 C displays the real and imaginary part of the equilibrium relative permittivity $\epsilon(\omega) = \epsilon_1(\omega) + i\,\epsilon_2(\omega)$, determined by solving Fresnel's equations and fitting the reflectivity edge $|r(\omega)|^2$ with the two fluid model as described in chapter 5 above. The real part $\mathrm{Re}\{\epsilon(\omega)\}$ is negative for $\omega < \omega_J$, and the reflectivity is nearly unity over the whole range, as only an evanescent field penetrates into the solid. For $\omega > \omega_J$,

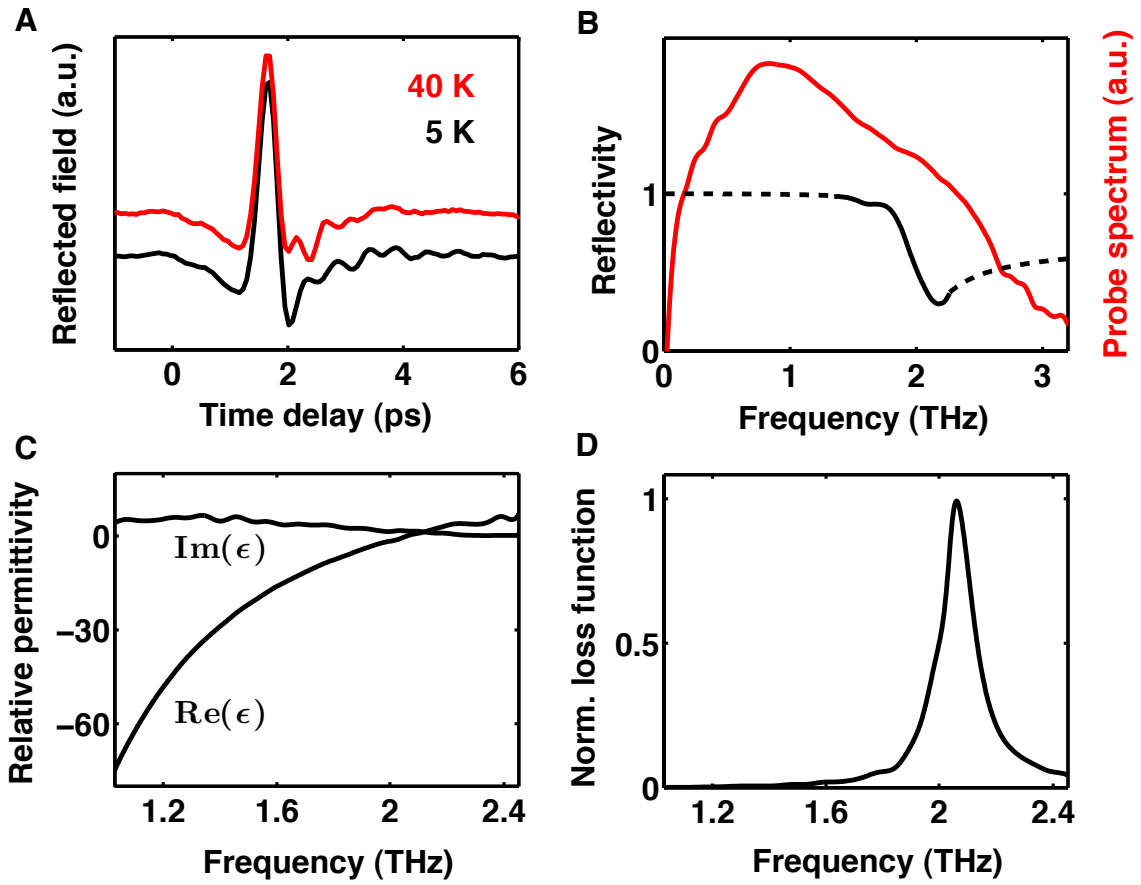


Figure 7.2: Linear plasmonics in $La_{1.84}Sr_{0.16}CuO_4$. A: Reflected terahertz time-domain transients recorded above (red line) and below (black line) the critical temperature $T_c = 36$ K. In the superconducting state, the plasma resonance is evident in the long-lived oscillations on the trailing edge of the pulse. B: Frequency-dependent probe spectrum on a logarithmic scale (red line) overlaid to the linear reflectivity edge (black line) measured at 5 K. C: Real and imaginary part of the complex frequency-dependent equilibrium permittivity $\epsilon = \epsilon_1 + i\,\epsilon_2$, determined at 5 K. D: Normalised equilibrium loss function $f(\omega)/f(\omega_J)$, with $f(\omega) = -\mathrm{Im}\{1/\epsilon(\omega)\}$, measured in the superconducting state at 5 K. The loss function captures the Josephson plasma physics, giving rise to a Lorentzian lineshape peaking at the resonance frequency with a width related to quasi-particle damping.

$\mathrm{Re}\{\epsilon(\omega)\}$ is positive and electromagnetic radiation can propagate inside the sample in the form of plasmon-polaritons. The imaginary part $\mathrm{Im}\{\epsilon(\omega)\}$ is small but finite over the whole frequency range, indicating weak dissipation by non-superconducting quasi-particles (Tamasaku *et al.*, 1992; Hu and Lin, 2010).

Figure 7.2 D exhibits the normalised equilibrium loss function $f(\omega)/f(\omega_J)$, where $f(\omega) = -\mathrm{Im}\{1/\epsilon(\omega)\}$. The physics of the Josephson plasma resonance is well encapsulated by this function, which exhibits Lorentzian lineshape and peaks at the plasma frequency. Thereby, the width of the loss function is determined by quasi-particle damping (Dordevic *et al.*, 2003).

7.2 Frequency-Selective Nonlinear Plasmonics

Figure 7.3 reports the time-dependent changes in reflectivity recorded for pump-probe excitation at 2.3 THz (panel A), 2.2 THz (panel B), 2.05 THz (panel C), and 1.9 THz (panel D). Three qualitatively different dynamics are observed. For excitation well above the plasma edge ($\omega_{FEL} > \omega_J$) as displayed in figure 7.3 A, a small increase of the reflectivity closely above the resonance frequency is recorded, which is suggestive of a marginal redshift of the edge. When the free electron laser is tuned closer to the resonance as reported in figure 7.3 B, the redshift of the plasma edge becomes more pronounced. The reflectivity decreases for frequencies below the Josephson plasma frequency ($\omega < \omega_J$), while it increases for frequencies above ($\omega > \omega_J$).

Contrary, when the free electron laser is tuned on resonance ($\omega_{FEL} \approx \omega_J$) as shown in panel 7.3 C, a drop in reflectivity at almost all frequencies is observed. Finally, for pump frequencies below the Josephson resonance ($\omega_{FEL} < \omega_J$) reported in figure 7.3 D, an increase in reflectivity for all frequencies above that of the pump ($\omega > \omega_{FEL}$), and decreases for frequencies below ($\omega < \omega_{FEL}$) is detected. This latter observation is suggestive of a mere reduction in the amplitude of the plasma edge, without a shift to lower frequencies.

To understand the different types of dynamics in more detail, the time-dependent optical properties of the photo-excited superconductor are extracted as follows. Starting from the equilibrium reflection coefficient $r_0(\omega)$ reported in figure 7.2 above, the amplitude- and phase-resolved non-equilibrium coefficient $r_0(\omega) + 6\Delta r(\omega)$ is fitted for each pump-probe time delay with a model that considers a surface layer of unknown permittivity over an unperturbed semi-infinite superconductor (see chapter 2.4). The scaling factor is motivated by the fact that the response is probed at 78 MHz, while the pump repetition rate is 13 MHz. The thickness of the excited surface layer is fixed to the pump-wavelength penetration depth. From these measurements, the time- and frequency-dependent loss function is extracted, which is displayed in figure 7.4.

When the free electron laser is tuned well above the Josephson plasma frequency

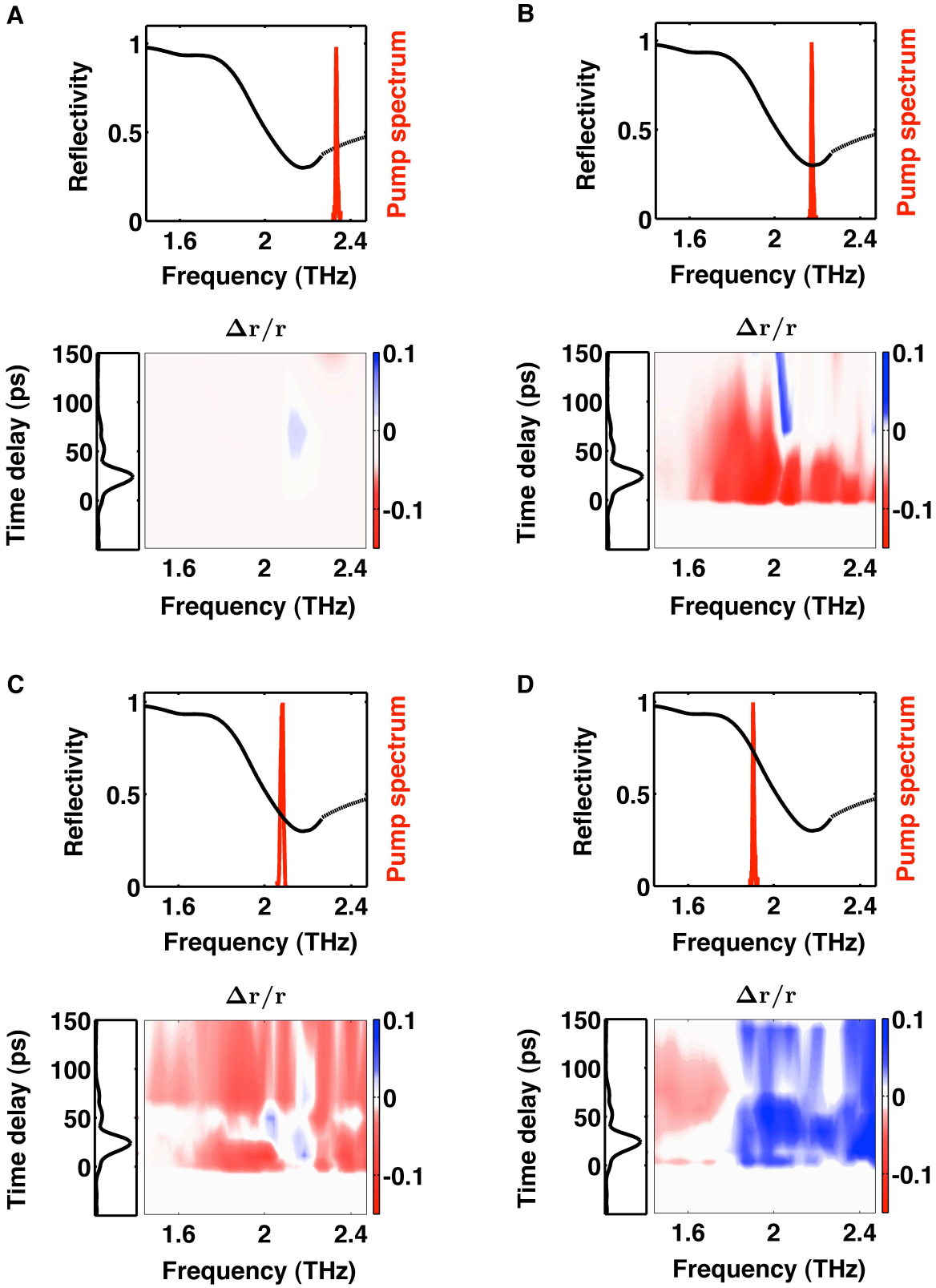


Figure 7.3: Reflectivity change for different excitation wavelengths. The upper panel of each subfigure reports the measured free electron laser spectrum overlaid to the low-temperature reflectivity of $La_{1.84}Sr_{0.16}CuO_4$. The lower panels depict the corresponding relative change in the frequency-dependent reflectivity as a function of time delay between the pump and probe pulses, compared to the Kerr signal of the excitation (Hoffmann *et al.*, 2009). The pump frequency in each panel reads: A: $\omega_{FEL} \approx 2.3$ THz. B: $\omega_{FEL} \approx 2.2$ THz. C: $\omega_{FEL} \approx 2.05$ THz. D: $\omega_{FEL} \approx 1.9$ THz.

($\omega_{FEL} > \omega_J$) as shown in figure 7.4 A, the loss function is minimally shifting to the red, but essentially remains unperturbed. However, for excitation just above the resonance, a rigid shift of the loss function to lower frequencies can be observed in figure 7.4 B. The dynamics are short-lived and persist only as long as the pump field is present. The redshift is readily understood by noting that, as the tunnelling current depends nonlinearly on the phase difference ($J \propto \sin\phi$), the inductance follows as $L \propto 1/\cos\phi$, and in turn the Josephson plasma resonance frequency decreases as $\omega_J \propto \sqrt{\cos\phi}$, moving to the red for a strong applied field (Savel'ev *et al.*, 2006).

As the excitation is tuned onto the resonance ($\omega_{FEL} \approx \omega_J$) as reported in figure 7.4 C, the nonlinear response becomes more pronounced and new features emerge. During the first 50 ps, the time-dependent loss function shows a broadening to the red, accompanied by a strong re-shaping. In the un-driven regime for time delays greater than 50 ps, the formation of a long-lived dip is observed, extending over the whole temporal window of our measurement. A similar dip is observed for excitation closely below the resonance ($\omega_{FEL} < \omega_J$), as depicted in figure 7.4 D. The upper panels in figure 7.4 C and D show lineouts of the loss function in the un-driven regime at time delays of 110 ps. The dips in the loss functions represent a significant reduction of the coupling of the electromagnetic probe radiation to the Josephson plasma wave excitations, implicating the development of a narrow transparency window.

The interpretation of this transparency effect is discussed in the following sections. In the proposed scenario, long-lived large amplitude nonlinear plasma waves, excited by the narrowband free electron laser, destructively interfere with the probed Josephson plasma waves. It has to be emphasised that spectral hole burning is a further possible explanation for the transparency dip (Moerner and Bjorklund, 1988). However, the fact that the unperturbed Josephson plasma resonance does not give rise to an inhomogeneously broadened lineshape (one of the key requirements for hole burning), and the observation that the loss function dip persists much longer than the decoherence time of linear plasma waves, make this alternative scenario less likely.

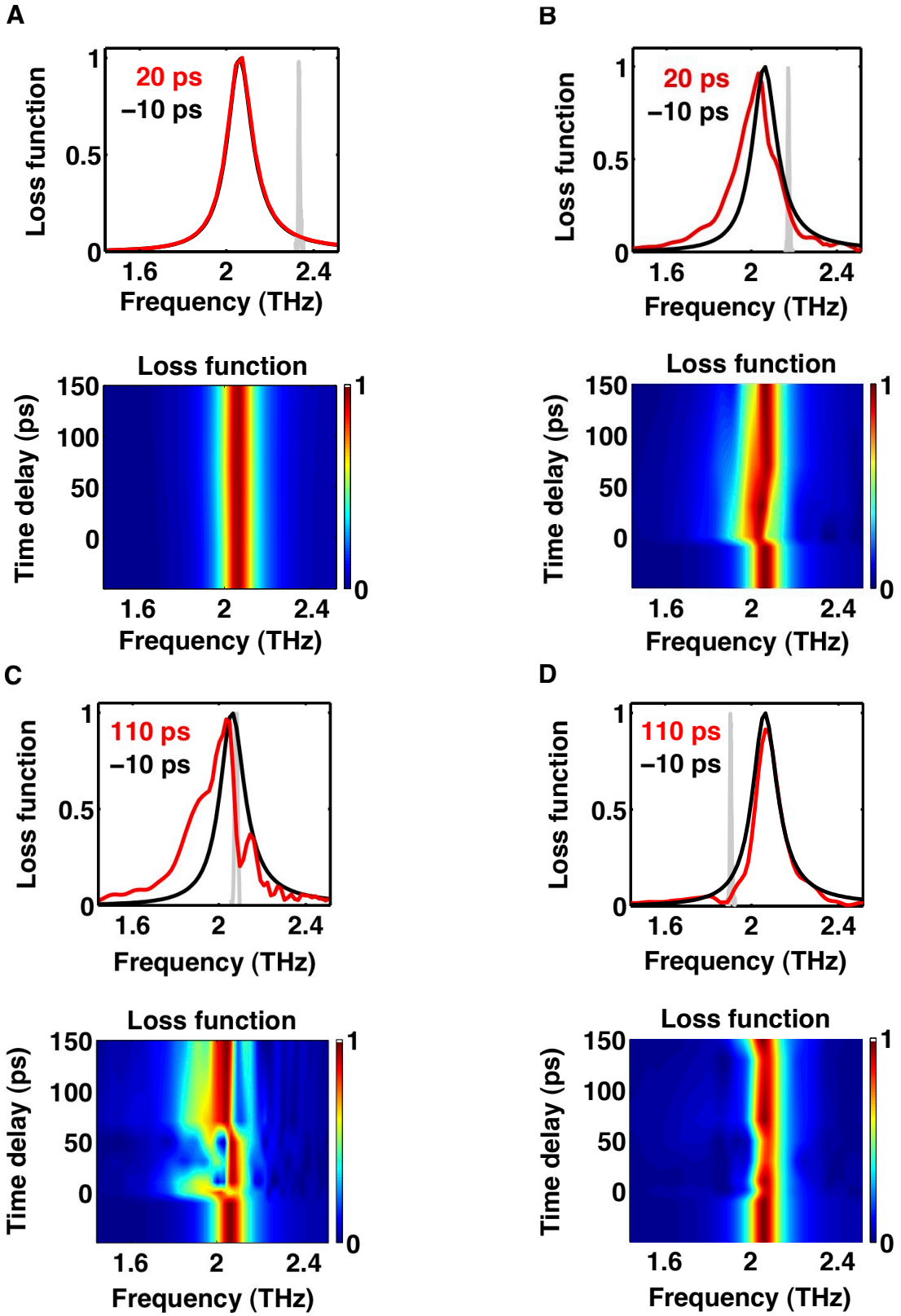


Figure 7.4: Time-dependent loss function. The lower panel of each subfigure reports the frequency-dependent loss function, measured for different time delays between a 2.5 kV/cm multi-cycle pump field and the probe pulse. The upper panel depicts lineouts of the loss function at relevant time delays, overlaid to the spectrum of the free electron laser (grey line). The pump frequency for each panel is: A: $\omega_{FEL} \approx 2.3$ THz. B: $\omega_{FEL} \approx 2.2$ THz. C: $\omega_{FEL} \approx 2.05$ THz. D: $\omega_{FEL} \approx 1.9$ THz.

7.3 Quantum Plasmonics in Cuprates

The low-temperature optical properties of cuprate superconductors are, for terahertz probe radiation polarised perpendicular to the copper oxygen planes, determined by interlayer tunnelling. A layered cuprate can be thought of as a stack of long Josephson junctions, with a tunnelling inductance L connecting capacitively coupled superconducting planes (see chapter 5). In the linear regime, a Josephson plasma resonance $\omega_J = 1/\sqrt{LC}$ occurs at terahertz frequencies, where C is the capacitance of the planes. Thus, a plasmonic response is observed, having a resonance frequency determined by the superconducting interlayer tunnelling strength (Josephson, 1964). An external small-amplitude terahertz field propagates into the superconductor for frequencies larger than the resonance $\omega > \omega_J$, and is damped for $\omega < \omega_J$ (Thorsmølle *et al.*, 2001; Tamasaku *et al.*, 1992). For strong applied electromagnetic fields, pronounced nonlinearities are expected to arise (Josephson, 1964; Savel'ev *et al.*, 2006, 2010).

For large fields with frequency below the plasma resonance ($\omega < \omega_J$), as the driving amplitude is attenuated over the c-axis penetration depth λ_c, the nonlinear electrodynamics can be captured by local models (Josephson, 1964). In brief, as the Josephson supercurrent scales as $J \propto \sin\phi$, where ϕ is the order-parameter-phase difference between the layers, the current grows sub-linearly and the Josephson plasma resonance frequency shifts to the red for high electric fields (Dienst *et al.*, 2011a).

For applied radiation with frequency close to the Josephson resonance, propagating plasma modes arise, and both spatial and temporal phase dependence must be taken into account. This regime is described by the sine-Gordon equation, which in one dimension and in absence of dissipation reads (Hu and Lin, 2010)

$$\lambda_c^2 \frac{\partial^2\phi}{\partial x^2} - \frac{1}{\omega_J^2}\frac{\partial^2\phi}{\partial t^2} - \sin\phi = 0 \quad . \tag{7.1}$$

In the case of small interlayer phase differences ($\sin\phi \approx \phi$), the sine-Gordon equation reduces to a linear wave equation with solutions of the type $\phi = \phi_0 \exp\{i(kx - \omega_J t)\}$.

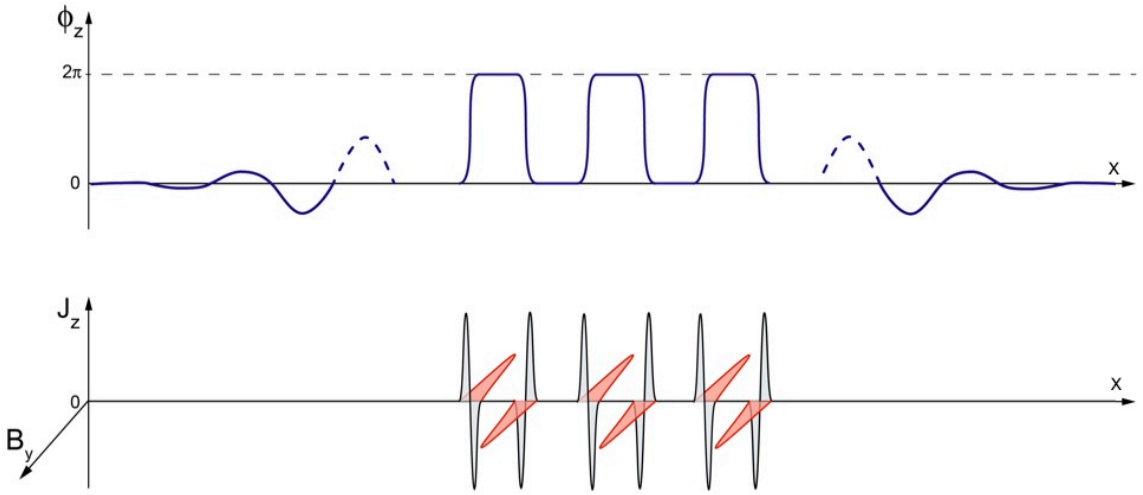


Figure 7.5: Schematic of a Josephson vortex train in a light field. The upper panel depicts the interlayer phase difference ϕ as a function of the spatial coordinate x. As the phase difference is resonantly driven beyond π, the normal mode of the sine-Gordon equation becomes a train of phase kinks, at which the current J changes sign, and the magnetic field B peaks, as shown in the lower panel (Savel'ev *et al.*, 2005; Alfimov and Popkov, 2006).

The plane electromagnetic waves propagate along the layers as Josephson plasmon-polaritons, with dispersion relation $\omega^2 = \omega_J^2 + c'^2 k^2$, where $c' = c/\sqrt{\epsilon_r}$.

The functional forms of the normal modes of the nonlinear sine-Gordon equation have been discussed in chapter 4.2 for long Josephson junctions. Two types of soliton-like solutions exist, typically referred to as kinks and kink-antikink pairs. Single kinks, which have been observed in various experiments (Eilbeck *et al.*, 1981; Kleiner and Müller, 1994), are regions of space in which the interlayer phase difference slips by 2π along the superconducting link over one Josephson length.

In layered cuprates, the normal modes of the sine-Gordon equation are 2π phase kinks of the general form (Savel'ev *et al.*, 2005; Alfimov and Popkov, 2006)

$$\phi = \pi + 2\arctan\left(\frac{2(x-vt)}{l}\right) \quad . \tag{7.2}$$

Here, the lateral vortex size $l = s\lambda_c/\lambda_{ab} = s\gamma$ in an intrinsic junction, defining the core region in which the supercurrent is highly nonlinear, is determined by the superconducting anisotropy γ and the interlayer spacing s. The maximum velocity of a kink is given by $v_c = \omega_J l$, which is much smaller than the Swihart velocity limiting

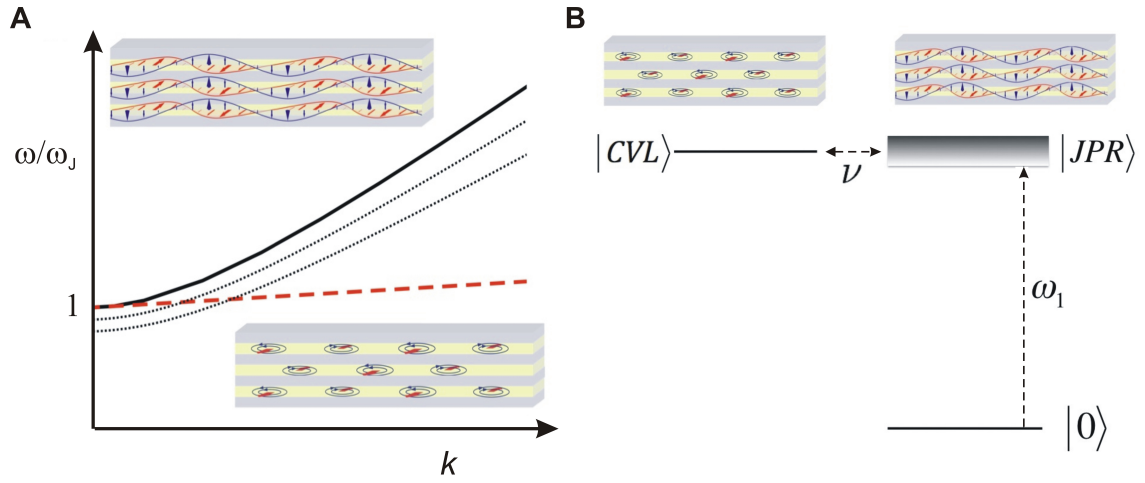


Figure 7.6: Dispersion relations and principle of quantum interference optical transparency. A: Dispersion relations of linear (black line), and weakly nonlinear plasma waves (black dotted line). These are shown in contrast to the dispersion of the Josephson vortex lattice (red line). The nonlinear dispersion becomes one in which the group velocity is significantly reduced in the vortex regime, limiting the region over which phase matched optical coupling to the plasma waves can be achieved (Eilbeck *et al.*, 1981; Savel'ev *et al.*, 2006). B: Schematic of the three-level quantum interference optical transparency process. The broad Josephson plasma resonance (JPR) of frequency ω_1 is probed linearly. The plasma waves interfere destructively with the coherent vortex lattice (CVL), which represents a dark excitation and is spectrally narrow. ν denotes the coupling.

the vortex motion in a single long Josephson junction.

For a strong light field comprising many cycles spaced by one optical wavelength $\lambda \gg l$, as is the case for terahertz radiation, the solution of the nonlinear sine-Gordon equation is that of a train of such kinks. It should be emphasised that each kink is to be thought of as a highly anisotropic Josephson vortex with the magnetic field confined in the dielectric layers, and thus without a normal core (Kleiner *et al.*, 2000).

A one-dimensional picture of the phase ϕ, current J, and magnetic field B is shown in figure 7.5. The vortex structure exhibits a periodicity of one wavelength along the propagation direction x, and of one interlayer spacing perpendicular to the planes. In the following, this excitation is called coherent vortex lattice (CVL).

Figure 7.6 A shows the dispersion relations for the linear Josephson plasma waves (black) and for the coherent vortex lattice (red), the latter having a linear dispersion with slope $v < v_c$. A coherent vortex lattice couples effectively to the plasma excitations if phase- and group-velocity matching are simultaneously achieved, a condition fulfilled only for frequencies $\omega \approx \omega_J$, which is achievable with free electron lasers.

7.4 Transparency Through Quantum Interference

Evidence for the coupling between linear plasma waves and the coherent vortex lattice is found for excitation above the Josephson resonance ($\omega_{FEL} > \omega_J$) only when pump and probe pulses are temporally overlapped at the sample (see figure 7.4 B). Due to enhanced phase matching, coupling to the vortex lattice is stronger if the free electron laser is tuned on, or closely below, the plasma resonance ($\omega_{FEL} \lessapprox \omega_J$). Then, a dip in the loss function and a broadening to the red are observed in the un-driven regime after $\sim$ 50 ps (see figures 7.4 C-D). The dynamic formation of the vortices in the driven regime is a highly nonlinear process requiring significant simulation effort, and will thus not be detailed here (Eilbeck *et al.*, 1981; Lomdahl *et al.*, 1984).

Figures 7.6 B highlights the proposed interpretation of the transparency effect. Linearly excited Josephson plasma waves, which are broad in energy as they represent radiative excitations, are an-harmonically coupled to the Josephson vortex lattice, which is a non-radiative mode with significantly longer lifetime and narrow linewidth. The nature of the coupling is magnetic, as the (along the x-axis) spatially inhomogenous magnetic field $\tilde{B}_y$ of the Josephson plasma waves applies a force $F_x = M_y(\partial \tilde{B}_y/\partial x)$ on the vortices acting parallel to the mutual propagation direction, with M_y being the vortex magnetic moment. Because the magnetic field gradient is directly proportional to the superconducting phase difference across the layers (Savel'ev *et al.*, 2010), this situation is well described by a system of two differential equations (see section 4.1) that have been applied in the past to model electromagnetically- and plasmon-induced transparency in terms of coupled oscillators (Lukin and Imamoğlu, 2001; Liu *et al.*, 2009). In the situation encountered here, the two excitations of the order parameter phase ϕ_1 and ϕ_2 correspond to the Josephson plasma waves and the Josephson vortices, respectively (Joe *et al.*, 2006; Miroshnichenko *et al.*, 2010)

$$\ddot{\phi}_1 + \gamma_1 \dot{\phi}_1 + \omega_1^2 \phi_1 + \nu \phi_2 = A \exp(i\omega t) \quad , \tag{7.3}$$

$$\ddot{\phi}_2 + \gamma_2 \dot{\phi}_2 + \omega_2^2 \phi_2 + \nu \phi_1 = 0 \quad . \tag{7.4}$$

Here, ω_1 and ω_2 are the resonance frequencies of the excitations, γ_1 and γ_2 the damping, and $A\exp(i\omega t)$ is the probe field, which acts only on the Josephson plasma resonance as the Josephson vortex lattice is a dark state. The coupling between the two excitations is described by ν. The amplitude of the harmonic solution $\phi_1 = |\phi_1|\exp(i\omega t)$ for the first oscillator describing linear plasma waves can be expressed as

$$|\phi_1| = \left| \frac{\omega_2^2 - \omega^2 + i\gamma_2\omega}{(\omega_1^2 - \omega^2 + i\gamma_1\omega)(\omega_2^2 - \omega^2 + i\gamma_2\omega) - \nu^2} A \right| \quad . \tag{7.5}$$

Thus, for finite coupling $\nu \neq 0$, the Lorentzian response function of the first oscillator is altered, corresponding to interference between the linear Josephson plasma waves and the vortex train[†]. As the loss function is directly proportional to the amplitude response of the linear Josephson plasma waves (Koshelev, 2007), this model can be scaled to fit the dip in the non-equilibrium loss function.

When the free electron laser is tuned well above the resonance frequency as shown in figure 7.7 A, the coupled oscillator model reproduces the marginal redshift of the loss function in the driven regime. The same accounts for the strong redshift when the excitation is tuned closely above the plasma frequency as depicted in figure 7.7 B.

Figure 7.7 C depicts the situation when the free electron laser is tuned on resonance. Here, the model faithfully reproduces the transparency window at the excitation frequency, but fails to account for the broadening on the red side of the loss function. The low-frequency shoulder can be modelled by allowing ω_1 to become frequency-dependent over a narrow interval below the plasma resonance. This is equivalent to equation (7.5) including, as the driving field is Gaussian, a distribution of plasma frequencies ω_1 (Dordevic *et al.*, 2003), which is allowed to decrease, over a window defined by the 1 % bandwidth of the excitation laser, from $\omega_1 = \omega_J$ at $\omega > \omega_{FEL}$ to $\omega_1 = 0.95\,\omega_J$ for $\omega < \omega_{FEL}$. Microscopically, this approach accounts for

[†]This set of coupled differential equations represents one of the simplest systems that give rise to the Fano resonance (Miroshnichenko *et al.*, 2010; Luk'yanchuk *et al.*, 2010). The fundamental criterion for the occurrence of destructive interference is the overlapping of a broad with a spectrally-narrow resonance, which is given here, since the vortex lattice represents a dark resonance with $\gamma_2 < \gamma_1$, and the excitation frequency is tuned close to the Josephson plasma resonance ($\omega_2 \approx \omega_1$).

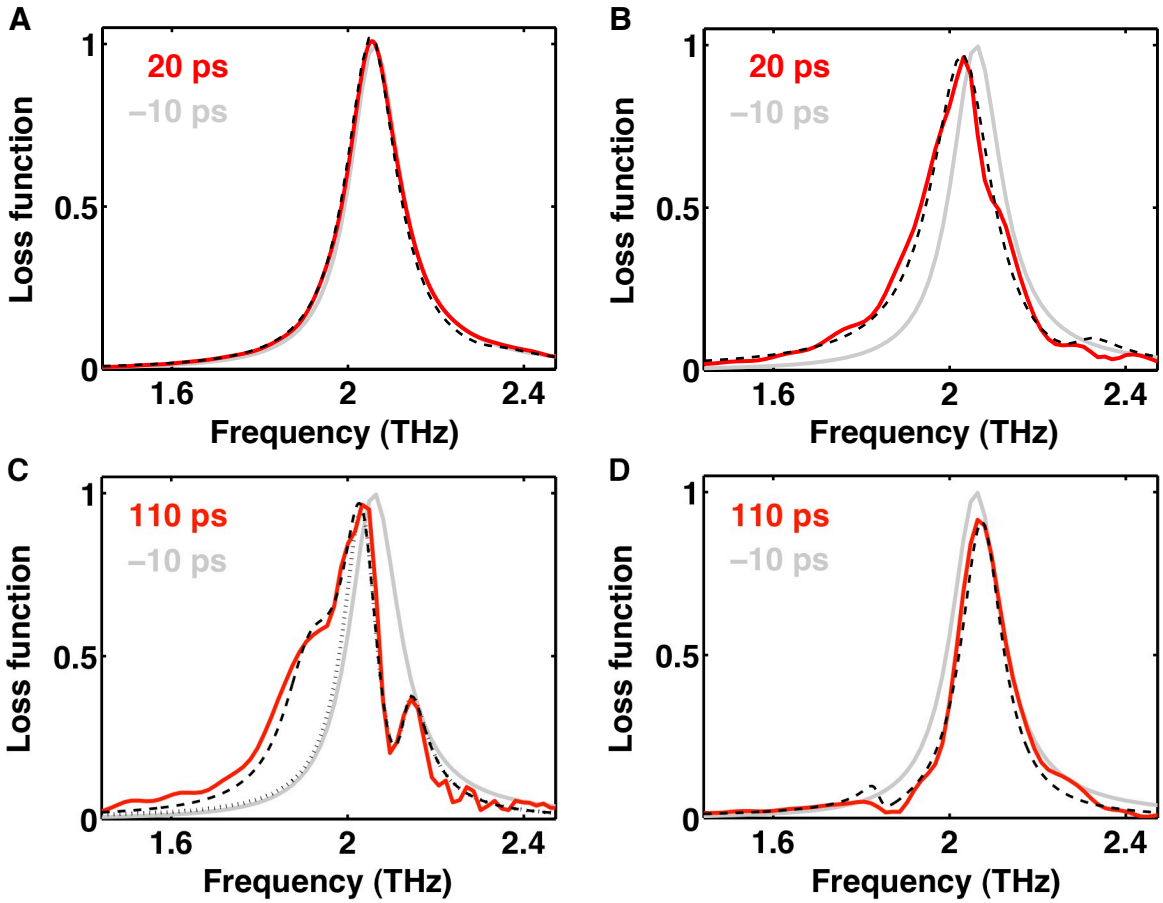


Figure 7.7: Fit of the loss function with the coupled oscillator model. The equilibrium loss function (grey line) is fitted with $|\phi_1|$ from equation (7.5), yielding $\gamma_1 = 0.12$ THz, whereas $\omega_1 = \omega_J$ and $\nu = 0$ are kept constant. A: When the free electron laser is tuned well above the resonance frequency ($\omega_{FEL} \approx 2.3$ THz), the coupled oscillator model reproduces the marginal redshift of the loss function in the driven regime using the fitting parameters $\omega_2 = \omega_{FEL}$, $\gamma_2 = 0.12$ THz, and $\nu = 0.35$ $1/\mu s^2$. B: For excitation closely above the plasma frequency ($\omega_{FEL} \approx 2.2$ THz), the pronounced redshift is well-captured using the parameters $\omega_2 = \omega_{FEL}$, $\gamma_2 = 0.12$ THz, and $\nu = 0.35$ $1/\mu s^2$. C: When the free electron laser is tuned on resonance ($\omega_{FEL} \approx 2.05$ THz), the model reproduces the emergence of the transparency window, but fails to account for the low-frequency shoulder (black dotted line). The asymmetric broadening can be incorporated by allowing ω_1 to become frequency-dependent over a narrow interval below the plasma frequency (black dashed line). The fitting parameters read $\omega_2 \approx \omega_{FEL}$, $\gamma_2 = 0.06$ THz, and $\nu = 0.35$ $1/\mu s^2$. D: For excitation well below the Josephson plasma resonance ($\omega_{FEL} \approx 1.9$ THz), the physics is well-captured by the coupled oscillator model, as the transparency window emerges at the excitation frequency (black dashed line). The out-of-equilibrium fitting parameters are $\omega_2 \approx \omega_{FEL}$, $\gamma_2 = 0.04$ THz, and $\nu = 0.35$ $1/\mu s^2$.

the fact that close to the vortex core, the phase difference is highly nonlinear, effectively reducing the Josephson resonance frequency as $\omega_J \propto \sqrt{\cos\phi}$, and thus allowing for the propagation of weak plasma waves with $\omega < \omega_J$ (Savel'ev *et al.*, 2010).

Figure 7.7 D shows a fit of the loss function for excitation below the Josephson plasma resonance. The simple model captures the main features of destructive inter-

ference between the linear plasma waves and the dark vortex modes in the specimen, resulting in a narrow window of transparency at the excitation frequency.

The dip in the loss function is long lived, and its decay can be extrapolated to a single exponential of 150 ps. As the decay time of vortex excitations due to quasiparticle dissipation accounts for several nanoseconds in layered cuprates (Gulevich and Kusmartsev, 2006), this lifetime is interpreted as a propagation effect, related to the vortex group velocity. As the penetration depth at the plasma frequency is circa ~ 15 μm, vortices propagating at a velocity of $v \approx 10^5$ m/s would leave the probed volume on this timescale. This corresponds to ~ 70 % of the theoretically predicted maximum vortex velocity $v_c \approx 1.4 \cdot 10^5$ m/s in $La_{1.84}Sr_{0.16}CuO_4$ (Savel'ev *et al.*, 2005).

7.5 Concluding Paragraphs

As discussed above, it has to be emphasised that the interpretation of optically induced quantum interference possibly does not represent the only reasonable explanation of the transparency effect observed in the present work. Therefore, it would be highly interesting to validate the nature of the coherent vortex lattice in an independent experiment, for instance using sophisticated imaging techniques (Moler *et al.*, 1998) in combination with the applied free electron laser excitation. Further terahertz pump, terahertz probe spectroscopy experiments, along the lines presented above but taking into account the full temperature- and doping-range of $La_{2-x}Sr_xCuO_4$ available, would also be of considerable interest to gain insight into the intriguing dynamics observed.

Under the assumption of the validity of the present interpretation it shall be noted that, since Josephson vortex lattices do not couple to probe radiation linearly, the experimental geometry presented here is highly attractive, as vortex excitations are key to a number of fundamental properties of superconductors. Indeed, superconducting vortices have been studied statically in a number of geometries, including magnetisation (Xu *et al.*, 2000), calorimetry (Schilling *et al.*, 1996), optical spectroscopy (Dordevic *et al.*, 2005; Thorsmølle *et al.*, 2006), and neutron scattering (Cubitt *et al.*,

1993). However, their out-of-equilibrium dynamic response has largely remained out of reach.

At the current state of technology, these propagating vortices are not easily controlled, as the narrowband sources needed to inject them are limited to terahertz free electron lasers. However, the potential of the present effect for quantum technologies (Longdell *et al.*, 2005; Fleischhauer *et al.*, 2005; O'Brien *et al.*, 2009), extending some features of gas-phase electromagnetically induced transparency to the solid state at relatively high base temperatures, should be noted, especially if one envisages coupling with solid state terahertz laser technology, which is also evolving rapidly (Ferguson and Zhang, 2002; Tonouchi, 2007; Kumar *et al.*, 2011).

More specifically, the experiment demonstrated here might open a number of new possibilities for solid-state nonlinear optics. The nature of the coherent vortex lattice is completely determined by quantum-mechanical phenomena, and the effect could serve for sensing of local magnetic fields or even computation, along the lines of what has been proposed for electromagnetically induced transparency in atomic gases. The development of femtosecond spatio-temporal shaping of narrowband pulses in the terahertz range would allow control of such coherent vortex lattices individually, opening the way to new applications in plasmonics. All solid state technologies, the use of superconducting cuprates may yield to integrated platforms, if combined with solid state terahertz sources (Köhler *et al.*, 2002). Finally, command of such processes may also allow for progress in the ability to manipulate quantum matter, optimising light control of cuprates (Fausti *et al.*, 2011).

Chapter 8

Summary and Outlook

This thesis reports on how recent technological advances in terahertz science can benefit materials research. The utilised methods of high-intensity terahertz generation represent state of the art technology, opening the opportunity to observe phenomena that were inaccessible before. At the beginning, an introduction to terahertz science is given, outlining how light-matter interaction can be exploited to gain physical information using spectroscopy. Terahertz time-domain techniques are discussed as amplitude- and phase-sensitive probes of matter that allow to extract the real and imaginary part of the frequency-dependent optical properties. The combination of this sensitive probe technique with recent advances in high-intensity terahertz generation allows time-resolved studies of systems far from equilibrium. The sources employed for the pump-probe measurements are characterised based on experimental data.

In the following, superconductivity is outlined by introducing different theoretical approaches that capture the fundamental physics observed. Layered cuprates are presented as prototype high critical temperature superconductors. Emphasis is put on the out-of-plane electrodynamics, which can be understood by considering adjacent copper oxygen layers as superconducting planes coupled by the Josephson effect.

Thereafter, Josephson physics are discussed by exhibiting how interlayer coupling leads to intriguing collective phenomena in stacks of junctions. It is shown that charge transport in cuprates can be described by the sine-Gordon equation for the relative

order parameter phase. Nonlinear large-amplitude soliton solutions are introduced, which physically correspond to vortices carrying one quantum of magnetic flux. Small amplitude plane wave solutions are shown to exist, which can be experimentally observed through the Josephson plasma resonance in layered superconductors.

Subsequently, the cuprate $La_{1.84}Sr_{0.16}CuO_4$ is introduced in more detail as a prototypical layered compound. Attention is devoted to the anisotropic charge transport. The linear optical properties of the layered superconductor are determined experimentally using terahertz time-domain spectroscopy, reproducing the well-characterised Josephson plasma resonance for probe light polarised perpendicular to the planes.

In a first time-resolved experiment, it is unveiled that out-of-plane transport in $La_{1.84}Sr_{0.16}CuO_4$ can be gated at terahertz frequencies. The gating effect becomes possible because charge transport along the *c*-axis depends on the interlayer order parameter phase difference, which is sensitive to applied fields. In equilibrium, the phase difference is close to zero, and the quasi-particles are optimally shorted by the superconducting electrons. As a large amplitude electric field is applied perpendicular to the layers, the relative phase is driven out of equilibrium, and through a critical value at which the Josephson interlayer coupling is switched off. At this point the response becomes resistive, and superconductive transport along the *c*-axis is depleted. To achieve this effect, the terahertz probe apparatus is combined with a tilted pulse front excitation setup, allowing to perform time-resolved spectroscopy. In accordance with the integral of the time-dependent pump transient, the layered superconductor shows sub-picosecond oscillations between superconductive and resistive states. Remarkably, the density of Cooper-pairs within the layers stays constant throughout this process. Since in-plane transport remains unperturbed, this situation amounts to an intriguing state in which the superconductivity features a time-dependent dimensionality. The oscillation frequency depends on the applied electric field strength and increases with amplitude in spirit of the a. c. Josephson effect. This latter phenomenon encapsulates a voltage to frequency conversion on ultrafast timescales, which in principle could be

extended to single nanometre-scale junctions and plasmonic devices.

In a second time-resolved experiment, a free electron laser is used to excite nonlinear Josephson plasma waves in $La_{1.84}Sr_{0.16}CuO_4$. Excitation at frequencies well above the plasma edge leads to the propagation of large-amplitude plasmon-polariton modes in the sample. The resulting large phase differences give rise to sub-linear growth in the Josephson tunnelling current, or, to a larger equivalent inductance, and thus a weakening of interlayer coupling. For excitation frequencies on resonance, a metastable state is created that shows transparency over a narrow spectral window. In the proposed interpretation of the observed effect, a long-lived vortex excitation with the periodicity of the driving electromagnetic wave is created in the solid, uncoupled to a weak external electromagnetic field, but coupled anharmonically to linear plasma excitations. In this picture, the reduced coupling of the probe radiation to the Josephson resonance is the result of disruptive quantum interference between the linear plasma waves and the Josephson vortex lattice. The findings are well-described theoretically by a system of differential equations used in the past to discuss plasmon-induced transparency in classical systems. Here, the transparency effect demonstrates the potential of layered superconductors for quantum nonlinear optics and shows how such experiments allow to study coherent vortex excitations on the ultrafast timescale.

In the future, the availability of high-field radiation covering the whole terahertz spectral region at unmatched intensities may be used for interlayer perturbations of similar kind (Fausti *et al.*, 2011; Dienst *et al.*, 2011a) to probe new theories on cuprates, for instance in stripe-ordered materials in which Josephson de-coupling might be relevant (Berg *et al.*, 2007; Wollny and Vojta, 2009). In this respect, it would be very interesting to combine the high-intensity terahertz sources with x-ray diffraction techniques (Ehrke *et al.*, 2011), as this might allow to probe the interrelationship between interlayer coupling and the electronically-ordered state.

Regardless of the experimental approaches chosen, high-temperature cuprate superconductors will probably remain the subject of intense research for a long time.

Bibliography

Alfimov, G. L. and Popkov, A. F. (2006). Nonlocal electrodynamics of fluxons and nonlinear plasma oscillations in a distributed Josephson junction with electrodes of arbitrary thickness. *Phys. Rev. B*, **73**, 214512.

Altshuler, E. and García, R. (2002). Josephson junction in a magnetic field: Insights from coupled pendula. *Am. J. Phys.*, **71**, 405–408.

Anderson, P. W. (1998). c-Axis electrodynamics as evidence for the interlayer theory of high-temperature superconductivity. *Science*, **20**, 1196–1198.

Averitt, R. D., Rodriguez, G., Siders, J. L. W., Trugman, S. A., and Taylor, A. J. (2000). Conductivity artefacts in optical-pump THz-probe measurements of $YBa_2Cu_3O_7$. *J. Opt. Soc. Am. B*, **17**, 327–331.

Averitt, R. D., Rodriguez, G., Lobad, A. I., Siders, J. L. W., Trugman, S. A., and Taylor, A. J. (2001). Nonequilibrium superconductivity and quasiparticle dynamics in $YBa_2Cu_3O_{7-\delta}$. *Phys. Rev. B*, **63**, 140502.

Bardeen, J., Cooper, L. N., and Schrieffer, J. R. (1957). Theory of Superconductivity. *Phys. Rev.*, **108**, 1175–1204.

Basov, D. N. and Timusk, T. (2005). Electrodynamics of high-T_c superconductors. *Rev. Mod. Phys.*, **77**, 721–779.

Basov, D. N., Woods, S. I., Katz, A. S., Singley, E. J., Dynes, R. C., Xu, M., Hinks,

D. G., Homes, C. C., and Strongin, M. (1999). Sum Rules and Interlayer Conductivity of High-T_c Cuprates. *Science*, **1**, 49–52.

Bednorz, J. G. and Müller, K. A. (1986). Possible High-T_c Superconductivity in the Ba-La-Cu-O System. *Zeitschrift für Physik B*, **64**, 189–193.

Berg, E., Fradkin, E., Kim, E.-A., Kivelson, S. A., Oganesyan, V., Tranquada, J. M., and Zhang, S. C. (2007). Dynamical Layer Decoupling in a Stripe-Ordered High-T_c Superconductor. *Phys. Rev. Lett.*, **99**, 127003.

Binning, G., Rohrer, H., Gerber, C., and Weibel, E. (1982). Tunneling through a controllable vacuum gap. *Appl. Phys. Lett.*, **40**, 178–180.

Bor, Z., Rácz, B., Szabó, G., Hilbert, M., and Hazim, H. A. (1993). Femtosecond pulse front tilt caused by angular dispersion. *Optical Engineering*, **32**, 2501–2504.

Born, M. and Wolf, E. (1975). *Principles of optics: electromagnetic theory of propagation, interference and diffraction of light.* Pergamon, Oxford.

Chen, H.-T., Padilla, W. J., Zide, J. M. O., Gossard, A. C., Taylor, A. J., and Averitt, R. D. (2006). Active terahertz metamaterial devices. *Nature*, **444**, 597–600.

Chen, H.-T., Padilla, W. J., Zide, J. M. O., Bank, S. R., Gossard, A. C., Taylor, A. J., and Averitt, R. D. (2007). Ultrafast optical switching of terahertz metamaterials fabricated on ErAs/GaAs nanoisland superlattices. *Optics Letters*, **32**, 1620–1622.

Cubitt, R., Forgan, E. M., Yang, G., Lee, S. L., Paul, D. M., Mook, H. A., Yethiraj, M., Kes, P. H., Li, T. W., Menovsky, A. A., Tarnawski, Z., and Mortensen, K. (1993). Direct observation of magnetic flux lattice melting and decomposition in the high-T_c superconductor $Bi_{2.15}Sr_{1.95}CaCu_2O_{8+x}$. *Nature*, **365**, 407–411.

Dai, P., Chakoumakos, B. C., Sun, G. F., Wong, K. W., Xin, Y., and Lu, D. F. (1995). Synthesis and neutron powder diffraction study of the superconductor $HgBa_2Ca_2Cu_3O_{8+\delta}$ by Tl substitution. *Physica C*, **243**, 201–206.

Dienst, A., Hoffmann, M. C., Fausti, D., Petersen, J. C., Pyon, S., Takayama, T., Takagi, H., and Cavalleri, A. (2011a). Bi-directional ultrafast electric-field gating of interlayer charge transport in a cuprate superconductor. *Nature Photonics*, **5**, 485–488.

Dienst, A., Fausti, D., Hoffmann, M. C., Khanna, V., Gensch, M., Seidel, W., Winnerl, S., Pyon, S., Takayama, T., Takagi, H., and Cavalleri, A. (2011b). Quantum interference optical transparency in a cuprate superconductor. *(submitted).*

Dienst, A., Hoffmann, M. C., Fausti, D., Pyon, S., Takayama, T., Takagi, H., and Cavalleri, A. (2011c). THz Control of Interlayer Coupling in High-T_c Superconductors. In Chergui, M., Jonas, D. M., Riedle, E., Schoenlein, R. W., and Taylor, A. J. (Eds.), *Ultrafast Phenomena XVII.* Oxford University Press, Oxford, 128-130.

Dordevic, S. V., Komiya, S., Ando, Y., and Basov, D. N. (2003). Josephson Plasmon and Inhomogeneous Superconducting State in $La_{2-x}Sr_xCuO_4$. *Phys. Rev. Lett.*, **16**, 167401.

Dordevic, S. V., Komiya, S., Ando, Y., Wang, Y. J., and Basov, D. N. (2005). Josephson vortex state across the phase diagram of $La_{2-x}Sr_xCuO_4$: A magneto-optics study. *Phys. Rev. B*, **71**, 054503.

Dresselhaus, M. (2011). Solid State Physics (Part II): Optical Properties of Solids. June 2011, URL `http://web.mit.edu/course/6/6.732/www/6.732-pt2.pdf`.

Ehrke, H., Tobey, R. I., Wall, S., Först, M., Khanna, V., Garl, T., Stojanovic, N., Prabhakaran, D., Boothroyd, A. T., Gensch, M., Mirone, A., Reutler, P., Revcolevschi, A., Dhesi, S. S., and Cavalleri, A. (2011). Photoinduced Melting of Antiferromagnetic Order in $La_{0.5}Sr_{1.5}MnO_4$ Measured Using Resonant Soft X-Ray Diffraction. *Phys. Rev. Lett.*, **106**, 217401.

Eilbeck, J. C., Lomdahl, P. S., and Newell, A. C. (1981). Chaos in the inhomogeneously driven sine-Gordon equation. *Phys. Lett.*, **87**, 1–4.

Fausti, D., Tobey, R. I., Dean, N., Kaiser, S., Dienst, A., Hoffmann, M. C., Pyon, S., Takayama, T., Takagi, H., and Cavalleri, A. (2011). Light-induced Superconductivity in a Stripe-Ordered Cuprate. *Science*, **331**, 189–191.

Ferguson, B. and Zhang, X.-C. (2002). Materials for terahertz science and technology. *Nature Materials*, **1**, 26–33.

Feynman, R. P., Leighton, R. B., and Sands, M. (1966). *The Feynman lectures on physics*. Addison–Wesley, Reading, Massachusetts.

Fleischhauer, M., Imamoglu, A., and Marangos, J. P. (2005). Electromagnetically induced transparency: Optics in coherent media. *Rev. Mod. Phys.*, **77**, 633–673.

Foerst, M., Hoffmann, M. C., Dienst, A., Kaiser, S., Rini, M., Tobey, R. I., Gensch, M., Manzoni, C., and Cavalleri, A. (2011). THz control in correlated electron solids: sources and applications. In Peiponen, K., Zeitler, A., and Kuwata-Gonokami, M. (Eds.), *Terahertz Spectroscopy: Theory and Applications*. Springer, (*in print*).

Fudamoto, Y., Tajima, S., Gorshunov, B., Dressel, M., Kakeshita, T., Kojima, K. M., and Uchida, S. (2003). In-Plane Optical Spectra of Optimally-Doped LSCO Single Crystals. *J. Low Temp. Phys.*, **131**, 761–765.

Gabay, M. and Triscone, J.-M. (2011). Superconductors: Terahertz superconducting switch. *Nature Photonics*, **5**, 447–449.

Gerrits, A. M., Wittlin, A., Duijn, V. H. M., Menovsky, A. A., Franse, J. J. M., and van Bentum, P. J. M. (1994). Josephson plasma oscillations in $La_{1.85}Sr_{0.15}CuO_4$. *Physica C*, **235**, 1117–1118.

Gorshunov, B. P., Pronin, A. V., Volkov, A. A., Somal, H. S., van der Marel, D., Feenstra, B. J., Jaccard, Y., and Locquet, J.-P. (1998). Dynamical conductivity of an MBE-grown $La_{1.84}Sr_{0.16}CuO_4$ thin film at frequencies from 5 to 36 cm^{-1}. *Physica B*, **244**, 15–21.

Gough, C. E., Colclough, M. S., Forgan, E. M., Jordan, R. G., Keene, M., Muirhead, C. M., Rae, A. I. M., Thomas, N., Abell, J. S., and Sutton, S. (1987). Flux quantization in a high-T_c superconductor. *Nature*, **326**, 855.

Gulevich, D. R. and Kusmartsev, F. V. (2006). Perturbation theory for localized solutions of the sine-gordon equation: Decay of a breather and pinning by a microresistor. *Phys. Rev. B*, **74**, 214303.

Harris, S. E. (1996). Electromagnetically Induced Transparency in an Ideal Plasma. *Phys. Rev. Lett.*, **77**, 5357–5360.

Hebling, J., Almasi, G., Kozma, I., and Kuhl, J. (2002). Velocity matching by pulse front tilting for large area THz-pulse generation. *Optics Letters*, **10**, 1161–1166.

Hebling, J., Yeh, K.-L., Hoffmann, M. C., Bartal, B., and Nelson, K. A. (2008a). Generation of high-power terahertz pulses by tilted-pulse-front excitation and their application possibilities. *J. Opt. Soc. Am. B*, **25**, 6–19.

Hebling, J., Yeh, K.-L., Hoffmann, M. C., and Nelson, K. A. (2008b). High-Power THz Generation, THz Nonlinear Optics, and THz Nonlinear Spectroscopy. *IEEE J. Sel. Top. Quant. Electr.*, **14**, 345–353.

Hoffmann, M. C., Brandt, N. C., Hwang, H. Y., Yeh, K.-L., and Nelson, K. A. (2009). Terahertz Kerr effect. *Appl. Phys. Lett.*, **95**, 231105.

Homes, C. C., Dordevic, S. V., Strongin, M., Bonn, A. D., Liang, R., Hardy, W. N., Komiya, S., Ando, Y., Yu, G., Kaneko, N., Zhao, X., Greven, M., Basov, D. N., and Timusk, T. (2004). A universal scaling relation in high-temperature superconductors. *Nature*, **430**, 539–541.

Hu, X. and Lin, S.-Z. (2010). Phase dynamics in a stack of inductively coupled intrinsic Josephson junctions and terahertz electromagnetic radiation. *Supercond. Sci. Technol.*, **23**, 1–29.

Huang, Z. and Kim, K.-J. (2007). Review of x-ray free-electron laser theory. *Phys. Rev. ST Accel. Beams*, **10**, 034801.

Ino, A., Kim, C., Mizokawa, T., Shen, Z.-X., Fujimori, A., Takaba, M., Tamasaku, K., Eisaki, H., and Uchida, S. (1999). Fermi Surface and Band Dispersion in $La_{2-x}Sr_xCuO_4$. *J. Phys. Soc. Jpn.*, **68**, 1496–1499.

Jackson, J. D. (1999). *Classical Electrodynamics*. John Wiley & Sons, Inc., New York.

Jepsen, P. U. and Fischer, B. M. (2005). Dynamic range in terahertz time-domain transmission and reflection spectroscopy. *Optics Letters*, **30**, 29–31.

Joe, Y. S., Satanin, A. M., and Kim, C. S. (2006). Classical analogy of Fano resonances. *Phys. Scr.*, **74**, 259–266.

Joo, J., Baurassa, J., Blais, A., and Sanders, B. C. (2010). Electromagnetically Induced Transparency with Amplification in Superconducting Circuits. *Phys. Rev. Lett.*, **105**, 073601.

Josephson, B. D. (1962). Possible new effects in superconductive tunnelling. *Physics Letters*, **1**, 251–253.

Josephson, B. D. (1964). Coupled Superconductors. *Rev. Mod. Phys.*, **36**, 216–220.

Josephson, B. D. (1965). Supercurrents through barriers. *Adv. in Phys.*, **14**, 419–451.

Kadowaki, K., Kakeya, I., Gaifullin, M. B., Muchiku, T., Takahashi, S., Koyama, T., and Tachiki, M. (1997). Longitudinal Josephson-plasma excitation in $Bi_2Sr_2CaCu_2O_{8+\delta}$: direct observation of the Nambu-Goldstone mode in a superconductor. *Phys. Rev. B*, **56**, 5617–5621.

Kindt, J. T. and Schuttenmaer, C. (1999). Theory for determination of the low-frequency time-dependent response function in liquids using time-resolved terahertz pulse spectroscopy. *J. Chem. Phys.*, **110**, 8589–8596.

Kittel, C. (2005). *Introduction to Solid State Physics*. Wiley, New York.

Kleiner, R. and Müller, P. (1994). Intrinsic Josephson effects in high-T_c superconductors. *Phys. Rev. B*, **49**, 1327–1341.

Kleiner, R., Gaber, T., and Hechtfischer, G. (2000). Stacked long Josephson junctions in zero magnetic field: A numerical study of coupled one-dimensional sine-Gordon equations. *Phys. Rev. B*, **62**, 4086–4095.

Koshelev, A. E. (2007). Electrodynamics of the Josephson vortex lattice in high-temperature superconductors. *Phys. Rev. B*, **76**, 054525.

Kubo, Y., Tanaka, T., Ueda, S., Ishii, S., Tsuda, S., Takahide, Y., Islam, A. N., Tanaka, I., and Takano, Y. (2009). Observation of Macroscopic Quantum Tunneling in $La_{2-x}Sr_xCuO_4$ Intrinsic Josepshon Junctions. *J. of Phys. : Conf. Ser.*, **150**, 052132.

Kumar, S., Chan, C. W. I., Hu, Q., and Reno, J. L. (2011). A 1.8 THz quantum cascade laser operating significantly above the temperature of $\hbar\omega/k_B$. *Nature Physics*, **1**, 166–171.

Köhler, R., Tredicucci, A., Beltram, F., Beere, H. E., Linfield, E. H., Davies, A. G., Ritchie, D. A., Lotti, R. C., and Rossi, F. (2002). Terahertz semiconductor-heterostructure laser. *Nature*, **417**, 156–159.

Larbalestier, D., Gurevich, A., Feldmann, D. M., and Polyanskii, A. (2001). High-T_c superconducting materials for electric power applications. *Nature*, **414**, 368–377.

Lawrence, W. E. and Doniach, S. (1971). *Theory of layer structure superconductors*. Proc. 12th Int. Conf. Low Temp. Phys., Kyoto.

Lebedev, M. V., Misochko, O. V., Dekorsy, T., and Georgiev, N. (2005). On the Nature of "Coherent Artifact". *J. of Exp. and Theor. Phys.*, **100**, 272–282.

Lee, P. A. (2008). From high temperature superconductivity to quantum spin liquid: progress in strong correlation physics. *Rep. Prog. Phys.*, **71**, 012501.

Lee, P. A., Nagaosa, N., and Wen, X.-G. (2006). Doping a Mott insulator: Physics of high-temperature superconductivity. *Rev. Mod. Phys.*, **78**, 17–85.

Lee, Y.-S. (2009). *Principles of Terahertz Science and Technology.* Springer, New York.

Liu, N., Langguth, L., Weiss, T., Kästel, J., Fleischhauer, M., Pfau, T., and Giessen, H. (2009). Plasmonic analogue of electromagnetically induced transparency at the Drude damping limit. *Nature Materials*, **8**, 758–762.

Löffler, T., Hahn, T., Thomson, M., Jacob, F., and Roskos, H. (2005). Large-area electro-optic ZnTe terahertz emitters. *Optics Express*, **13**, 5353–5362.

Logvenov, G., Gozar, A., and Bozovic, I. (2009). High-Temperature Superconductivity in a Single Copper-Oxygen Plane. *Science*, **326**, 699–702.

Lomdahl, P. S., Olsen, O. H., and Samuelsen, M. R. (1984). Breather-kink-antikink-pair conversion in the driven sine-Gordon system. *Phys. Rev. A*, **29**, 350–354.

London, F. and London, H. (1935). The Electromagnetic Equations of the Supraconductor. *Proc. R. Soc. Lond. A*, **149**, 71–88.

Longdell, J. J., Fraval, E., Sellars, M. J., and Manson, N. B. (2005). Stopped Light with Storage Times Greater than One Second Using Electromagnetically Induced Transparency in a Solid. *Phys. Rev. Lett.*, **95**, 063601.

Lukin, M. D. and Imamoğlu, A. (2001). Controlling photons using electromagnetically induced transparency. *Nature*, **413**, 273–276.

Luk'yanchuk, B., Zheludev, N. I., Maier, S. A., Halas, N. J., Nordlander, P., Giessen, H., and Chong, C. T. (2010). The Fano resonance in plasmonic nanostructures and metamaterials. *Nature Materials*, **9**, 707–715.

Ma, X. F. and Zhang, X. C. (1993). Determination of ratios between nonlinear-optical coefficients by using subpicosecond optical rectification. *J. Opt. Soc. Am. B*, **10**, 1175–1179.

Machida, M., Koyama, T., and Tachiki, M. (1999). Dynamical Breaking of Charge Neutrality in Intrinsic Josephson Junctions: Common Origin for Microwave Resonant Absorptions and Multiple-Branch Structures in the I-V Characteristics. *Phys. Rev. Lett.*, **83**, 4618–4621.

Martinov, N. and Vitanov, N. (1992). On some solutions of the two-dimensional sine-Gordon equation. *J. Phys. A: Math. Gen.*, **25**, 419–426.

McCumber, D. E. (1968). Effect of ac Impedance on dc Voltage-Current Characteristics of Superconductor Weak-Link Junctions. *J. App. Phys.*, **39**, 3113–3118.

Meissner, W. and Ochsenfeld, R. (1933). Ein neuer Effekt bei Eintritt der Supraleitfähigkeit. *Naturwissenschaften*, **21**, 787–788.

Miroshnichenko, A. E., Flach, S., and Kivshar, Y. S. (2010). Fano resonances in nanoscale structures. *Rev. Mod. Phys.*, **82**, 2257–2298.

Moerner, W. E. and Bjorklund, G. C. (1988). *Persistent spectral hole-burning: science and applications*. Springer–Verlag, Berlin; London.

Moler, K. A., Kirtley, J. R., Hinks, D. G., Li, T. W., and Xu, M. (1998). Images of interlayer Josephson vortices in $Tl_2Ba_2CuO_{6+\delta}$. *Science*, **20**, 1193–1196.

Mühlschlegel, B. (1959). Die thermodynamischen Funktionen des Supraleiters. *Zeitschr. f. Physik*, **155**, 313–327.

Nahata, A., Weling, A. S., and Heinz, T. F. (1996). A wideband coherent terahertz spectroscopy system using optical rectification and electro-optic sampling. *Appl. Phys. Lett.*, **69**, 2321–2323.

O'Brien, J. L., Furusawa, A., and Vučković, J. (2009). Photonic quantum technologies. *Nature Photonics*, **3**, 687–695.

Orenstein, J. and Mills, A. J. (2000). Advances in the physics of high-temperature superconductivity. *Science*, **288**, 468–474.

Parc, Y. W., Ko, I. S., Kim, C., and Huang, J. Y. (2008). A study of detection schemes in electro-optic sampling technique. *Nucl. Instr. and Meth. in Phys. Res. A*, **586**, 452–457.

Quinlan, S. M., Hirschfeld, P. J., and Scalapino, D. J. (1996). Infrared conductivity of a $d_{x^2-y^2}$-wave superconductor with impurity and spin-fluctuation scattering. *Phys. Rev. B*, **53**, 8575–8582.

Redfield, D. and Burke, W. J. (1974). Optical absorption edge of $LiNbO_3$. *J. Appl. Phys.*, **45**, 4566–4571.

Roessler, D. M. (1965). Kramers-Kronig analysis of non-normal incidence reflection. *Brit. J. Appl. Phys.*, **16**, 1359–1366.

Saleh, B. E. A. and Teich, M. C. (1991). *Fundamentals of Photonics*. John Wiley & Sons, Inc., New York.

Savel'ev, S., Yampol'skii, V. A., Rakhmanov, A. L., and Nori, F. (2005). Generation of tunable terahertz out-of-plane radiation using Josephson vortices in modulated layered superconductors. *Phys. Rev. B*, **72**, 144515.

Savel'ev, S., Rakhmanov, A. L., Yampol'skii, V. A., and Nori, F. (2006). Analogues of nonlinear optics using terahertz Josephson plasma waves in layered superconductors. *Nature Physics*, **2**, 525–525.

Savel'ev, S., Yampol'skii, V. A., Rakhmanov, A. L., and Nori, F. (2010). Terahertz Josephson plasma waves in layered superconductors: spectrum, generation, nonlinear and quantum phenomena. *Rep. Prog. Phys.*, **73**, 026501.

Schafgans, A. A., LaForge, A. D., Dordevic, S. V., Qazilbash, M. M., Padilla, W. J., Burch, K. S., Li, Z. Q., Komiya, S., Ando, Y., and Basov, D. N. (2010). Towards a Two-Dimensional Superconducting State of $La_{2-x}Sr_xCuO_4$ in a Moderate External Magnetic field. *Phys. Rev. Lett.*, **104**, 157002.

Schilling, A., Fisher, R. A., Phillips, N. E., Welp, U., Dasgupta, D., Kwok, W. K., and Crabtree, G. W. (1996). Calorimetric measurement of the latent heat of vortex-lattice melting in untwinned $YBa_2Cu_3O_{7-\delta}$. *Nature*, **382**, 791–793.

Shibauchi, T., Kitano, H., Uchinokura, K., Maeda, A., Kimura, T., and Kishio, K. (1994). Anisotropic penetration depth in $La_{2-x}Sr_xCuO_4$. *Phys. Rev. Lett.*, **72**, 2263–2266.

Tajima, S., Fudamoto, Y., Kakeshita, T., Gorshunov, B., Železný, V., Kojima, K. M., Dressel, M., and Uchida, S. (2005). In-Plane optical conductivity of $La_{2-x}Sr_xCuO_4$: Reduced superconducting condensate and residual Drude-like response. *Phys. Rev. B*, **71**, 094508.

Takagi, H., Ido, T., Ishibashi, S., Uota, M., Uchida, S., and Tokura, Y. (1989). Superconductor-to-nonsuperconductor transition in $(La_{1-x}Sr_x)_2CuO_4$ as investigated by transport and magnetic measurements. *Phys. Rev. B*, **40**, 2254–2261.

Takahashi, H., Igawa, K., Arii, K., Kamihara, Y., Hirano, M., and Hosono, H. (2008). Superconductivity at 43 K in an iron-based layered compound $LaO_{1-x}F_xFeAs$. *Nature*, **453**, 376–378.

Tamasaku, K., Nakamura, Y., and Uchida, S. (1992). Charge dynamics across the CuO_2 planes in $La_{2-x}Sr_xCuO_4$. *Phys. Rev. Lett.*, **69**, 1455–1458.

Thoman, A., Kern, A., Helm, H., and Walther, M. (2008). Nanostructure gold films as broadband terahertz antireflection coatings. *Phys. Rev. B*, **77**, 195405.

Thorsmølle, V. K., Averitt, R. D., Maley, M. P., Bulaevskii, L. N., Helm, C., and Taylor, A. J. (2001). C-axis Josephson plasma resonance observed in $Tl_2Ba_2CaCu_2O_8$

superconducting thin films by use of terahertz time-domain spectroscopy. *Optics Letters*, **26**, 1292–1294.

Thorsmølle, V. K., Averitt, R. D., Shibauchi, T., Hundley, M. F., and Taylor, A. J. (2006). Dynamic Coupling-Decoupling Crossover in the Current-Driven Vortex State in $Tl_2Ba_2CaCu_2O_8$ Probed by the Josephson Plasma Resonance. *Phys. Rev. Lett.*, **97**, 237001.

Tinkham, M. (1996). *Introduction to Superconductivity*. McGraw-Hill, Singapore.

Tonouchi, M. (2007). Cutting-edge terahertz technology. *Nature*, **1**, 97–105.

Tsvetkov, A. A., van der Marel, D., Moler, K. A., Kirtley, J. R., de Boer, J. L., Meetsma, A., Ren, Z. F., Koleshnikov, N., Dulic, D., Damascelli, A., Grüninger, M., Schützmann, J., van Eb, J. W., Somal, H. S., and Wang, J. H. (1998). Global and local measures of the intrinsic Josephson coupling in $Tl_2Ba_2CuO_6$ as a test of the interlayer tunnelling model. *Nature*, **395**, 360–362.

Ustinov, A. V., Kohlstedt, H., Cirillo, M., Pedersen, N. F., and Hallmanns, G. (1993). Coupled fluxon modes in stacked $Nb/AlO_x/Nb$ long Josephson junctions. *Phys. Rev. B.*, **48**, 614–618.

Weis, S., Rivière, R., Deléglise, S., Gavartin, E., Arcizet, O., Schliesser, A., and Kippenberg, T. J. (2010). Optomechanically Induced Transparency. *Science*, **330**, 1520–1523.

Wollny, A. and Vojta, M. (2009). Interlayer Josephson coupling in stripe-ordered superconducting cuprates. *Phys. Rev. B*, **80**, 132504.

Xu, Z. A., Ong, N. P., Wang, Y., Kakeshita, T., and Uchida, S. (2000). Vortex-like excitations and the onset of superconducting phase fluctuation in underdoped $La_{2-x}Sr_xCuO_4$. *Nature*, **406**, 486–488.

Appendix A

Photos and Cover

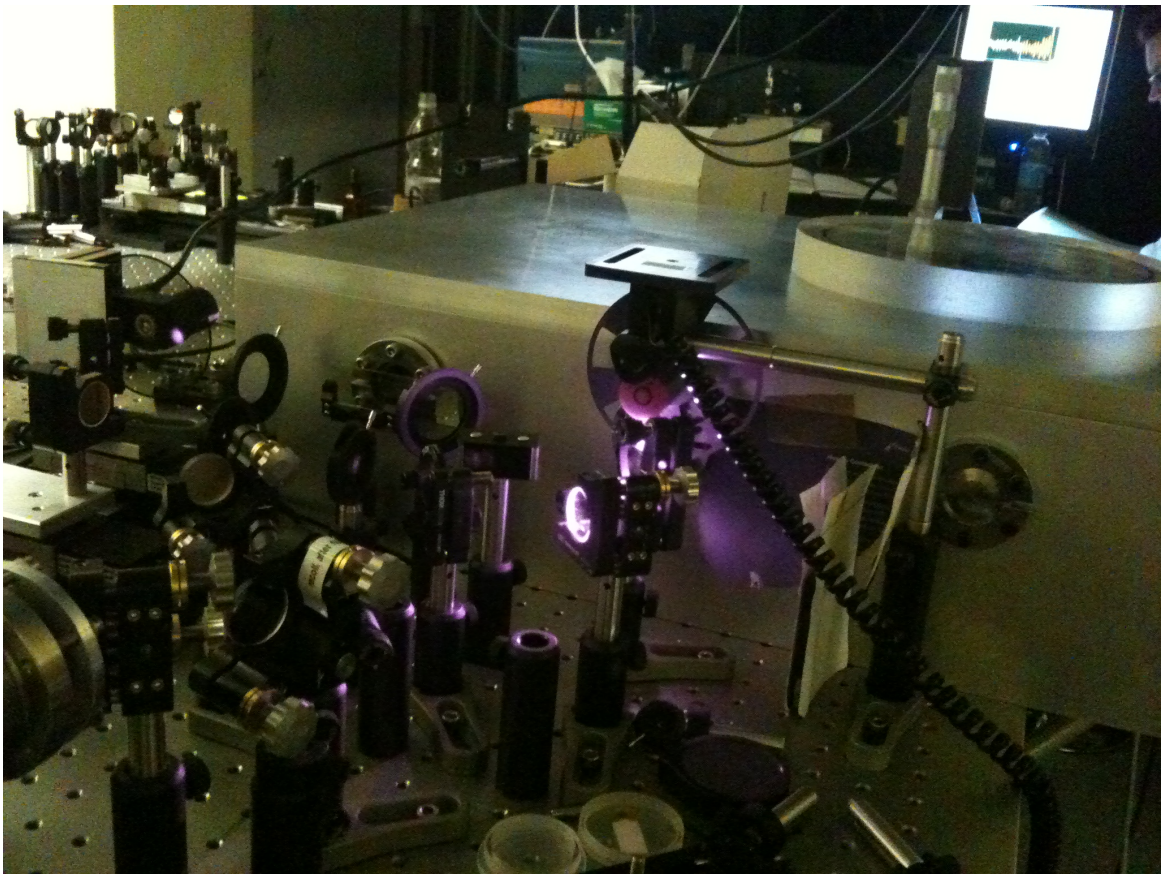


Figure A.1: Photograph of the Oxford vacuum chamber exterior. The vessel is closed and evacuated, while a window on the top allows to adjust the spatial overlap between the laser beams at the sample position. The optics in the foreground split the beam into pump, probe, and EOS component, which can be temporally delayed with respect to each other using optical delay lines. A data acquisition programme allows real-time analysis of the experimental results.



Figure A.2: Photograph of the Oxford vacuum chamber interior. Within the vessel, a terahertz time-domain spectroscopy apparatus is assembled together with a tilted pulse front setup.

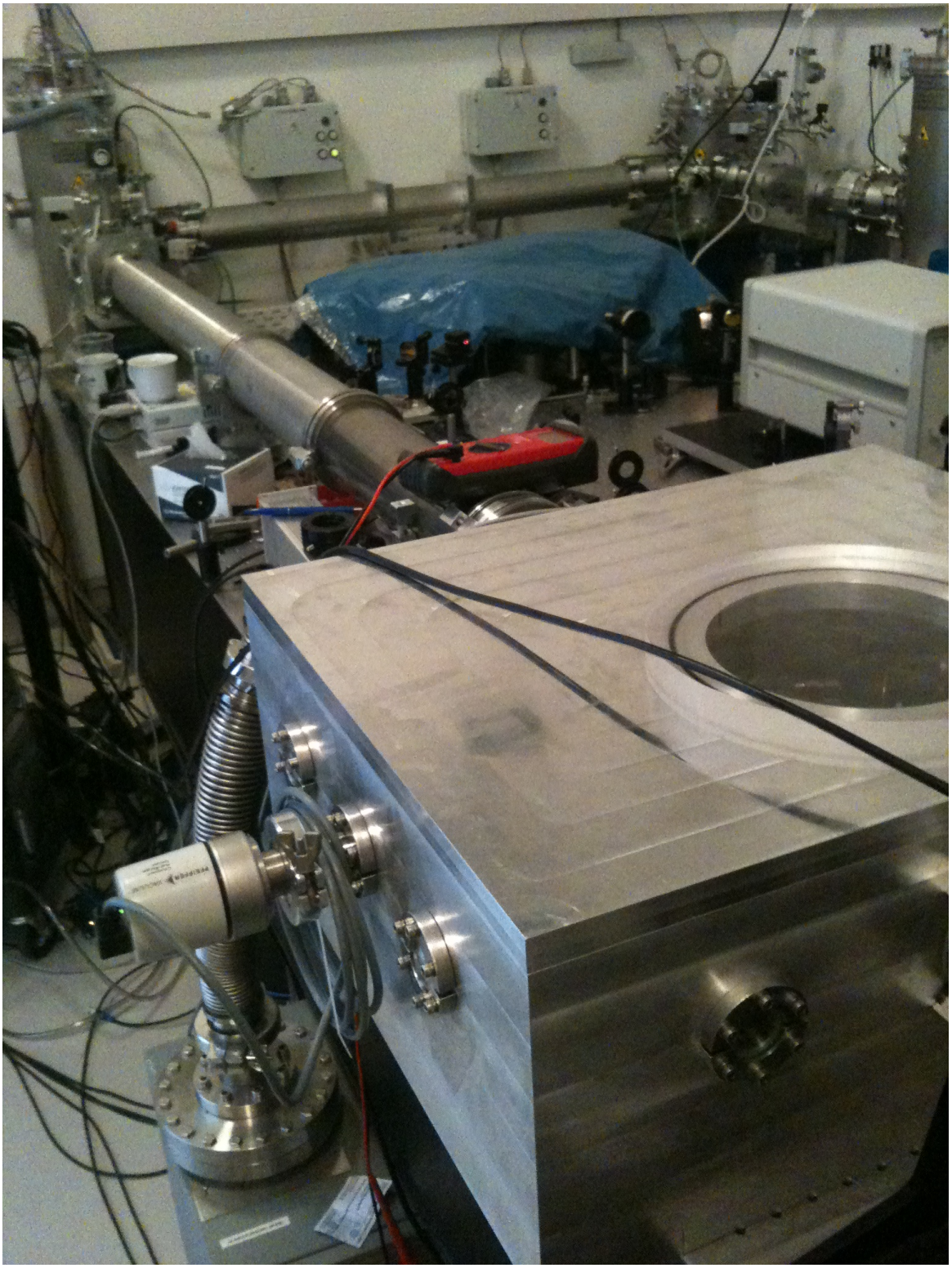


Figure A.3: Photograph of the Dresden vacuum chamber exterior. The vessel is directly connected to the free electron laser output such that all terahertz propagation takes place in vacuum.



Figure A.4: Photograph of the Dresden vacuum chamber interior. In the vessel, the free electron laser polarisation is rotated by 90°, and the beam is subsequently focussed onto the specimen. The time-dependent sample properties are then probed by delayed time-domain spectroscopy pulses.



Figure A.5: Cover of the August 2011 issue of *Nature Photonics*. The magazine also contains a News and Views article featuring the interlayer gating experiment (Gabay and Triscone, 2011). The illustration of charge transport across the superconducting planes is courtesy of J. Harms.